DISSERTATION

IMPROVING THE QUALITY OF EXTREME PRECIPITATION ESTIMATES USING SATELLITE

PASSIVE MICROWAVE RAINFALL RETRIEVALS

Submitted by

Veljko Petković

Department of Atmospheric Science

In partial fulfillment of the requirements

For the Degree of Doctor of Philosophy

Colorado State University

Fort Collins, Colorado

Summer 2017

Doctoral Committee:

      Advisor: Christian D. Kummerow

      Thomas H. Vonder Haar
      Steven A. Rutledge
      Jeffrey D. Niemann

ABSTRACT

IMPROVING THE QUALITY OF EXTREME PRECIPITATION ESTIMATES USING SATELLITE

PASSIVE MICROWAVE RAINFALL RETRIEVALS

Satellite rainfall estimates are invaluable in assessing global precipitation. As a part of

the Global Precipitation Measurement (GPM) mission, a constellation of orbiting sensors,

dominated by passive microwave imagers, provides a full coverage of the planet

approximately every 2-3 hours. Several decades of development have resulted in passive

microwave rainfall retrievals that are indispensable in addressing global precipitation

climatology. However, this prominent achievement is often overshadowed by the retrieval's

performance at finer spatial and temporal scales, where large variability in cloud

morphology poses an obstacle for accurate rainfall measurements. This is especially true

over land, where rainfall estimates are based on an observed mean relationship between

high frequency (e.g., 89 GHz) brightness temperature (Tb) depression (i.e., the ice-scattering

signature) and rainfall rate.

In the first part of this study, an extreme precipitation event that caused historical

flooding over south-east Europe is analyzed using the GPM constellation. Performance of the

rainfall retrieval is evaluated against ground radar and gage reference. It is concluded that

satellite observations fully address the temporal evolution of the event but greatly

underestimate total rainfall accumulation (by factor of 2.5). A primary limitation of the

rainfall algorithm is found to be its inability to recognize variability in precipitating system

structure. This variability is closely related to the structure of the precipitation regime and the large-scale environment.

To address this influence of rainfall physics on the overall retrieval bias, the second part of this study utilizes TRMM radar (PR) and radiometer (TMI) observations to first confirm that the Tb-to-rain-rate relationship is governed by the amount of ice in the atmospheric column. Then, using the Amazon and Central African regions as testbeds, it demonstrates that the amount of ice aloft is strongly linked to a precipitation regime. A correlation found between the large-scale environment and precipitation regimes is then further examined. Variables such as Convective Available Potential Energy (CAPE), Cloud Condensation Nuclei (CCN), wind shear, and vertical humidity profiles are found to be capable of predicting a precipitation regime and explaining up to 40% of climatological biases. Dry over moist air conditions are favorable for developing intense, well organized systems such as MCSs in West Africa and the Sahel. These systems are characterized by strong Tb depressions and above average amounts of ice aloft. As a consequence, microwave retrieval algorithms misinterpret these non-typical systems assigning them unrealistically high rainfall rates. The opposite is true in the Amazon region, where observed raining systems exhibit relatively little ice while producing high rainfall rates.

Based on these findings, in the last part of the study, the GPM operational retrieval (GPROF) for the GMI sensor is modified to offer additional information on atmospheric conditions to its Bayesian-based algorithm. When forming an estimate, the modified algorithm is allowed to use this ancillary information to filter out *a priori* states that do not match the general environmental condition relevant to the observation and thus reduce the difference between the assumed and observed variability in ice-to-rain ratio. The results are

compared to the ground Multi-Radar Multi-Sensor (MRMS) network over the US at various

spatial and temporal scales demonstrating outstanding potentials in improving the accuracy

of rainfall estimates from satellite-borne passive microwave sensors over land.

ACKNOWLEDGMENTS

TABLE OF CONTENTS

LIST OF FIGURES

CHAPTER 1

INTRODUCTION

1.1 Motivation

Recent climate records suggest substantial changes are occurring in extreme rainfall events across the globe [Beniston et al. 2007, Intergovernmental Panel on Climate Change (IPCC) 2007]. These changes have significant socioeconomic impacts by directly affecting management of important water-related resources such as irrigation, flood control, and administering freshwater supplies (Futrel et al. 2005; NRC 2010). Understanding their causes is critical for both science and water management planning strategies. From the scientific perspective, precipitation is seen as one of the key components in Earth's climate. Coupling global water and energy cycles through clouds, moisture, and atmospheric circulations [latent heat release (Trenberth et al. 2007)], precipitation responses to changes in their global trends. Accurate knowledge of precipitation intensity and accumulation, especially during extreme events, is essential for understanding the variability and early detection of these trends. From the water resources perspective, precipitation trends have a major impact on stream flows and water supply systems. Our ability to control these flows and supplies in a constantly changing climate is largely limited by our skill to promptly detect them. This often brings the focus of observations to extreme events where trending state of the system is naturally amplified and easier to discover.

The importance of understanding global precipitation trends and variability of rainfall extremes has not been fully recognized until fairly recently (Allen and Ingram, 2002; Sun et al. 2007). Limited coverage and inferior technology were the greatest challenges for complete and accurate understanding of global precipitation extremes. After the launch of the Global Precipitation Measurement (GPM) mission in February 2014, great strides are being made but there are outstanding science issues that need to be addressed before robust guidance can be provided.

The GPM core satellite carries the first ever dual-frequency radar and is thus able to provide high quality rainfall rate estimates as well as descriptions of the structure of individual extreme events over most of the globe. The dual frequency radar unfortunately covers only a narrow swath (approximately 100 km) and thus has a very long revisit time that makes it difficult to detect extreme rainfall accumulations needed for most applications. In the GPM concept, this problem is addressed via the constellation of passive microwave radiometers that have an average revisit time of less than 3 hours. Key to their success, however, are unbiased rainfall estimates.

Passive microwave (PMW) measurements made from space are affected by both atmospheric and surface properties. A full understanding of the difficulties, currently surrounding rainfall retrievals over land, requires a detailed understanding of existing algorithms, most of which aim to relate Tb (brightness temperature) depressions to surface rainfall through a universal relationship between ice scattering and surface rainfall. A goal of this research is to understand these differences such that the microphysics of clouds is better captured. This will allow for improved fidelity of rainfall extremes without relying on regional sub-setting that ignores the underlying physics.

1.2 Outline of Dissertation

This dissertation consists of five chapters. Following the motivation of the study presented in Chapter 1, Chapters 2 through 4 are to be read as stand-alone papers with their own introductions and conclusions. However, each chapter builds on the preceding one. Chapters 2 and 3 in their present form were published in the *Journal of Hydrology* in December 2015 (Petkovic and Kummerow, 2015) and *Journal of Applied Meteorology and Climatology* in March 2017 (Petkovic and Kummerow, 2017), respectively.

Chapter 2 introduces a version of the operational passive microwave (PMW) rainfall algorithm [Goddard Profiling Algorithm (GPROF 2014)] with a new overland scheme developed specifically to serve as a day-1 rainfall algorithm for the GPM mission. This algorithm was designed to provide consistent precipitation estimates over both ocean and land across diverse satellite platforms and with minor improvement serves as a primary source of rainfall estimates for the entire mission to the present day. With a goal of building a solid foundation for the study as a whole, the performance of this retrieval is tested with a specific focus on extreme rainfall and the role that precipitation regimes may play in overall accuracy of the product. Choosing a well-documented and record breaking event, a constellation of five conically scanning sensors demonstrated an outstanding performance in addressing evolution of long-lasting precipitating scene at high spatial resolution. However, findings indicated that, to a large extent, strong negative biases (-60%) are caused by the differences between the expected and observed ice-scattering signals, suggesting that better understanding of the environment and its impact on rain profiles is the key for successful retrievals in extreme events.

Before any steps towards addressing this issue were taken, the study first tried to examine whether this was a global or perhaps only a localized phenomenon. Using a larger data sample, and an older but better-tested and well-understood retrieval (GPROF 2010 version 2), it was found that variability in ice-scattering signal is responsible not only for significant biases in extreme events but is likely a major source of many of the known systematic errors in PMW retrieval. This was found by analyzing the Tropical Rainfall Measuring Mission (TRMM) satellite rainfall estimates that revealed a substantial disagreement between its active [Precipitation Radar (PR)] and passive [TRMM Microwave Imager (TMI)] sensors over certain regions.

Addressed throughout Chapter 3, this finding emphasized the importance of the cloud morphology on passive microwave signatures. Seen as a primary driver of cloud processes, the focus is then brought to the synoptic state of the atmosphere and its variability over the regions where passive (TMI) and active (PR) microwave retrievals showed greatest discrepancies in surface rainfall estimates. The variability in the relationship between the ice-induced scattering signal and the surface rainfall was easily recognized and further examined using the Amazon River and Central Africa regions as a test bed. It is found that the systematic difference seen between PR and TMI rainfall estimates is well correlated with both the precipitating system structure and the level of its organization. Using radar profiles to group raining scenes into three broad but distinct organizational categories revealed that relative to the PR, deep-organized systems, such as MCSs in West Africa and the Sahel, are typically overestimated by PMW retrieval while the shallower ones, commonly observed over Amazon region, are underestimated. Results suggest that the storm organization level can explain up to 50% of the regional systematic difference between the two sensors.

Because of its potential for retrieval improvement, the ability to forecast the level of systems organization is then tested. The state of the atmosphere is found to favor certain storm types when constrained by CAPE, wind shear, dewpoint depression, and vertical humidity distribution – variables found to be capable of explaining up to 40% of climatological biases. This offered an effective solution for reducing the uncertainties of PMW rainfall estimates presented in Chapter 2. Implementation of this solution into the latest GPM PMW algorithm is presented and assessed in the last part of the study.

In Chapter 4, the latest version of GPM operational retrieval for the GMI sensor is modified to allow both the observed vector and Bayesian *a priori* content to carry information on atmospheric conditions. Qualitative assessment of the information content offered to the retrieval and detailed analysis of the retrieving process were set to provide full understanding on how properties of no radiometric signatures (e.g., CAPE and wind shear) reduced the gap between assumed and observed variability in the relationship between the brightness temperature and observed rainfall.

Chapter 5 summarizes the research objectives, the key findings of the three content chapters, and offers a vision of a future work that builds on the results of this study.

CHAPTER 2

PERFORMANCE OF THE GPM PASSIVE MICROWAVE RETRIEVAL IN THE BALKAN FLOOD

EVENT OF 2014

2.1 Background and Introduction

Observations of precipitation are an important focus of water resource management. According to the fifth assessment report of IPCC working group one (IPCCAR5 WG1), observations and model-projected future changes both indicate increases in extreme precipitation associated with climate change. This is supported by analysis of observed annual maximum 1-day precipitation that indicates a significant increase in extreme precipitation globally, with a median increase of approximately 7% per 1 °C of global mean surface temperature increase (Westra *et al.* 2013). Expectations are that higher moisture content in the atmosphere leads to stronger extreme precipitation as extreme precipitation typically scales with total column moisture. These projections, together with consideration of direct (destruction, floods, etc.) and indirect (contamination, diseases, damaged infrastructure) effects of extreme precipitation, make their detection a priority in hydro-meteorological observations.

Today, WMO[1] as well as national agencies utilize all available resources in an effort to provide the best possible estimates of rain and snow accumulations. Satellite products play

---

[1] See the list of acronyms

an integral role in this scheme, particularly in areas that are not well instrumented. Relying largely on passive microwave measurements, significant challenges exist due to poor temporal sampling and the inability of land retrievals to correctly address these extreme events over the areas where they are of the greatest interest. The launch of the Global Precipitation Measurement (GPM) core satellite (Hou *et al.*, 2014) offers new potential in precipitation observations. Better reference precipitation from GPM's dual frequency radar, together with increased temporal sampling provided by GPM constellation satellites offer great potential for capturing extreme events. New, three-hourly observations are expected to contribute towards improving the existing rainfall accumulations and accompanying flood warnings systems. To meet these expectations, highly accurate rainfall retrievals are needed with sufficient temporal sampling over extended regions. A significant challenge remains to test whether the sometimes limited information content of the passive microwave radiometers can properly retrieve rainfall rates associated with a broad spectra of atmospheric conditions.

To better understand the challenges of retrieving precipitation over land from passive microwave algorithms, aspects of the physical basis and architecture of the retrieval is reviewed. The GPM operational passive microwave rainfall retrieval – GPROF_2014 (Kummerow *et al.* 2015), was released after the launch of GPM core satellite in February 2014. It is a Bayesian retrieval that utilizes ground radar observations to relate observed brightness temperatures (Tbs) to surface rainfall rates. To accomplish this, an *a priori* database was created of coupled NMQ[2] (Zhang *et al.* 2011) precipitation rates and

---

[2] National Mosaic and Multi-Sensor Quantitative Precipitation Estimation

corresponding Tbs (for each instrument in the GPM constellation). The retrieval uses Bayes' theorem to relate the Tb observation vector $\mathbf{y}$ to the rainfall profile $\mathbf{x}$ if an *a priori* distribution of $\mathbf{x}$ is known:

$$\Pr(\mathbf{x} \mid \mathbf{y}) = \Pr(\mathbf{x}) \times \Pr(\mathbf{y} \mid \mathbf{x}) \tag{2.1}$$

where $\Pr(\mathbf{x})$ is the probability of observing a certain rain profile $\mathbf{x}$, and $\Pr(\mathbf{y}|\mathbf{x})$ is the probability of observing the $\mathbf{y}$ vector for a given profile $\mathbf{x}$. This can also be cast in the framework of an "expected value" problem as shown in equation (2.2) were the distances between the observed and database Tb vectors are used to assign weight to individual database entries. This approach allows physical and consistent retrievals across different sensors, providing a statistically "expected" rainfall rate x:

$$E(\mathbf{x}) = \sum_{i} \mathbf{x}_i \frac{\exp\{-0.5[\mathbf{y}-H(\mathbf{x}_i)]^T (\mathbf{O}+\mathbf{S})^{-1} [\mathbf{y}-H(\mathbf{x}_i)]\}}{A} \tag{2.2}$$

where $\mathbf{x}_i$ represents all database profiles, $\mathbf{y}$ is the observation vector, $H(\mathbf{x}_i)$ is the simulated observation vector corresponding to profile $\mathbf{x}_i$ with H being the observation operator, $\mathbf{O}$ and $\mathbf{S}$ are the observation and model error covariance matrices, respectively, while A is a scalar constant serving as the normalization factor (Kummerow *et al.* 2001). While this is usually advantageous for the purpose of generating robust rainfall estimates, it may not be optimal for extreme rain events that are not well represented in the *a priori* ($\Pr(\mathbf{x})$) database. The problem of correctly retrieving "extremes" from a Bayesian methodology therefore depends upon the extent that the scheme can identify the correct extreme cases in the database and the extent to which the scheme does not overly average

database entries towards the mean of the distribution. Both of these factors depend upon the information content of the Tb signal itself.

While the radiative properties of water are well understood, the signal is dramatically different over land and ocean. Over the oceans, a low emissivity surface provides significant contrast between the radiatively cold background and warm precipitation signatures. Unfortunately, this is not the case over the land where high emissivity of the surface and its large variability mask atmospheric emission signatures and make precipitation nearly indistinguishable from the background. To overcome this problem, passive microwave retrievals over land focus on ice scattering signals, which are less well related to precipitation but more easily detected over a warm surface background. This limited information content weakens the linkage between satellite measurements and the *a priori* database and exposes the algorithm to excessive averaging. The key for successful rainfall rate estimate over land is therefore a good understanding of the relationship between the amount of ice in the cloud and surface rainfall rate. Currently, the *a priori* database is constructed using one year of ground radar observations from US NEXRAD radar network matched to Tbs from satellite overpasses. The database is stratified by total precipitable water (TPW) and land surface temperature obtained from global reanalysis data. This provides a broad set of profiles for retrieving a wide range of rainfall rates, including those above 50 mm h^{-1}, but it implicitly imposes a mean relationship between ice aloft and surface precipitation which is representative of the continental United States. Strong evidence exists, however, that the ratio of ice to rain is regionally dependent and sensitive to environmental forcing, such as atmospheric stability, which is often far from average in extreme precipitation events.

The primary goal of this study is to explore GPM's current passive microwave retrieval (GPROF_2014.V1-4) performance in an extreme precipitation event and provide deeper understanding of its potential in the case of extreme events. As a second goal the study seeks to quantitatively evaluate the differences between satellite retrieval and ground measurements in extreme precipitation conditions to gain a better understanding of their relationship.

A case of the Balkan floods of 2014 (described in following section) is seen as a perfect example of an event with microphysics that does not correspond to typical conditions although its rain rates are well within the database range. This makes it ideal for performing a comparison between retrieved satellite accumulations and ground references to provide information on GPROF skills under non-typical atmospheric condition. Available gauge and ground radar network over this region (OPERA, see section 2.3) allow for understanding of how each dataset interprets the flood event.

Important environmental and synoptic scale characteristics of the rain systems are presented in the following section. A more detailed description of datasets used in this study is given in Section 2.3, while results, discussion, and conclusions are provided in Sections 2.4 and 2.5.

2.2. Events description

This study chose two 3-day rainfall events over the Balkan region. An extreme and a more typical Balkan rain events were selected.

2.2.1 *Flood event (14th – 16th May 2014)*

The extreme precipitation event (hereafter – "Balkan flood" or "flood event") focuses on a 3-day period that started at 0000 UTC 14 May 2014, spread over a significant area (see Fig. 2.1) in the central Balkan and affected the countries of Serbia, Bosnia and Herzegovina (BiH), and Croatia. During this event, historical readings at both rain and river gauges were recorded throughout the region that was devastated by floods and mudslides. A number of fatalities and greater than 2 billion dollars in damage[3] were directly caused by this flood event. The area itself contains two catchments: 1) the Adriatic – the most southern 15% of the box shown in Fig. 2.1 that did not flood, and 2) the Black Sea – upper 85% of the box with 2 major rivers (Danube and Sava) and a dozen regional-size basins where the majority of flooding occurred. The study area (15°-21°E, 42-47°N) is defined by the flood region and its Black Sea upstream catchment. It ranges in elevation from 100 m in the predominantly flat plains to the north, to 1700 m in steep elevated terrain to the south of 45° N latitude.

---

[3] No official estimate available at the time of writing this paper
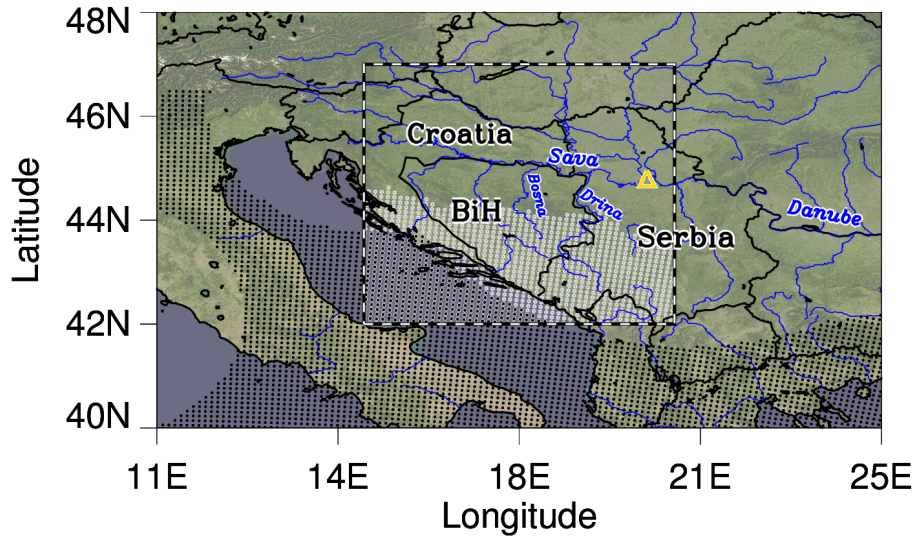
Figure 2.1 Balkan peninsula. Boxed area marks the flood region limits. Shadings denote OPERA network coverage: *shaded in black* **- areas beyond radar range,** *shaded in white* **- no radar coverage due to beam blockage of high terrain. River names are given in blue. Yellow marker indicates sounding location.**

2.2.1.1 The synoptic environment and climatology

Two weeks prior the Balkan flood event, the region experienced localized thunderstorms (May 1st - 3rd) and the passage of a cyclone from the west Mediterranean (May 5th) that brought light to moderate rain to the region. A warm air mass and higher temperatures followed on May 7th – 12th, which contributed to an increase in melting of the remaining snow accumulation in the mountains. This consequently resulted in increased river flows and moderately saturated soil. The period from May 12th to 14th was characterized by clear and warm weather during which a large area, including most of central and southeast Europe, experienced a drop in the geo-potential height. The trough formation at the surface was followed by a surface cutoff Low on May 15th over the central Balkan, which was accompanied by extremely strong and wide 500 mb level depression whose center was positioned over the central and western Balkan. The slow moving Low had its center close to the flood region causing intense precipitation and a decrease in temperature in the period

from May 14th to May 18th. A strong positive west-east gradient of specific humidity at 850 mb was present throughout the event, while the 500 mb values remained uniform and relatively low. The majority of precipitation occurred between May 14th and May 17th with rain at lower elevation and snow generally above 1200 m. While a mean monthly temperature over the area was only 1 °C below the climatological mean, the event mean temperature was 7-8 °C lower.

2.2.1.2 Snow, Rain and River gauge readings

The majority of rain and river gauges in the area of interest recorded historical levels. Climatological monthly means were exceeded by 130-400% at all rain gauges in central and western Serbia and central and north BiH while 3-day accumulations exceeded the long-term mean May monthly values. Five climatological rain gauges in Serbia reported historical levels for 24-hour accumulations. The greatest 3-day accumulation at any station was 209 mm while most of the area received approximately 1/4th of its average annual precipitation in only 72 hours. According to Gumbel's method (Gumbel 1958, Wolf 1966) of extreme value distribution, the 3-day rainfall accumulation had return period ranging between 100 - 1000 years throughout most of the flood region. Major rivers (i.e. Sava, Drina, Bosna) reached 200-300% of their monthly climatological marks. On May 15th the maximum temperature at elevations above 1500 m remained below 0° C, with some stations exceeding 60 cm of new snow accumulations (e.g. Kopaonik mountain: 61cm) during the 24-hour time interval.

2.2.2 Non-Flood event (1st – 3rd May 2014)

A 3-day period (hereafter: non-flood event), starting at 0000 UTC 1 May 2014, is used to study more average conditions over the same 5° x 6° area defined in the case of the flood event. The event was chosen to be: 1) a 72-hour period of frequent precipitation, 2) within

13

proximity (a couple weeks) to the flood event, and 3) characterized by typical precipitation regimes for the season. This provides a strong contrast in rain intensity, environment, and system structures (microphysics and thermodynamics) between the two events.

2.2.2.1 The synoptic environment and climatology

On May 1st, at 500 mb, the formation of a trough over the central Europe occurred as a consequence of an easterly propagating wave that simultaneously formed a strong ridge aligned with the east Atlantic coast. As the trough deepened, a cutoff Low occurred over the Apennine peninsula on May 2nd. This was followed by the formation of a surface low and cyclonic circulation over most of the Balkan region on May 3rd. Under the influence of a cold air mass advected from the north-northwest and moisture coming from the southwest the region experienced scattered precipitation within the first 48 hours followed by rain produced by a more organized mid-latitude system on May 3rd. In contrast to the flood event, no particularly strong gradients in specific humidity were observed. Daily rain accumulations and temperature values were close to their climatological values, with neither moisture nor the persistence of the low being atypical for this time of the year.

2.3. Data.

The study utilizes remote and in situ rainfall measurements from gauge and radar networks as well as the GPM constellation of satellite radiometers. Each dataset is available in near real time and, with the exception of OPERA products, is used in wide spectrum of applications.

*2.3.1 **O**perational **P**rogram for the **E**xchange of **RA**DAR information – OPERA*

Within EUMETNET, the operational program for weather radar networking (OPERA), and its radar data center have been in operation producing network-wide radar mosaics from volumetric data since 2011 (Huuskonen *et al.* 2013). The radar network spreads over most of Europe and exploits more than 130 weather radars of different types and frequencies distributed in 21 European countries.

This study utilizes OPERA's near surface rainfall rate and maximum reflectivity products, both provided on 2 km x 2 km grid at 15 min temporal resolution. Within the flood region these composite fields are formed by combining measurements from five Doppler radars (see Table 2.1) in and close to the region, working at C- and S-band single polarized frequencies. Their coverage is somewhat limited due to beam blockage along the mountain range in the southern flood region but still accounts for approximately 90% of the flood catchment area (the Black Sea catchment). In Fig. 2.1 black shading depicts radars range while regions suffering from terrain beam blockage are shown in gray.

Table 2.1. List of radars used to create OPERA's composites, their IDs, coordinates and band of operation.

Radar name	Country	Radar ID	WMO ID	Lat/Lon [°N]/[°E]	Band	Range [km]
Lisca	Slovenia	LJ41	14024	46.06/15.28	C	250
Maly Javornik	Slovak Rep.	SQ41	12921	48.25/ 17.15	C	240
Bilogora	Croatia	RH42	14256	45.88/ 17.20	S	240
Osijek	Croatia	RH43	14280	45.50/ 18.56	S	240
Timisoara	Romania	RDTM	13169	45.77/ 21.25	S	230

Currently, the OPERA network rain rates are based on the traditional Marshall-Palmer *Z-R* relationship only (Marshall and Palmer (1948): $Z = 200 \, R^{1.6}$). Despite the potential lack of fidelity in representing local gauge accumulation, this provides consistency across different regionally operated systems and allows for better understanding of comparison results

when the product is compared against other independent datasets. It is worth mentioning that a number of storm-specific factors may contribute to overall uncertainty of the OPERA dataset. Some of them include Z-R variability within the storm, the radar signal attenuation, and the highly variable precipitation field (Moszkowicz et al. 1994; Krajewski et al. 2003; Miriovsky et al. 2004; Lee and Zawadzki 2005; Berne and Andrieu 2005). Although addressing this problem is among top priorities of the OPERA project (Sandford and Gaussiat 2011), due to the amount of processed data and radar type variability across the network, in its current stage OPERA project does not quantify contributions from these error sources. However, it is expected that overall uncertainty is largely dominated by the assumption of a constant Marshall-Palmer DSD. To ensure the best possible quality, OPERA data in this study are filtered using accompanying quality control flags, which resulted in data sample reduction of approximately 10% but increased the confidence of ground clutter removal. Missing pixels in the radar data set are replaced by interpolating between the closest available (in time) measurements at the given grid point. This resulted in negligible changes in the results (less than 0.1% of rain accumulation over the domain). During manual inspection of the data set, Local Area Network (LAN) interference, known to be often present in OPERA products (Lopez 2014), is noticed for one radar (Maly Javornik) in the Slovak Republic. These spurious retrievals are replaced by interpolating values of interference-free time-adjacent pixels. In most cases the adjacent pixels had value of zero which overall resulted in negligible changes to the 3-day rainfall accumulations.

2.3.2 Satellite data - GPROF 2014

Five conically scanning sensors in the GPM constellation [AMSR2 (Shimoda 2005), GMI (Hou *et al.* 2014), and SSMIS on board of F16, F17 and F18 satellites operated by the United States Air Force Defense Meteorological Satellite Program (Kunkee *et al.* 2008)] are utilized to provide satellite data. Rainfall rates from 29 overpasses during the flood event and 28 overpasses during the average, non-flood, event over the region of interest are obtained from GPROF_2014 passive microwave retrieval at spatial resolution corresponding to 37 GHz of each sensors FOV with an average temporal sampling of the event of approximately 2.1 hours. Based on the observations of the flood event and simulated channel and forward model errors, retrieval error is estimated to be less than 3% for applications in this study.

2.3.3 Surface gauge data

Surface 24-hour rain accumulations from 25 rain gauges located within the flood region are used as a ground reference in this study. Table 2.2 lists gauge accumulations as given in SYNOP reports while their locations are shown in Fig. 2.2 (blue triangles).
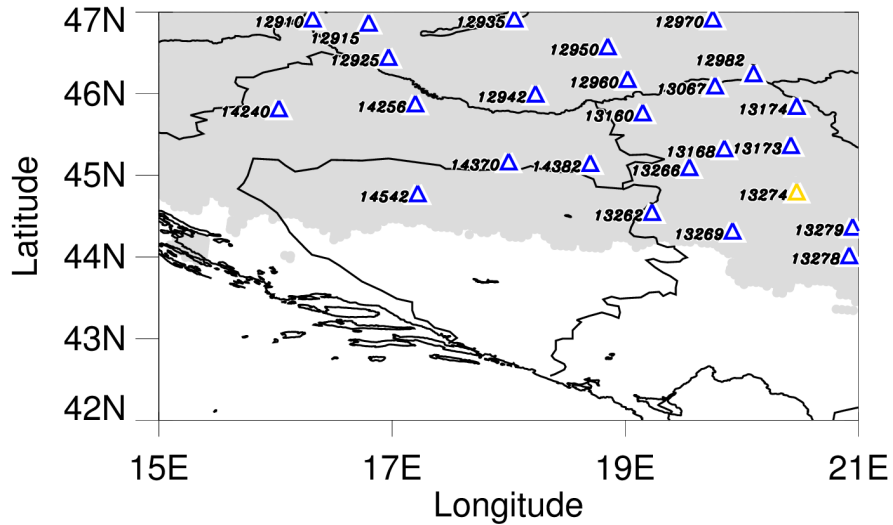
Figure 2.2 Flood region with radar coverage (in gray) and distribution of ground rain gauges (blue triangles labeled by station's WMO IDs) used in the analysis. Yellow marker indicates sounding location.

Although rain gauge observation is generally seen as the most accurate precipitation measurement, the complexity and amplitude of its error requires rigorous quality control before data can be used for scientific purposes. SYNOP rain gauge data can be affected by both systematic and random errors (Lopez 2013). Systematic errors are usually linked to raindrops splashing, high wind conditions, the wetting of the gauge walls, and the loss through evaporation. Random errors are mainly caused by the discrete nature of the time sampling and by small-scale variations of the turbulent airflow around the gauge. In this study all chosen gauges are maintained by National Hydro-meteorological Services undergoing the standard quality control procedures recommended in terms of the latest global standard by WMO. The selected subset of the gauge network is chosen to ensure the best quality confidence and spatio-temporal coverage over the region. During the extreme event meteorological conditions were such that significant errors are not expected (e.g. no high winds are detected throughout the region while precipitation was continuous). On the other hand, the isolated convection seen during the non-flood event may have easily resulted

18

in significant random errors in SYNOP reports. These errors are, however, expected to be relatively small in the 24-hour accumulation due to the averaging over 4 to 8 individual measurements (Ciach 2003). No significant differences in surrounding rain gauges (not included in this study) are reported for the flood-event (no such a report is expected for the non-flood event due to its mediocrity). Three to six hourly gauge readings are verified using monthly reports of national weather centers in the region and by comparing the reports from surrounding rain gauges (non-SYNOP ones). Missing data are found at one gauge location (Banja Luka, WMOid: 14542) for the first day of the flood event and therefore this gauge is used in daily accumulation analysis only.

Table 2.2. List of ground gauge station with 24-hour and 3-day accumulations for flood and an average event used to compare against OPERA's composites and satellite data.

Rain gauge			Accumulation [mm]							
			Flood event				*Average event*			
			May			Total	May			Total
Station name	WMO#	lat/lon [°]	14th	15th	16th		1st	2nd	3rd	
Hungary										
Szentgotthard	12910	46.92/16.32	0.0	1.3	16.0	17.3	0.0	0.0	1.3	1.3
Zalaegerszeg	12915	46.87/16.80	0.0	3.6	12.4	16.0	0.0	1.2	2.7	3.9
Nagykanizsa	12925	46.45/16.97	0.0	1.2	17.8	19.0	0.0	0.7	6.8	7.5
Siofok	12935	46.92/18.05	0.0	0.0	8.7	8.7	0.0	4.1	5.7	9.8
Pecs/Pogany	12942	46.00/18.23	12.0	35.0	31.0	78.0	2.2	2.9	28.9	34.0
Paks	12950	46.58/18.85	7.0	9.8	4.2	21.0	0.0	2.9	16.1	19.0
Baja	12960	46.18/19.02	18.0	20.0	4.0	42.0	0.2	1.7	31.5	33.3
Kecskemet	12970	46.92/19.75	7.0	38.0	1.0	46.0	0.0	1.9	13.2	15.1
Szeged	12982	46.25/20.10	23.0	35.7	7.3	66.0	0.0	2.3	33.7	36.0
Serbia										
Palic	13067	46.10/19.77	20.0	26.4	4.6	51.0	0.0	1.4	32.3	33.7
Sombor	13160	45.77/19.15	21.0	17.0	7.0	45.0	1.8	2.0	37.5	41.3
Novi S. Rim.	13168	45.33/19.85	77.0	39.0	28.6	144.6	0.0	2.7	30.9	33.6
Zrenjanin	13173	45.37/20.42	55.0	29.0	15.0	99.0	5.7	2.9	21.7	30.3
Kikinda	13174	45.85/20.47	27.0	34.0	12.5	73.5	0.0	4.5	26.0	30.5
Loznica	13262	44.55/19.23	129.0	71.0	9.0	209.0	3.1	2.3	28.9	34.3
Sr. Mitrovica	13266	45.10/19.55	56.0	44.0	21.0	121.0	2.8	2.2	33.6	38.6
Valjevo	13269	44.32/19.92	105.4	69.0	6.2	180.6	7.8	3.4	243	35.5
Beograd	13274	44.80/20.47	112.6	58.0	17.0	187.6	1.5	0.0	23.3	24.8
Kragujevac	13278	44.02/20.92	37.0	43.0	1.8	81.8	7.2	0.0	27.0	34.2
Sm. Palanka	13279	44.37/20.95	81.0	49.0	7.3	137.3	7.1	0.0	24.1	31.2
Croatia										
Zagreb Maks.	14240	45.82/16.03	0.0	16.0	13.0	29.0	1.1	4.0	11.7	16.8
Bilogora	14256	45.88/17.20	0.1	10.0	26.0	36.1	0.7	1.8	18.1	20.6
Slavonski B.	14370	45.17/18.00	12.5	36.0	8.0	56.5	2.3	1.8	28.2	32.3
Gradiste	14382	45.15/18.70	43.0	45.0	9.0	97.0	2.1	1.8	37.4	41.3
BiH										
Banja Luka	14542	44.78/17.22	-	23	53	-	2.5	4.3	25.2	-

The European Climate Assessment and Data (ECA&D) E-OBS daily rainfall dataset (Haylock *et al.* 2008, Lockhoff *et al.* 2014) is used for additional OPERA quality control. This high-resolution gridded precipitation product is based on combined monthly and daily gauge estimates using various interpolation and kriging techniques. Although only negligible differences are seen between this product and 24-hour gauge accumulation values from the 25 SYNOP gauges used for this study, potential errors that may emerge from interpolation

techniques (Haylock *et al.* 2008 and Kirstetter *et al.* 2010) do not qualify this dataset for direct comparison with satellite and radar products. Techniques to overcome these problems exist (Lockhoff *et al.* 2014) but unfortunately do not apply to the Balkan region and quality of available data. Therefore, E-OBS dataset is used here only in the process of removing OPERA radar ground clutter and LAN interference (Section 2.3.1).

2.4. Data set inspection

To allow inspection of each dataset and perform their inter-comparisons, both satellite and radar data are first uniformly gridded into 0.2 km grids over the study area at the times of observations. Rainfall is then accumulated at each grid point assuming that rain rates are constant between available measurements. In order to match OPERA's temporal sampling, the time of the satellite overpass is rounded to the closest 15min. This resulted in a virtual overlap of two satellite overpasses (GMI and F16 on May 16th 4:00 UTC) that in reality were 6 minutes apart. Comparison between satellite and radar accumulations are made only where satellite measurements exist.

2.4.1 Ground radar to gauge comparisons

Gauge network observations of both the extreme and average 3-day raining events (described in Section 2.2) are used to evaluate remotely sensed products. Despite the availability of close-to-instantaneous measurements at a number of the gauge locations, (e.g. tipping bucket measurements), their direct comparison to satellite estimates would be sparse and highly sensitive to spatial variability of the rainfall field and random errors. Therefore, rather than comparing satellite FOV to the gauge point measurements directly, a two-step approach is used. In the first step, ground radars are compared against collocated

gauge measurements. In the second step (described in Section 2.4.2) satellite estimates are compared to ground radars.

Figure 2.3 shows 72-hour accumulation maps for the extreme (May 14th – 16th) and non-extreme/average (May 1st - 3rd) 3-day events (panels *a* and *b,* respectively). The color scale depicts radar estimates across the region, while gauge readings are labeled next to the station locations (details given in Table 2.2). Scatter plots of daily accumulations over the area for the same two events are given in Fig. 2.4.
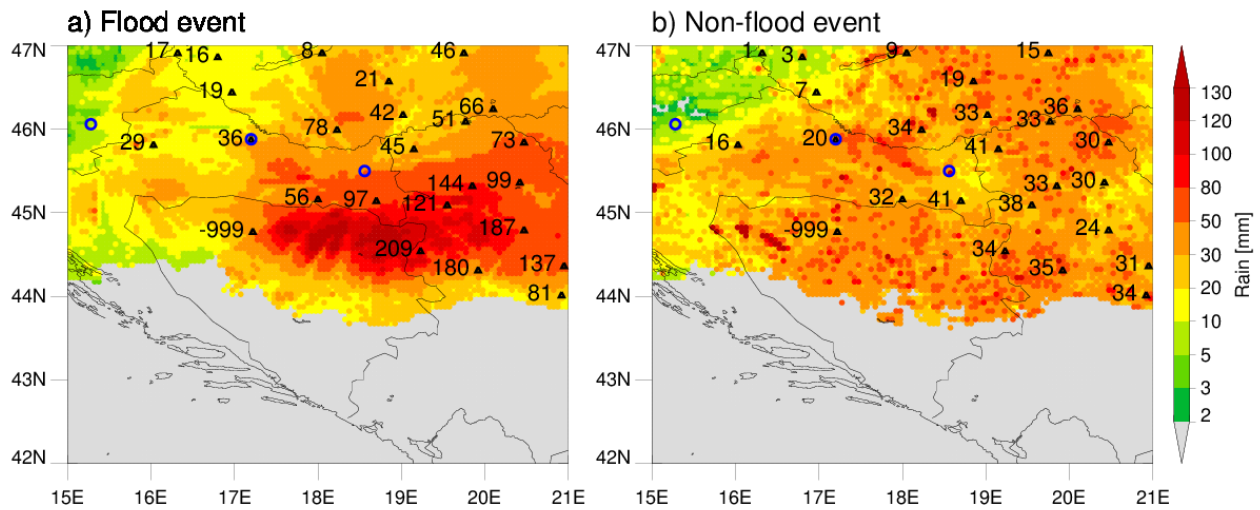
Figure 2.3 A 3-day rainfall accumulations over the flood region for the Balkan flood event (May 14th – 16th) – (a), and the average (non-flood) 3-day period (May 1st – 3rd) – (b). Color bar corresponds to the OPERA measurements; ground rain gauges readings are labeled next to their locations (black triangles) with more details in Table 2.2; blue circles point radar locations.

22
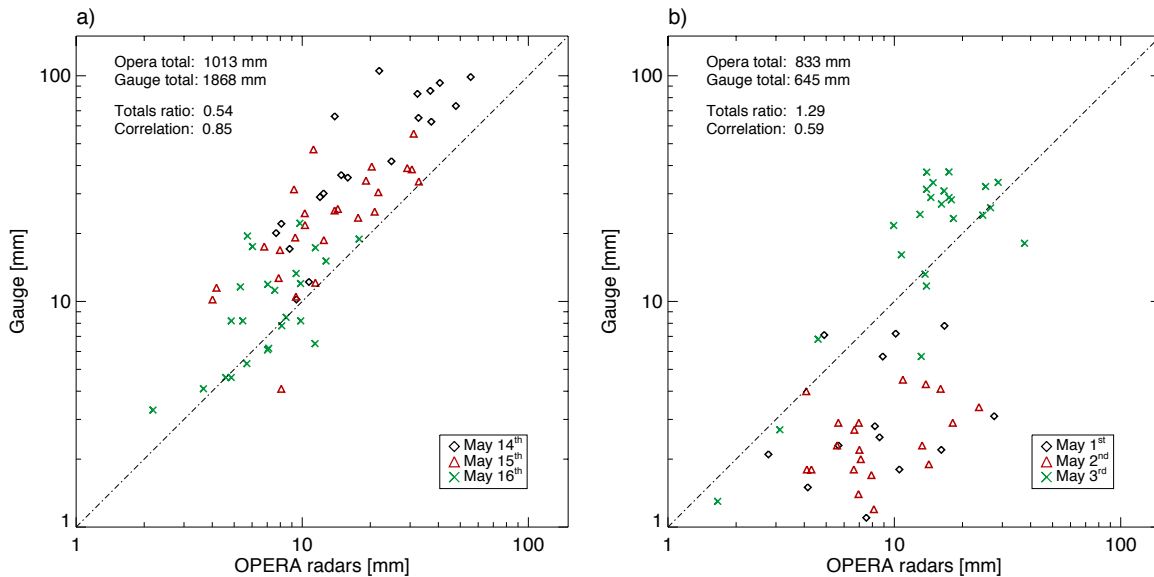
Figure 2.4 Comparison between 25 gauge and OPERA 24-hour rainfall accumulations (diamonds – May 14th, triangles – May 15th, crosses – May 16th) in the Balkan flood event – *panel a*, and in the average (non-flood) 3-day period (May 1st – 3rd) – *panel b*. Note log-axes on both plots.

Analyses show that the ground radars tend to underestimate gauge accumulations by a factor of 2 during the flood event but overestimate the same gauges by a factor of 1.3 during the average non-flood event. Similar result for May 2012 and May 2014 is reported in Lopez 2014 who compared the OPERA monthly mean products against ground gauges in this region. If rain gauges are treated as more accurate measurements, the fact that OPERA radar retrieval assumes constant particle size distribution (i.e. Marshall-Palmer with Z= 200R$^{1.6}$) during both events implies that the difference in the precipitation regimes (e.g. DSDs) is the key variable to alter the radar to gauge ratio. This is further corroborated by the fact that radar to gauge biases are relatively constant over the wide range of rain rates during the flood event characterized by tropical-like environment as evident from the mean 00 UTC and 12 UTC Belgrade soundings shown in Fig. 2.5. Conversely, variations in the bias on daily-scales are highly correlated with precipitation type during the average non-flood event. In

Fig. 2.4b during the first two days, the bias is opposite to that found on the third day, following the change in the precipitation regime from isolated intense storms to a more organized mesoscale convection (see Section 2.2). Studies such as Petersen *et al.* (1999) and Cifelli *et al.* (2011) provide detailed understanding of drawbacks related to the use of radar products that rely upon average Z-R relationship ($200R^{1.6}$) in "tropical-like" environment conditions seen during the Balkan floods event and a number of Front Range flooding events in Colorado. Therefore, based on 25 gauges collocated with radar measurements, an adjusted Z-R relationship for each 24-hour interval of the two events was calculated (see Table 2.3) and used to form the gauge-adjusted OPERA estimates. For simplicity, this calculation keeps *b*, the exponent of the original Marshall-Palmer Z-R relationship ($Z=a\mathrm{R}^{b}$), constant. Significantly lower values of coefficient *a* during the flood event (Table 2.3) imply that the two events were characterized by different precipitation regimes. Sharma et al. 2009 show that an increase of the coefficient *a* is associated with transitioning from stratiform to convective regimes. Also, the coefficients of adjusted Z-R relationship during the flood event are similar to those used in Gochis et al. 2014 for tropical-like environment (Fig. 2.5) to match the Front Range flooding regimes in Colorado.
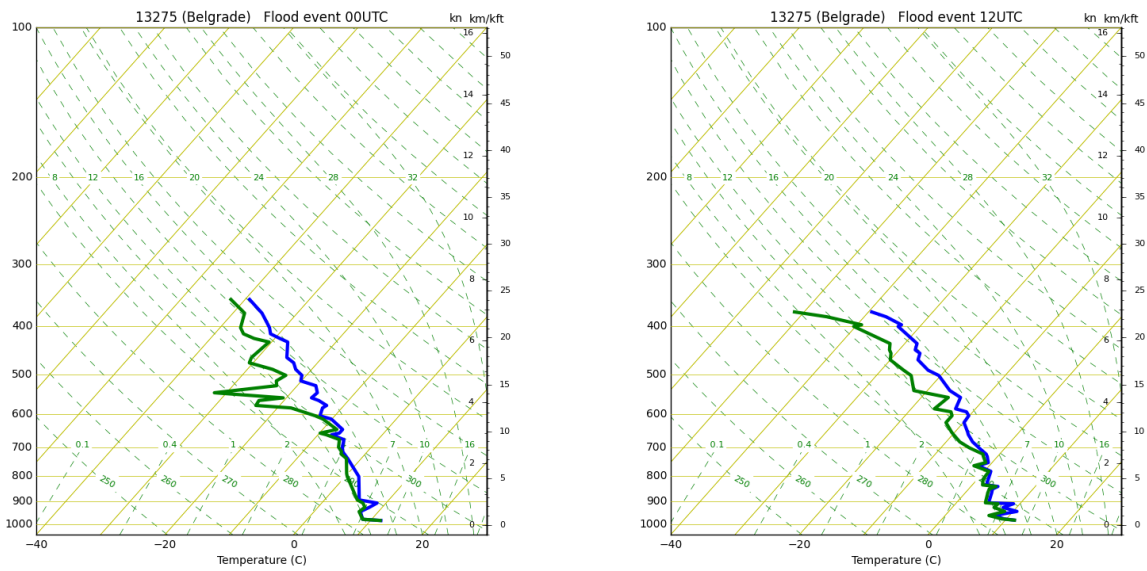
Figure 2.5 Flood event mean sounding for Belgrade (WMOid: 13275; for location see Fig. 2.1). Temperature (blue) and dew point temperature (green) profiles represent the average of 3-day 00UTC (left) and 12UTC (right) soundings in period 14th – 16th May 2014.

Table 2.3. OPERA to gauge ratio and corresponding gauge adjusted Z-R relationship for the two 72-hour events. Calculations are made using Marshall-Palmer DSD parameter constant ($Z=200R^{1.6}$) and basing the adjustment on comparison of rain accumulations between 25 gauge stations and coincide OPERA radar estimates.

Period	OPERA/gauge ratio	Adjusted Z-R relationship
Balkan flood event		
14th	0.52	70 $R^{1.6}$
15th	0.46	58 $R^{1.6}$
16th	0.56	79 $R^{1.6}$
14th – 16th	0.52	70 $R^{1.6}$
Average non-flood event		
1st	3.0	1160 $R^{1.6}$
2nd	3.6	1553 $R^{1.6}$
3rd	0.71	115 $R^{1.6}$
1st – 3rd	1.12	240 $R^{1.6}$

2.4.2 Satellite constellation to ground radar comparisons

Five microwave imagers made 29 overpasses over the region during the 3-day extreme precipitation event (May 14th – 16th) and 28 overpasses during the regular non-flood event (May 1st – 3rd). Visual inspection of each overpass rain rate field in its native spatial resolutions provided qualitative comparisons between satellite and ground radar estimates. An example is given in Fig. 2.6 where corresponding measurements of OPERA network (Fig. 2.6 top) and GMI (Fig. 2.6 bottom) sensor for 2015 UTC 15 May 2014 are shown. Black shaded regions are the same as in Fig. 2.1 while the satellite swath is shaded in gray and outlined by a black-yellow line.
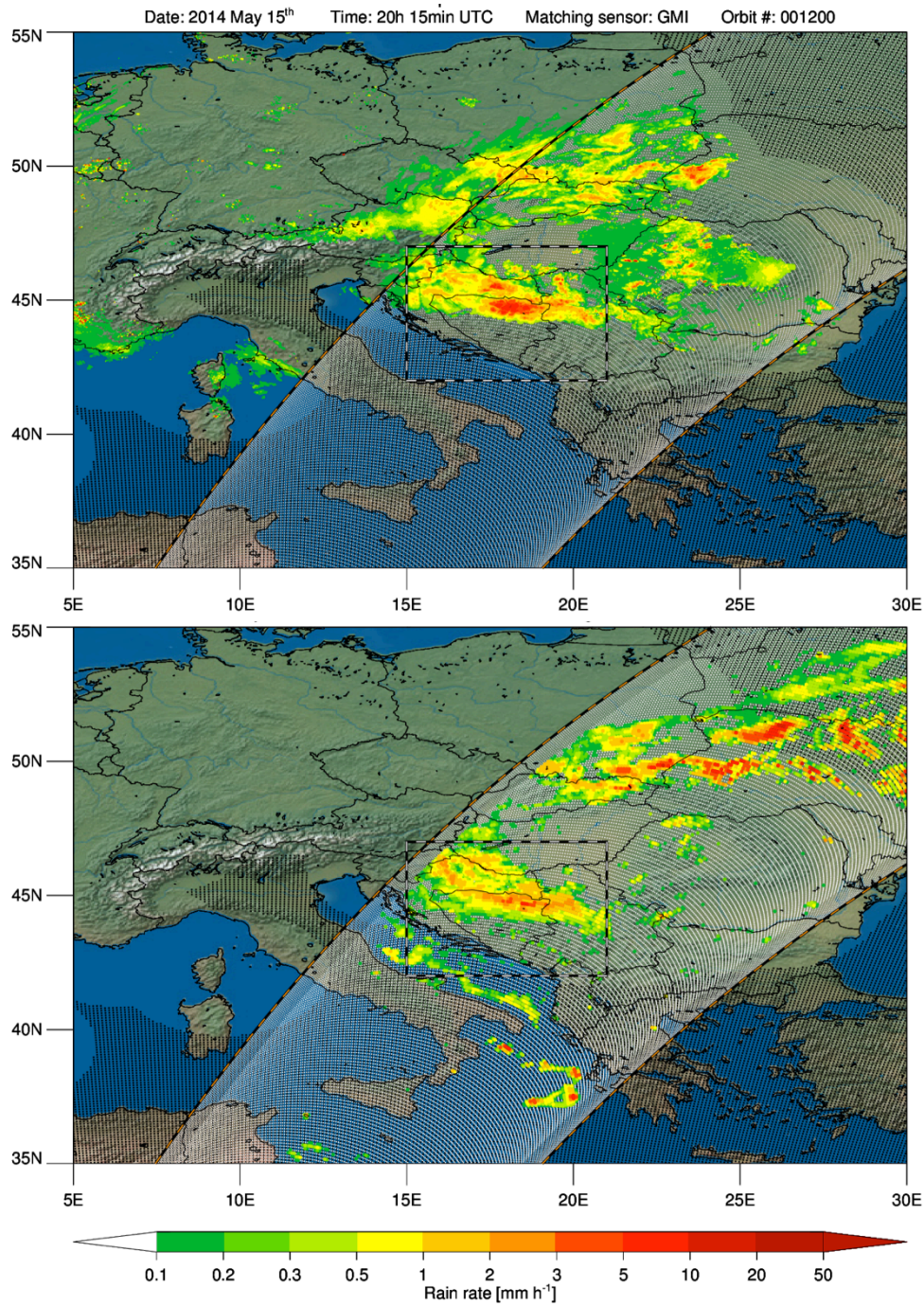
Figure 2.6 *Top:* **OPERA composite surface rain rate for 2015 UTC 15 May 2014. Black shading marks radars range; black-white line outlines flood region; white shading with black-yellow limits denote coincided GMI swath.** *Bottom:* **Corresponding GPROF (GMI orbit 1200) near surface rain rate**

If one focuses on the northern half of the flood area to ensure the best performance of the OPERA radars and to avoid mountainous regions in the south, one can conclude that satellite and radar estimates match very well. Both precipitation system size and distribution of rain rates are in good agreement between the instruments, despite the fact that the two products come from sensors that utilize different vertical sampling, with satellite estimate based on atmospheric integrated column properties at a relatively large slant angle in contrast to radar beam volume sampling. Slant angle of the GMI radiometer results in some displacement of the precipitation features edges and convective cores but within expected ranges. A more detailed examination that includes regions outside the flood box, however, reveals that GMI often misses light rain rates (less than 0.2 mm h^{-1}) as well as intense precipitation cores associated with isolated convection. The radiometer's insensitivity to light rain is expected since the low rain rate scenes are expected to be radiometrically very similar to the non-raining ones, while the underestimation in the deep convective cores is likely due to Bayesian averaging. Examples of side-by-side comparisons between the other four sensors and OPERA data focusing on the flood region only during the extreme event are shown in Fig. 2.7. Except for the higher spatial resolution of the GMI and AMSR2 sensors relative to the DMSP sensors, the same conclusions as in the GMI case hold. Overall, GPROF_2014 shows qualitatively good performance in capturing the spatial variability of the rainfall field when compared to ground radar measurements. The same conclusion was made upon examination of the non-extreme event (not shown here).
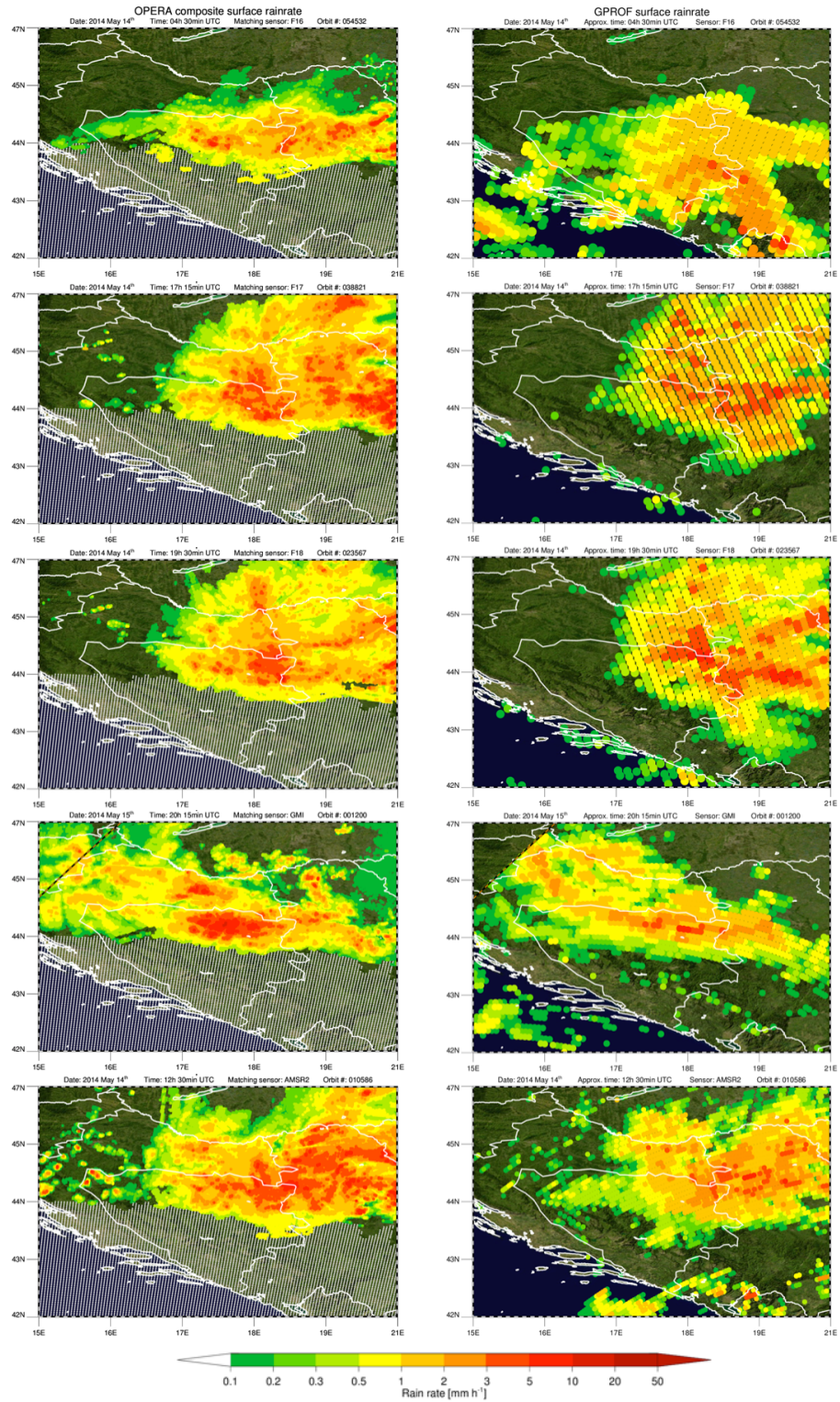
Figure 2.7 *Left column:* **OPERA composite surface rain rates over the flood region at the time of the closest overpasses of SSMIS (onboard F16, F17, F18), GMI and AMSR2 sensors, with corresponding orbit numbers: 54532, 38821, 23567, 1200, and 10586, respectively. Shaded in white: region with no valid radar retrieval.** *Right column:* **corresponding GPROF near surface rain rates.**

Quantitative comparisons between satellite- and ground-based measurements are given in Figs. 2.8 and 2.9. Figure 2.8 depicts timelines of the area-mean total accumulation over the flood region at 15-min temporal resolution for each dataset during the flood (panel *a*) and non-flood event (panel *b*). Satellite observations (black line) are compared to: i) collocated ground radar measurements (red line), ii) ground radar measurements over the entire flood region using OPERA's native (15min) temporal resolution and a Z=200 $R^{1.6}$ relationship (yellow line), and iii) gauge-adjusted radar measurements using 24-hour Z-R relationships given in Table 2.3 (green line). The red line represents simulated satellite observations given by the ground radars, while the green line serves as a reference for "truth" for the size and scale of the events over the entire region of interest. The differences between the OPERA overpass match (red line) and OPERA native resolution (yellow line) exist due to their different spatial extend. The two lines address slightly different areas, being more apart when satellite's FOV captures only a small portion of the flood region.
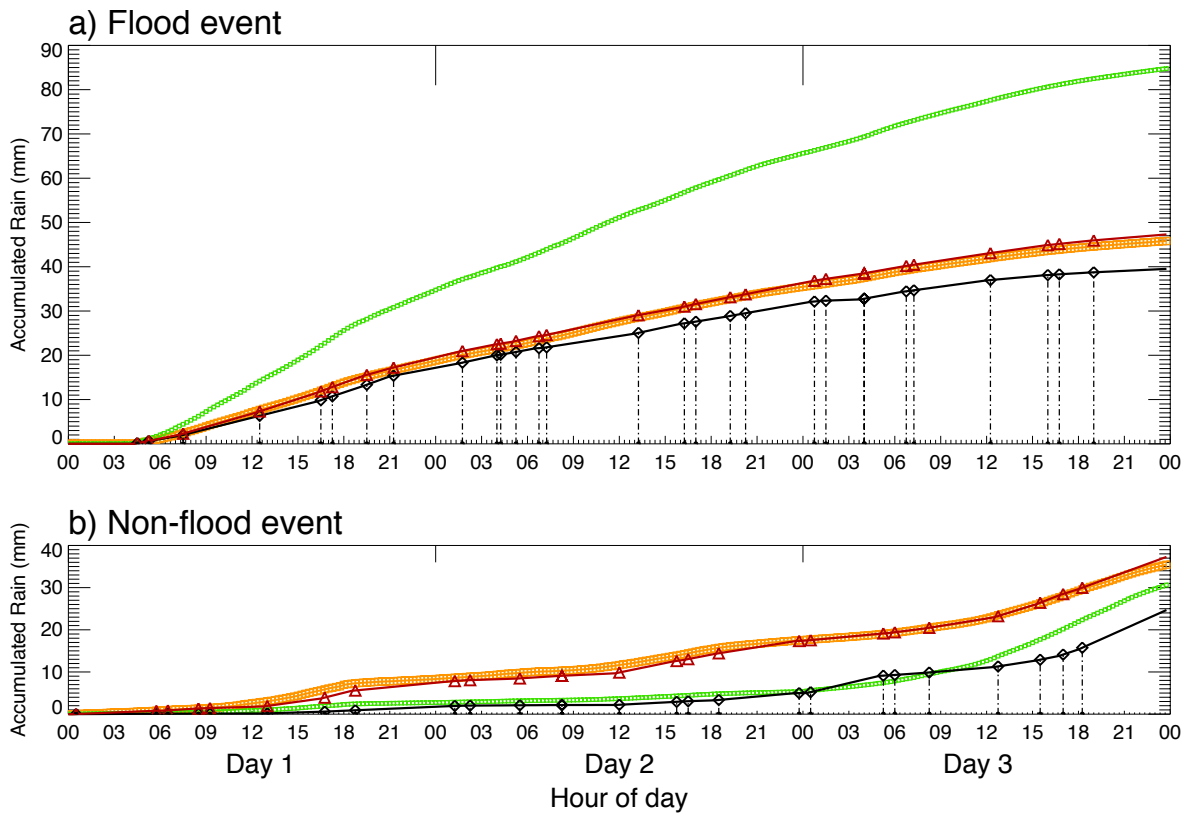
Figure 2.8 Timelines of the area mean rainfall accumulations for the Balkan flood (panel a) and the non-flood (panel b) event. Satellite estimate is given in *black* with symbols marking the individual sensors overpasses; *Red* - OPERA observations at the time of satellite overpass only; *Yellow* - OPERA observations in full temporal and spatial resolution; *Green* - OPERA gauge-adjusted observations in full temporal and spatial resolution (adjusted Z-R relationship is given in Table 2.3).
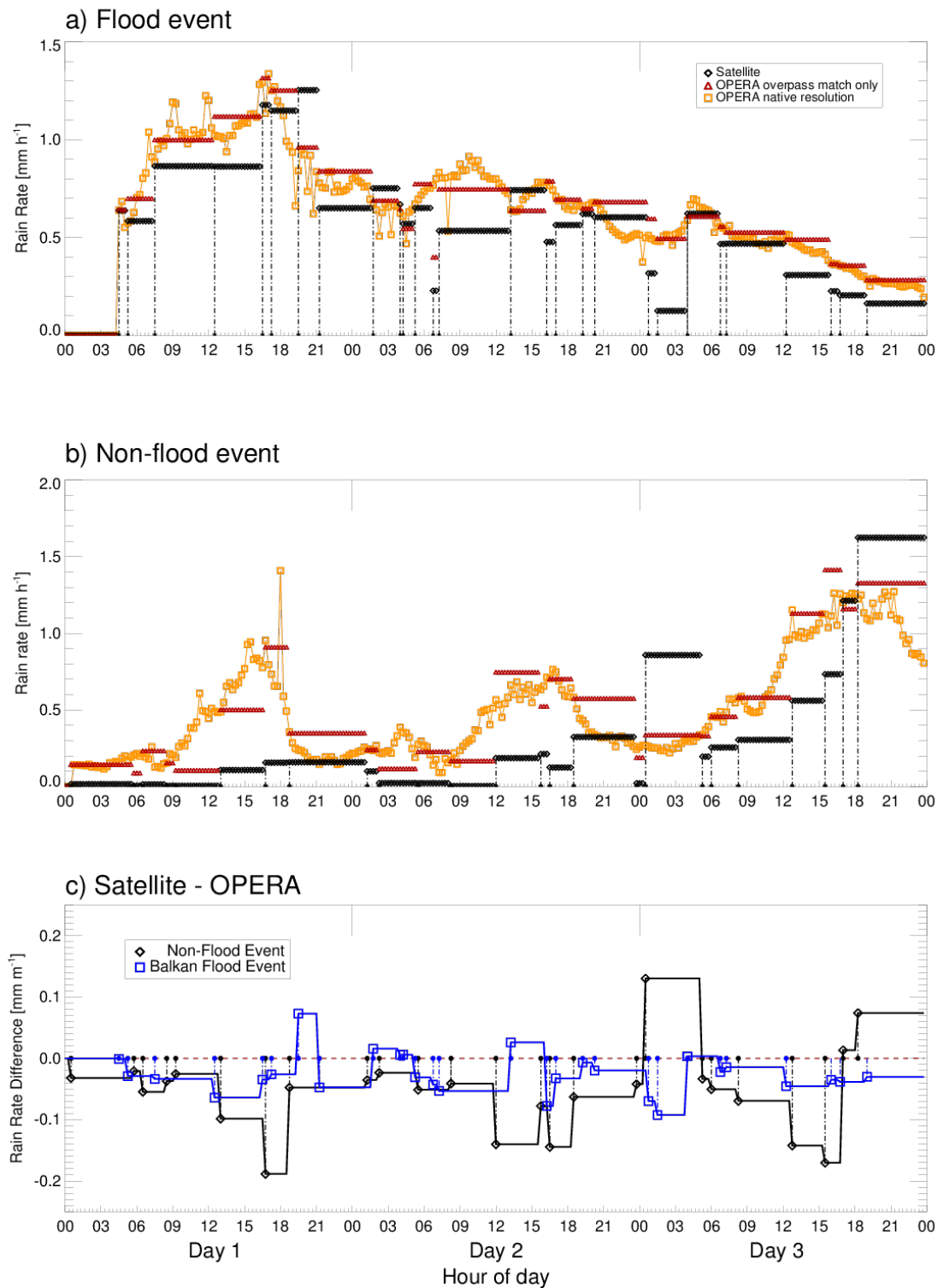
Figure 2.9 Timelines of the area mean rainfall rate for Balkan flood (a) and an average (b) event with their differences (c). Colors have same meaning as in Fig. 2.8 with differences (c) given in blue for the flood event and in black for the average non-flood event.

It is evident from Fig. 2.8 that the radar observations at the satellite overpass times (red) are almost identical to 15 min radar full-coverage over the region (yellow). This indicates that the constellation provides sufficient spatial and temporal sampling to capture all of the rainfall variability over the region for this event. The fact that satellite accumulation (black) in both events fairly closely follow in shape the gauge adjusted accumulation (green), with correlation of 0.99 between the two, indicates that constellation's sampling and performance is capable of addressing a life cycles of both extreme and non-extreme events. To support previous conclusions and point the origin of the observed differences in rainfall accumulations, detailed comparisons of area-mean rain rates are performed and presented in Fig. 2.9.

Studies that compare radar and radiometer products indicate that the differences in their rain rate estimates stem primarily from the assumptions the algorithms use to relate the observed quantities to rainfall rates. As mentioned earlier, the satellite retrieval is built upon the observed ice scattering signal. Similarly, OPERA radar rain rate estimates rely on the Marshall and Palmer Z-R relationship. Therefore, to the first order, differences in the magnitude of the rain rate between the satellite and ground radar retrievals can be caused by: 1) inappropriate choice of Z-R relationship in radar retrievals, and 2) non-representative storm structures populating the *a priori* database.

Based on Table 2.3 and Fig. 2.4, the fact that radar reflectivity is proportional to the sixth power of the rain drop diameter ($Z \sim D^6$) suggests that the DSD was dominated by smaller drops (compared to Marshal-Palmer mean drop size) during the flood event and the third day of non-flood event. Consequently, radar retrieval underestimated gauge-adjusted rainfall accumulation in these well-organized systems relating observed Z to lower rain

rates. On the other hand the first two days of the non-flood event, characterized by isolated intense convection, appear to consist of DSD with mean drop diameter somewhat larger than expected by standard Marshal-Palmer. This difference in the DSD during the two events is likely linked to microphysical properties of isolated and organized convection regimes (Rosenfeld and Ulbrich 2003, Bringi *et al.* 2003). It is known that inappropriate hydrometeor profiles lead to underestimation by passive microwave radiometer algorithms (Kwon *et al.* 2008, Kubota *et al.* 2009, Ryu *et al.* 2012, Sohn *et al.* 2013, Shige *et al.* 2013, 2015, and Taniguchi *et al.* 2013). While not proven for the events in this study, one can infer that the general findings related to precipitation systems organization hold, saying that more organized systems appear to have smaller drops and less pronounced ice scattering signal for the same rain amount than the isolated convective storms of similar or greater top height. This would explain the satellite's underestimates during the flood event and the last day of non-extreme event, both described as well-organized regimes with presence of ice phase. However, the amplitude of this negative bias is related to both event's intensity and a complex link between the environment and rainfall profiles in the database (contributions of the two are quantitatively described in Section 2.4.4). Figure 2.10 depicts the distribution of the *a priori* database profiles for the environmental conditions observed during the Balkan flood event over the vegetated surface type accounting for 60% of the area over 90% of the time. Colors represent the density of database entries within a given rain rate and Tb interval, while magenta and black crosses mark satellite retrieved and ground gauge-adjusted observed values, respectively. While the correct answers appear to be represented in the database, the algorithm favors lower rainfall rates underestimating the observed rain by 50% (as seen in Fig. 2.8) for the given environmental conditions.
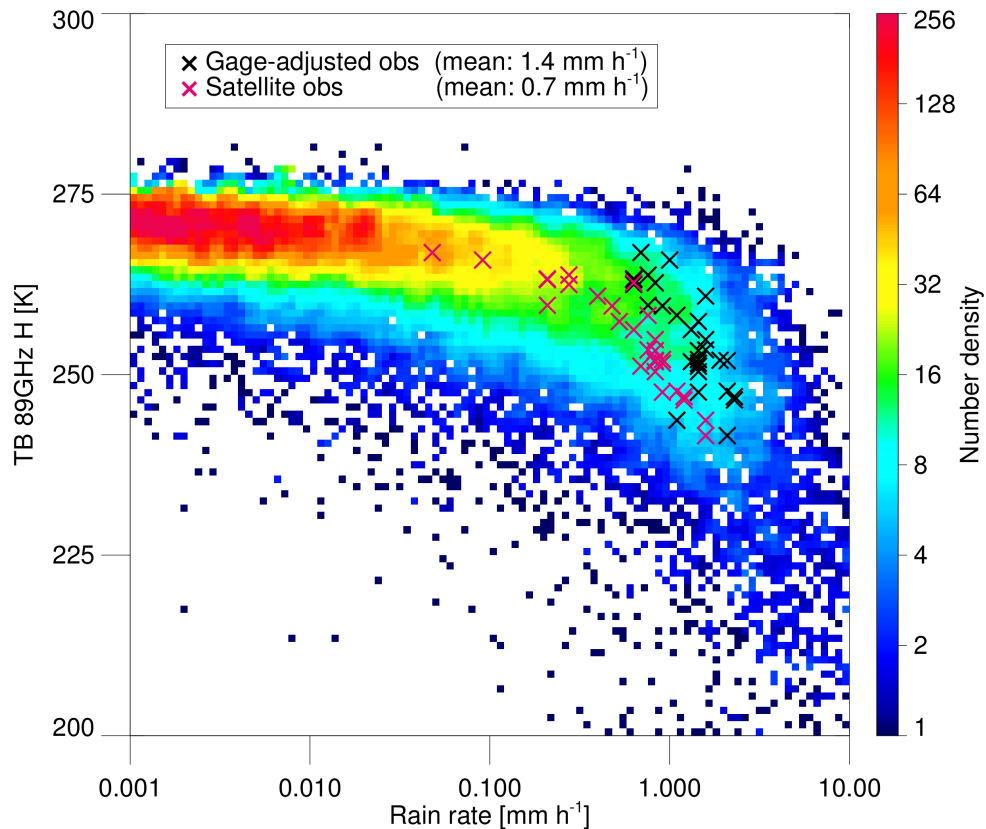
Figure 2.10 The prevalence of the *a priori* database rain profiles relative to 89GHz horizontal brightness temperature (color shades). Profiles correspond only to the predominant surface type (60% of area) of the Balkan flood region and the most commonly observed skin temperature (275 – 285 K) and total column water vapor values (14-23 g kg⁻¹) during the flood event. Area-mean ground radar gauge-adjusted observations and satellite retrieved vales of rain rate are marked in black and magenta crosses, respectively. Note that the x-axis is log-scaled.

The mechanics of the Bayesian scheme itself account for two primary sources of bias: 1) a Bayesian pull towards the *a priori* database mean, which is more pronounced when the information content is low, and 2) incorrect or underrepresented microphysics in the *a priori* database relative to the extreme event. While the pull towards the database mean is expected by definition of the extreme event, the latter can be explained by the fact that, perhaps, the US NEXRAD-based database builds on storms specific for the US region with microphysics different from the one that took place during the Balkan flood event. In

addition, the link between rainfall profiles and environmental conditions used to constrain the database (e.g. skin temperature and total column water vapor) may not be suitable for events such as Balkan flooding. Thus, regardless the fact that the observed profiles exist in the database, the retrieval failed to recognize them as the most likely solution. Comparison of the observed Tb profiles with profiles that the *a priori* database links to the gauge-adjusted rain rate values showed significant differences in ice-scattering signatures. Mismatch of approximately 10 K at high frequency channels (i.e. 91GHz) implied ∼ 40% more ice in the column during the flood event than the database entries for the observed environmental conditions suggest. A more quantitative comparison between the bias contributors (i.e. Bayesian averaging vs. microphysics) is given in the discussion section.

2.4.3 DPR to ground radar

To further address GPM's microwave imager constellation potential, and to verify that precipitation regimes play a key role in the gauge to satellite discrepancies, DPR measurements are introduced (Seto *et al.* 2013). The DPR's attenuation-based retrieval (Iguchi *et al.* 2000, 2009) adjusts its Z-R relationship to the observed precipitation regime though a number of steps that include effects of rain type, presence or absence of a bright band, and the phase state, all of which in essence relate a chosen Z-R relationship to the environment and thermo-dynamical processes of the system. It is worth mentioning that this algorithm, originally developed for the TRMM (Kummerow *et al.* 1998) precipitation radar (PR), is under an incremental development process for the use in the mid-latitude rainfall systems. Thus, although adjustable, the initial *Z-R* relationship is likely biased towards tropical environment characteristic by smaller mean drop size (lower Z) and larger rain rate (high R) than typically seen in an average mid-latitude regime.

Due to relatively small sample size (only four overpasses during the flood period and five overpasses during the non-flood period) comparison between OPERA radar network and DPR products was extended beyond the flood region. Thus, DPR comparisons do not relate exclusively to the events but rather to a much larger, though from a synoptic perspective still similar, precipitation region. This broader comparison partially emphasizes the role that OPERA's fixed Z-R relationship plays in defining the gauge to radar biases.

The comparisons of GMI and DPR to ground radar measurements over the OPERA domain for four (five) satellite overpasses for the extreme (average) event is shown in Fig. 2.11a (2.11b), with the summary of pixel level analysis given in Table 2.4. Overall the results show reasonably high correlation between the satellite and ground data, especially considering the fact that random satellite overpasses and differences in scanning geometry prevent the exact colocation between OPERA and DPR volumes. However, while DPR and OPERA reflectivities (not shown here) match very well in both events, their rainfall accumulations differ significantly. During the flood event the DPR to OPERA ratio is close to that of the gauge to OPERA, implying a good match between satellite and gauge data, but a similar ratio is also seen during the average event when DPR greatly overestimates gauges. Possible explanation may lie in the lack of the full dual-frequency impacts on the day-1 algorithm being used here.
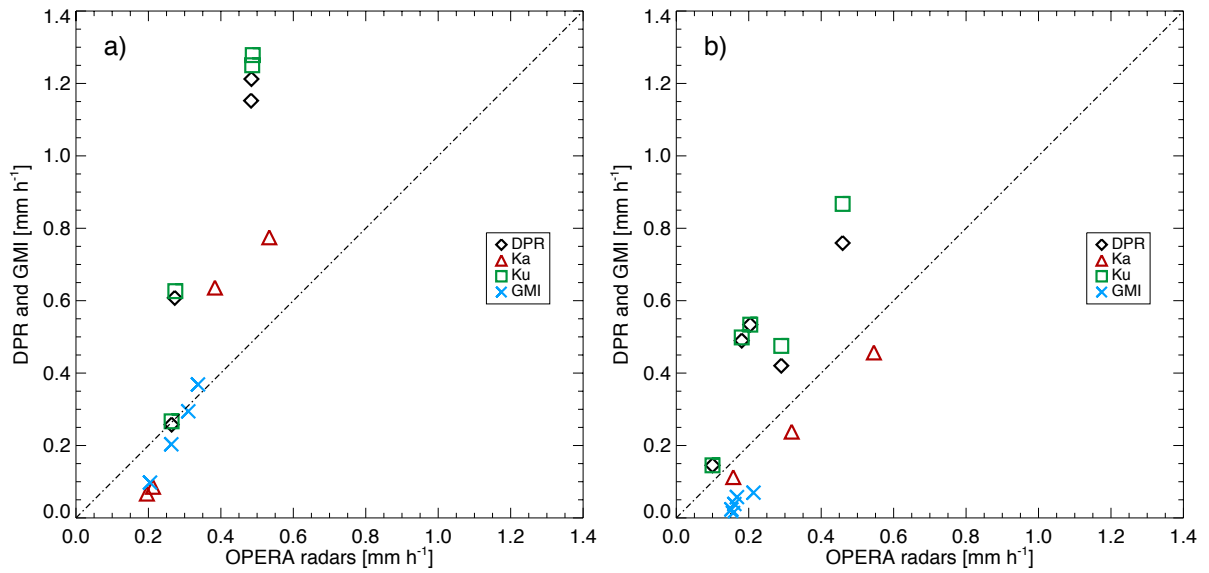
Figure 2.11 DPR/GMI to OPERA rainfall rate comparison. For conditional satellite rain, in nine GPM core-satellite flood-region overpasses, an average rain rate of: DPR, Ku, Ka and GMI sensors is compared to ground radar observations over the entire OPERA domain. Results in panel a) include four overpasses occurred during the 3-day interval of the Balkan flood event (May 14th – 16th), while panel b) depicts the same comparison made during the average (non-flood) event (May 1st – 3rd). Table 2.4 contains corresponding quantitative comparisons.

Table 2.4. Summary of comparisons between collocated ground (OPERA) and satellite (DPR/GMI) rainfall estimates shown in Fig. 2.11 given by using a total rain. The difference in total rain between the sensors is a consequence of sensors swath size.

	DPR	Ku	Ka	GMI
Balkan flood event				
OPERA total rain (mm)	345	345	128	1871
Satellite total rain (mm)	793	834	185	1626
Ratio	2.30	2.42	1.41	0.86
Correlation	0.52	0.50	0.65	0.49
Average non-flood event				
OPERA total rain (mm)	104	104	37	270
Satellite total rain (mm)	171	191	29	256
Ratio	1.64	1.83	0.80	0.94
Correlation	0.51	0.59	0.52	0.28

A more detailed investigation of DPR precipitation profiles (using GPM 2A.DPR product)

addresses the contrast in precipitation regimes of the two events. According to DPR

observations over the flood region only, the flood event is characterized by an average

freezing level height of 1700 m, a near surface reflectivity ranging from 30 dBZ to 35 dBZ,

and 95% of total rainfall being classified as stratiform. On the other hand, the stratiform

portion of the total rain during the average event is 70%, with a mean freezing level at

approximately 2700m and near surface reflectivity in range from 27 dBZ to 32 dBZ. A high

ratio of stratiform-to-convective rain, and an increase in reflectivity below the brightband

seen during the food event are common for intense stationary flood-related regimes. Gochis

et al. 2014 offer extensive analysis on The Great Colorado Flood of September 2013 showing

precipitation profile signatures that are in many aspects similar to those presented here.

2.4.4 Discussion

As suggested above, one can conclude that the radiometer underestimation of the flood

event as well as the organized convection accumulations are caused by: 1) a Bayes' pull

towards the *a priori* database mean, and 2) a non-flood microphysics of the *a priori* database

rainfall profiles. In the second case the entire database appears to be biased towards

different type of raining systems characterized by different ice-to-rain relationship form the

observed one. This scenario results in biased rain rates regardless of their value since the

algorithm links observed Tbs to rain rate values that are not related to the scene being

retrieved. For the first problem, on the other hand, the distribution of database's rain rate is

such that the observed values are found only at its tail and thus, given the mathematics of

the Bayesian retrieval, are underestimated.

Bayesian retrievals, by virtue of retrieving the expected value of the parameter, tend to gravitate towards the center of the distribution. This can cause a Bayesian scheme to underestimate extreme precipitation events. Having an incorrect *a priori* distribution of precipitation, likewise, can lead to over- or underestimation depending upon biases in the *a priori* distribution. To investigate the contribution of Bayesian averaging versus errors in the *a priori* database upon the retrieval's bias seen in the previous section, a synthetic set of rain profiles is generated from the database. This is accomplished by randomly selecting entries from the database with a given surface rain rate to match the observed (gauge-adjusted) probability density function (PDF) of rain rates during the extreme event. These profiles thus have the correct PDF of rain for the extreme event while statistically preserving the microphysics of the database. The retrieval is then run using these synthetic observations, excluding the true answer, which is still contained in the entire database. Thus, any differences between the retrieved and original rain rates in this synthetic experiment must come from the Bayesian averaging. The comparison of gauge-adjusted and retrieved rain rates from this experiment is shown in Fig. 2.12. The retrieval underestimates the original values by 25%. The remaining bias in the retrieval, or roughly 35% of the overall bias, is therefore likely due to the structural differences between observed precipitation systems over the Balkan and those that built the US-NEXRAD database.
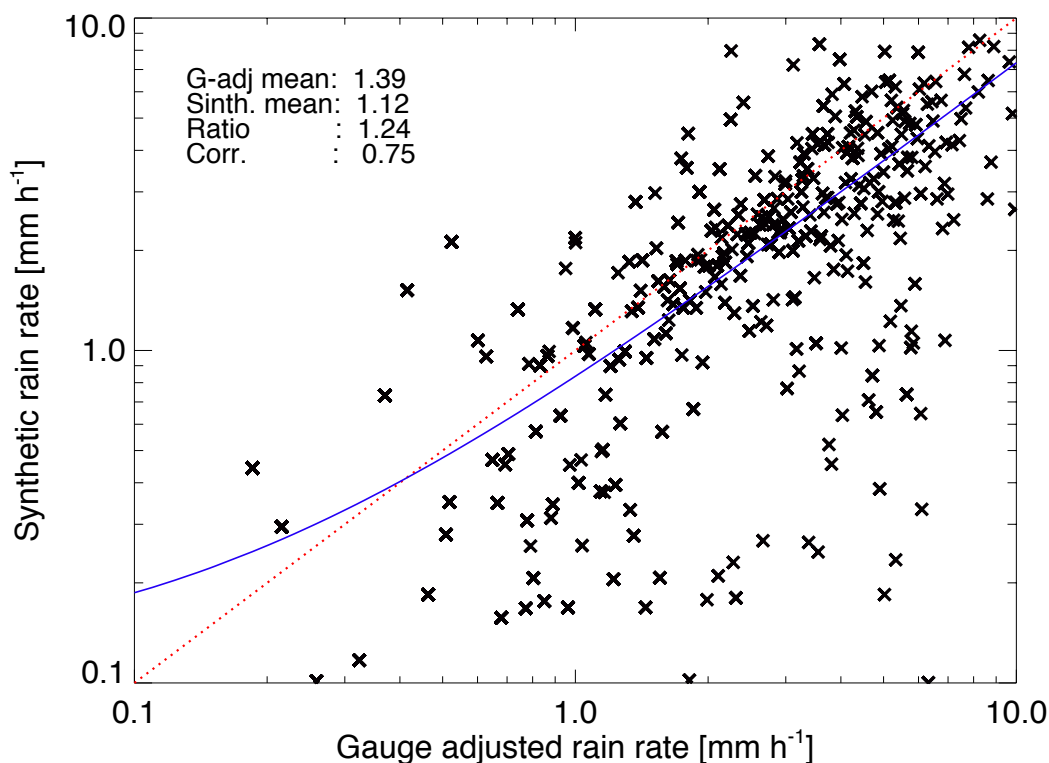
Figure 2.12 Relationship between gauge-adjusted and synthetically retrieved rain rates for six SSMIS-F18 overpasses during the flooding event. Blue line is a linear fit of approximately 2500 rain rates, while red line denotes one to one ratio.

2.5. Conclusions and summary

The performance of the GPM passive microwave retrieval (GPROF_2014.V1-4) in an extreme precipitation event is tested to provide deeper understanding of its potentials and guidelines for its future development. Being an operational retrieval for GPM mission, GPROF serves multiple microwave imager sensors both conical and cross-tracking, with the goal of providing consistent precipitation observations at a wide range of regimes and scales across the globe. Analyzing a 3-day flood event that occurred in the central Balkan region, in addition to an average non-flood event of same duration, this study: 1) provides qualitative and quantitative comparison of retrieval's products against two sets of independent ground

measurements, and 2) offers some insight about the impact of regime dependent microphysics upon these retrievals. The latter is likely to be the key for improving the accuracy of individual and combined satellite products.

The results show that the constellation of five conically-scanning sensors (AMSR2, GMI, and SSMISs on board of F16, F17 and F18) provided sufficient sampling and coverage for the retrieval to closely reproduce rainfall rate and accumulation estimates given by ground radars. However, discrepancies between satellite-, radar-, and gauge 72-hour rain accumulation estimates during the extreme precipitation event reveal that both satellite and ground radars underestimated accumulations relative to gauges by 60% and 50%, respectively. At the same time, relatively high correlations of 24-hour accumulations (0.85) are seen between ground (OPERA) radars and gauges. Additional comparisons related to a more typical, non-extreme, precipitation event of same duration, over the same area, indicated satellite underestimate (20%) and radar overestimate (12%) relative to gauge accumulations. This ambiguous result is explained by OPERA's exclusive use of Marshal-Palmer Z-R relationship ($Z=200R^{1.6}$), which is designed to represent mid-latitude stratiform systems DSD rather than DSDs related to "tropical-like" conditions seen during the Balkan extreme event. A similar explanation holds in the case of satellite retrieval where microphysics from typical rain events (build upon the US NEXRAD observations) leaves an inadequate link between rain rates and corresponding environmental conditions during this extreme event. While upcoming versions of the DPR retrieval will with no doubt implement mid-latitude Z-R relationships, the role of the variability of the ice-to-rain ratio over the broad spectrum of microphysical and dynamical cloud properties related to specific environments remains to be carefully addressed in the future.

CHAPTER 3

UNDERSTANDING THE SOURCES OF SATELLITE PASSIVE MICROWAVE RAINFALL

RETRIEVAL SYSTEMATIC ERRORS OVER LAND

3.1. Introduction and background

The measurement of precipitation from space dates back to the advent of geostationary satellites (Barrett 1970) and their infrared sensors. Techniques for retrieving the surface rain at that time were based on information of cloud top height, whose relationship to surface rainfall was rather ambiguous. The advantage of using microwave frequencies to penetrate clouds was recognized with the introduction of Passive Microwave (PMW) sensors. If sampled across the microwave spectrum (1-300 GHz), surface-originated upwelling radiation detected at the top of the atmosphere (TOA) can offer a valuable insight to the entire atmospheric column. The Special Sensor Microwave Imager (SSMI; Hollinger et al. 1990) was the first widely used multi-channel sensor that allowed rainfall to be detected in a more physical sense. The retrievals used lower frequencies (*e.g.,* 19 GHz) where radiation is absorbed and re-emitted by liquid hydrometeors to derive information of column-integrated liquid water, while the upwelling radiation at higher frequencies (*e.g.*, 85 GHz), strongly affected by ice scattering, offered insight into the upper layers of convective clouds. Thus, PMW retrievals employed both absorption and scattering properties of hydrometeors to relate the observed radiances at TOA to surface rainfall. Despite the improvements, precipitation measurements still suffered from serious discrepancies when

compared to ground-based products (Ferraro 1997). Their inability to fully capture the variability of scattering and absorptive elements within the cloud was seen as the main obstacle for further improvements.

The first spaceborne precipitation radar (PR) was launched in 1997 aboard the Tropical Rainfall Measuring Mission (TRMM, Kummerow et al. 2000), along with the state-of-the-art microwave radiometer (TMI). With high spatial resolution, PR, upon calibration, directly measured the vertical profile of reflectivity, which is proportional to sixth moment of rain drop diameters in the measurement layers. For the first time, PMW measurements could be directly compared to radar's vertical samplings of the atmospheric column, in both time and space. Profiling capabilities of PR allowed for better understanding of hydrometeor absorption and scattering signatures relative to the brightness temperature (Tb) vector by PMW. Ground validation sites, such as Kwajalein, offered valuable ground-based radar rainfall measurements as a reference for both PR and TMI estimates (Kim et al. 2004; Houze et al. 2004; Schumacher et al. 2000). This greatly improved PMW retrieval performance over the ocean where a low surface emissivity ensures a strong contrast between a radiometrically cold background and a warm, precipitation related, atmospheric signature (Ferraro et al., 1995; Kummerow et al., 2001). Consequently, the PMW retrieval output over the ocean quickly came into reasonable agreement with independent estimates (e.g., TRMM ground radar validation sites at Kwajalein, Melbourne, Houston, and Darwin, Wolff et al. 2005). However, comparable agreement was much harder to achieve over land backgrounds (Wolff et al. 2009). Land surfaces are all highly emissive, which leads to Tb emission signatures similar to rain itself. With no obvious contrast between rain and surface-background emission signals, rainfall detection over land is based primarily on ice-induced

scattering signatures (Wang et al., 2009) and its relationship to the surface rain rate (Ferraro, 1997; Ferraro et al., 2013). As will be shown here, this limitation remains one of the greatest challenges in the global rainfall observations over land. TRMM, however, played a key role in revealing many of the PMW retrieval shortcomings including the sensitivity to different geophysical parameters related to rainfall such as variability of the surface emissivity (Ferraro et al. 2013; Petty and Li 2013), as well as the assumptions inherent in the algorithms used to retrieve rainfall from Tb or reflectivity measurements (Kummerow et al. 2011) such as the Drop Size Distribution (DSD) and hydrometeor vertical profile. While many improvements have been made over time [e.g., *Grody*, 1991; *Ferraro et al.*, 1994; *Adler et al.*, 1994; *Conner and Petty*, 1998; *Seto et al.*, 2005, Kummerow et al. 2015], PMW retrievals essentially still rely on ice-scattering signal to retrieve surface rainfall and this relationship, it turns out, is quite sensitive to storm system dynamics.

The modern era of satellite observations emphasizes the importance of understanding this relationship even more thoroughly. The launch of the GPM (Hou et al. 2014) core-satellite, with a dual-frequency precipitation radar (DPR) and the most accurate microwave imager to date (GMI), affords the opportunity to inter-calibrate a multitude of PMW radiometers to the same reference. Blended products of global rainfall measurements, such as Integrated Multi-satellitE Retrievals for GPM (IMERG; Huffman et al. 2014, 2015), are becoming available at 30-min temporal resolution across the globe. Consistent and reliable retrievals over land are thus more critical than ever. Facing the limitation of having to infer surface precipitation from just the ice-scattering signal, this study seeks to better understand such relationships in nature, and explores synoptic-scale structural and environmental

parameters that may be used to characterize this relationship between the ice scattering signal and the surface rainfall.

3.1.1 Accuracy and bases of the PMW rainfall retrieval over land

Validating satellite precipitation retrievals on a global scale is a complex and difficult task (Turk et al. 2002). Recognizing the qualitative performance, fortunately, is much easier. A comparison of TRMM rainfall estimates (PR and TMI) identifies the presence of large-scale systematic differences in the retrievals (Berg et al. 2006, 2008; Yamamoto et al. 2008; Adler et al. 2012; Wang and Wolff 2012; Maggioni et al. 2016; Liu et al. 2016). An example is given in Fig. 3.1, where one year of TRMM data is used to present the difference in mean daily rain rate of the PR and Goddard PROFiling algorithm – GPROF 2010 version 2 (Version 7 for TMI; hereafter referred to as PMW retrieval) algorithms over land. The comparison is made using TRMM 3G68 product, which is an hourly gridded product containing TRMM 2A12 (Kummerow et al., 2001), 2A25 (Iguchi et al., 2000), and 2B31 (Haddad et al., 1997a, 1997b), precipitation estimates (note that this is not a standard TRMM product). Inspection of Fig. 3.1 reveals two types of problems: 1) surface contamination (e.g., Himalaya region), and 2) mean-biases with a significant random component over large regions. The most pronounced error corresponds to regions in the Himalayas. This, however, is a surface-screening problem where the upwelling microwave signal, depressed by accumulated snow and ice on the ground, is erroneously related to the rainfall by the PMW retrieval. This is easily verified using the PR profiles, which show that the majority of PMW "precipitation" events are not associated with any echo in the atmosphere over this region. In the past, PMW algorithms have employed a number of screening steps taken prior to the retrieval process to avoid this misinterpretation (Ferraro et al. 1998; Kummerow et al. 2001; Gopalan et al. 2010; Meyers

et al. 2015). In its most recent version, GPROF (Kummerow et al. 2015) uses daily snow cover updates to ameliorate this problem. This has improved precipitation screening over regions with snow on the ground, resulting in systematic differences that are significantly lower than those seen in Fig 1 (not shown here). Surface screening errors, however, are not the topic of this study. To avoid any contamination by this type of scattering signature, the focus of this paper is on tropical regions marked in Fig. 3.1 that show opposite PMW-to-PR systematic differences but have very similar surface backgrounds. Tropical Africa and South America stand out (highlighted in Fig. 3.1) although a similar dipole is seen in Australia, as well as over Southeast Asia, and the Central and Eastern United States. While both PR and PMW retrievals may be contributing to this disagreement, the PMW algorithm must rely on ice-scattering signatures only and is thus less reliable than the radar retrieval. The focus of this study is therefore on PMW retrieval and the potential elements that contribute to these systematic differences.
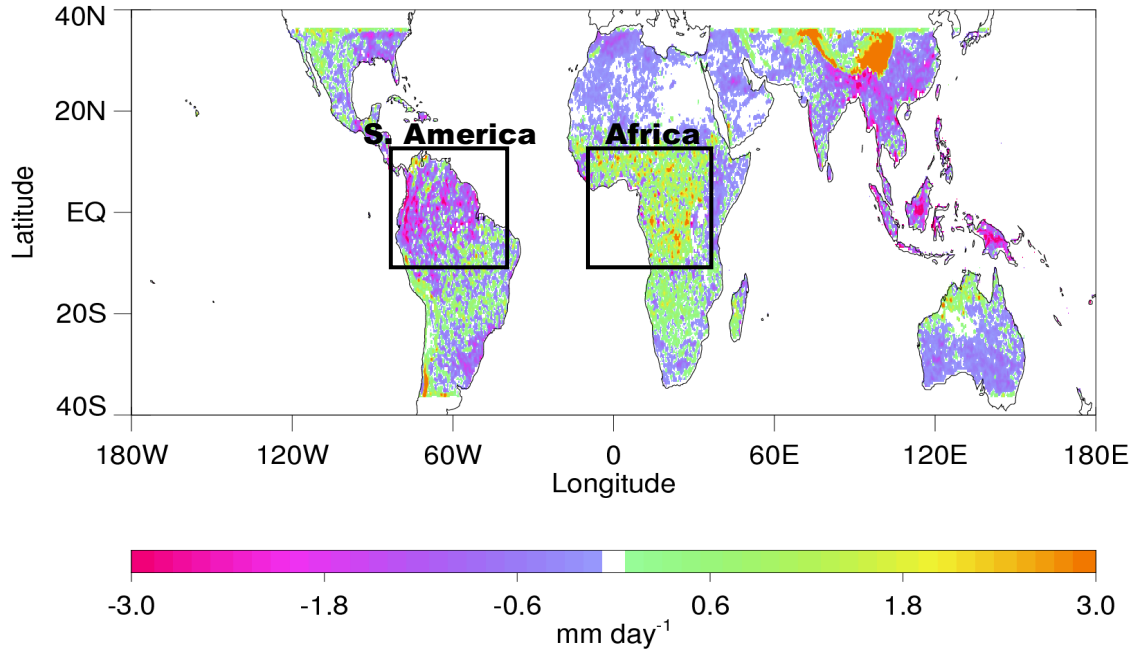
Figure 3.1 Mean daily rainfall differences between PMW (TMI) and PR sensors (TMI-PR) for 2008 on a 0.5° grid of the 3G68 product. The figure reveals regions where PMW retrieval (GPROF2010 version 2) underestimates and overestimates PR observations.

Before any hypothesis is presented, the actual assignment of rain rates over land surfaces in the PMW retrieval is briefly reviewed (details can be found in Kummerow et al. 2015). In its first step, the algorithm (GPROF 2010) screens out cold surfaces (residual errors from which still appear over Himalayan region in Fig. 3.1) using the methodology described in Meyers et al. (2015). Then, mainly based on the values and spatial distribution of 85 GHz Tb, a convective-stratiform discriminator, described by McCollum and Ferraro (2003) and modified by Gopalan et al. (2010), is added. Once a pixel is determined to be raining and its convective-stratiform nature is known, regression equations relate the 85 GHz Tb depression to the surface rainfall using following relationships:

$$Rain_{strat} \,[\text{mm h}^{-1}] = (1 - cnvprob) \cdot (19.7034 - 0.0708 \cdot Tb_{85v}) \tag{3.1}$$

$$Rain_{conv} \,[\text{mm h}^{-1}] = cnvprob \cdot (165.656 - 1.63 \cdot Tb_{85v} + 6.5035x10^{-3} \cdot Tb^2_{85v} - 9.6682x10^{-6} \cdot Tb^3_{85v}) \tag{3.2}$$

where *cnvprob* is the convective probability, $Rain_{strat}$ and $Rain_{conv}$ are stratiform and convective rain rates, respectively, and Tb_{85v} is 85 GHz vertically polarized channel brightness temperature in [K]. The final rain rate estimate is simply the sum of the two (i.e., *$Rain_{strat}$ + $Rain_{conv}$*). Errors in PMW rainfall estimates over land are thus primarily related to the variability of the surface rain rate relationship to the 85 GHz Tb depression.

It has been suggested that systematic differences over these areas may be a result of the differences between the instruments' capability to detect light rainfall, errors in assumptions about the raindrop size distribution (DSD) in the radar algorithm, or presence of supercooled water. A considerable amount of research has been done on these (*e.g., Olson et al.* 2006; *Yang et al.* 2006; Shige et al. 2006; Seo et al. 2007; Wang et al. 2009). Nevertheless, the regional systematic differences over land remain significant. The possibility that different regions have systematically different ice contents and related Tb depressions for the same surface rainfall has not been sufficiently explored. Therefore, this study will focus on understanding mean-differences over regions of generally similar atmospheric and surface background conditions, but opposite PMW-to-PR differences.

Deeper insight into this problem is offered in Fig. 3.2 using the aforementioned regions of Africa and South America as a test bed. The rainfall ratio (PR/PMW) between raining scenes detected by the two sensors is plotted as a function of rain rate. The black line reflects a mean ratio of the PR and PMW rainfall over the two regions after the overall systematic difference is removed. Focusing to the mean ratio only, one can easily note that PMW retrieval tends to overestimate PR at low rain rates (0-5 mm h^{-1}), while underestimating higher ones (above 5 mm h^{-1}). This is a general property of GPROF retrieval caused by the fact that algorithm has less information content than the PR and thus tends to drive

individual pixels towards the mean solution. However, when the regions are analyzed individually, the ratio is seen to be consistently above (Amazon) and below (Africa) the mean value, suggesting a clear regional dependency of the relationship on the observed vector and precipitation. Thus, according to Eq.'s (3.1) and (3.2) and Fig. 3.2, it can be hypothesized that cloud microphysical properties must be substantially different in storms over the Amazon, compared to the African region.
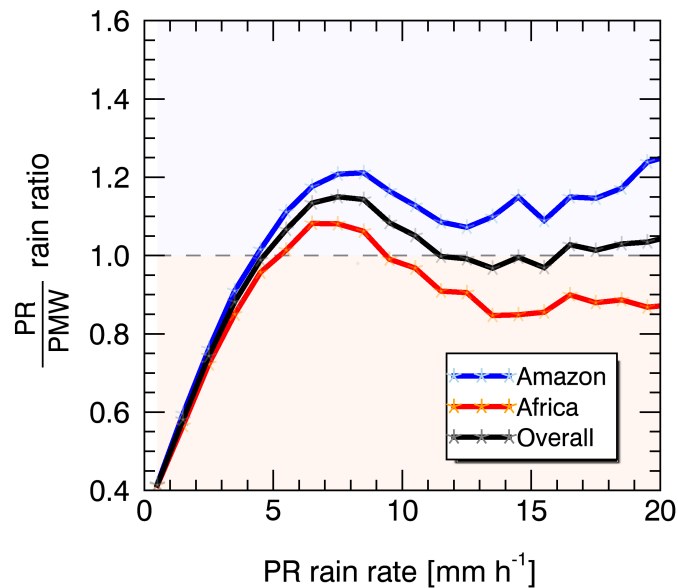
Figure 3.2 PR to PMW rainfall estimate ratio (PR/TMI) as a function of rain rate for Amazon (blue), African (red) and both regions combined (black). Overestimations by PMW retrieval are shaded in light red; underestimations by PMW retrieval are shaded in light blue.

In support of this hypothesis is a global map of annualized distributions of total lightning activity shown in Fig. 3.3 (Stolz et al. 2015). It can be seen that higher lightning densities coincide with strong PMW overestimations over Africa, while lower flash rates coincide with PMW underestimations over Amazon regions of Fig. 3.1. It is known that the majority of rainfall over these regions originates from a structurally different type of system: Meso-scale

Convective Systems (MCSs) (e.g., Toracinta et al. 2001) in Africa, and warmer and shallower storms over the Amazon region. Therefore, it is expected that the microphysical processes and the cloud structure of storms in these regions are likely different as well. Other areas with similar surface types but opposite systematic differences (e.g. East/West US) may have different lightning density ratios compared to the Amazon-Africa example. However, this can be explained by the fact that cloud microphysics and structure are influenced by a number of factors such as topography, mesoscale air masses, and, the large-scale environment. Combined, these factors play a critical role in the lifecycle of storms (e.g., Rasmussen et al. 2016) by suppressing and enhancing the ice-phase, and the associated scattering signal upon which the passive microwave rainfall is predicted. From this perspective, it is worth noting that, in addition to earlier studies (e.g., Williams et al. 1992, 2005; Ba et al. 1998; Gilmore and Wicker 2002; Qie et al. 2003) that showed positive correlations between lightning, microphysics and the amount of passive microwave scattering, the most recent study by Barth et al. (2015), based on data from Deep Convective Clouds and Chemistry (DC3) field campaign, links lightning flash rates to thermo-dynamical drivers of precipitation regimes over the US Great Plains. They found substantial differences in flash rates of storms occurring during periods of high and low values of shear and CAPE. McCollum et al. (2000) compared Global Precipitation Climatology Project (GPCP) data to satellite infrared and microwave rain estimates to find essentially the same discrepancies as those seen in Fig. 3.1. As one possible cause they point that distinct environmental conditions exist over these regions using the observed difference in lightning density as supporting argument.
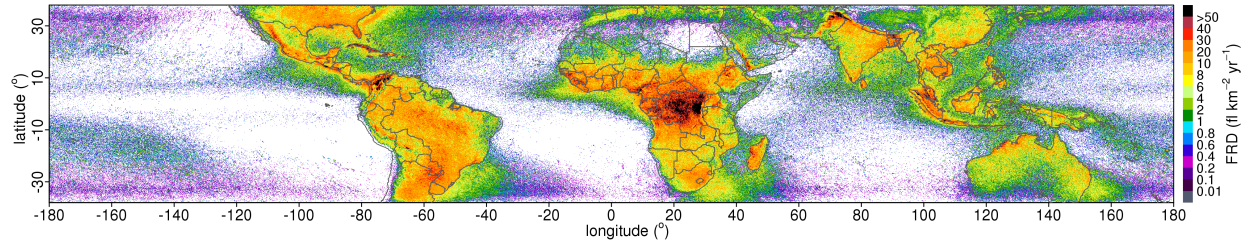
Figure 3.3 The annualized distribution of total (cloud-to-ground plus cloud-to-cloud) lightning activity [flashes km^{-2} yr^{-1}] detected by the Lightning Imaging Sensor (LIS) Very High Resolution Full Climatology (VHRFC) in period 1998-2013. Source: NASA – Global Hydrological Resource Center (GHRC).

In order to assess our comprehension of cloud dynamics and microphysics in the regions described above, this study seeks to understand and identify causes and potential predictors of observed systematic differences of passive microwave precipitation relative to PR estimates. The study will focus on the Amazon and African regions in order to minimize variability due to surface type, proximity to the ocean, and advected air masses.

3.2. Data and precipitation climatology

This study employs one year (2010) of TRMM PR and TMI data to detect regional systematic differences of PMW retrieval (shown in Figs. 3.1 and 3.2), and to provide insight into the vertical structure and character of precipitation regimes. The standard TRMM PR 2A25 product (Iguchi et al. 2000, 2009) provides the attenuation-corrected radar reflectivity (Z_E) profile (every 250m from the surface to 20 km), freezing level estimate, and near surface rainfall rate at the PR native spatial resolution (approximately 5 km). Precipitation type at the pixel level (convective/stratiform) is given by the 2A23 product (Awaka et al. 2009). PMW retrieval surface rain rate estimates and corresponding TMI brightness temperatures are obtained from the GPROF (see Section 3.1.1) standard output and 1B11 product

respectively. An additional year (2008) of the same data sets is used as an independent sample to test the robustness of this study's findings.

Environmental parameters, namely CAPE, wind profile, temperature, dew point and specific humidity are taken from the European Centre for Medium-Range Weather Forecasts (ECMWF) Re-Analysis Interim (ERA-Interim) model data (Dee et al. 2011), at 0.75° horizontal and 6-hour temporal resolution, at 4 pressure levels (850, 700, 500 and 200 mb) for the same two years as the TRMM data. While model-induced uncertainties exist, this dataset is still seen as the best resource based on its consistency, coverage and use in potential applications. Thus, *vertical wind shear* is defined as the difference in wind magnitude at 500 mb and 850 mb levels. *Low-level dew point depression* is defined as the difference between 2 m temperature and dew point. *A vertical humidity deviation* is defined as the ratio between specific humidity at low- and mid-tropospheric levels. To ensure that the height of the planetary boundary layer (PBL) does not affect these results, mid-level humidity is taken as a mean value of 450 mb and 500mb, while low-level humidity is required to be within the PBL (e.g., 850 mb). Three different humidity ratios are defined so that the environment is separated into three equally probable states: i) dry aloft, ii) mean, and iii) moist aloft. The 'dry aloft' profile is defined as a state with a ratio of low- to mid-level atmospheric moisture greater than that of the domain mean profile, while the opposite is the case for 'moist aloft' profile.

This study focuses on land regions in South America (10S-10N; 50W-80W) and Africa (10S-10N; 17W-30E) of approximately equal area, similar surface type and elevations. While a detailed description of data sets used for the analysis can be found in the cited literature, a

brief overview of TRMM instrument characteristics is provided below in addition to the climatology of the Amazon and African regions.

3.2.1 TRMM instruments.

TRMM's precipitation radar is a Ku-band radar operating at frequency of 13.8 GHz with a minimum detectable reflectivity of 17 dBZ. This provides reliable rain rate detection down to 0.5 mm h^{-1} with limited sensitivity to frozen hydrometeors (e.g., fairly large ice particles such as hail and graupel). With a range resolution of 250 m, PR offers vertical sampling up to 20 km above the mean sea level through its attenuation based retrieval (version 7, Iguchi et al. 2000, 2009). Each scan contains 49 5-km FOV pixels forming a swath of approximately 250 km.

TMI measures the microwave radiances with horizontal (H) and vertical (V) polarization at nine channels (10V/H, 19 V/H, 24, 37 V/H, and 85 V/H GHz) with footprint sizes ranging from 63x37 to 5x7 km (Kummerow et al. 1998).

3.2.2 Climatology of precipitation over the Amazon and Central and West African regions

Central Africa is known for deep, intense, well-organized storms that produce as much as 70% of total rainfall in that region. In the form of squall lines and mesoscale convective complexes (MCCs), these storms typically initiate near the Ethiopian Highlands, the Darfur mountains, and Jos Plateau. While propagating toward the Atlantic, they are strongly affected by African Easterly Waves, the African Easterly Jet and moisture convergence in the lower troposphere. The average annual precipitation, ranging from 600 mm to 2000 mm, is unevenly distributed between the dry (October-March) and wet (April-September) seasons (Conway et al. 2009). Detailed descriptions of precipitation systems over Central Africa can be found in studies by Payne and McGarry (1977); Bolton (1984); Tetzlaff and Peters (1988);

Machado *et al.*, (1993); Rowell and Milford (1993); Laing and Fritsch (1993); Novella and Thiaw (2013). Two sub-regions, namely the Sahel (northern-) and the Congo (equatorial-Africa), are often characterized by somewhat different precipitation patterns. A comprehensive analysis of those differences is given by Laing et al. (2011) who emphasize a role that equatorial coupled waves play in development and lifecycle of the MCSs in Central Africa. They point out that, in comparison to their Sahel counterparts, equatorial Mesoscale Convective Systems (MCSs) are often exposed to slowing equatorial Kelvin waves, Madden–Julian Oscillation (MJO) signal, less continental mass, and weaker contribution of local shear. Therefore, while generally very similar, it may be expected that typical precipitation systems in these regions have different structures under the same local atmospheric conditions.

Amazon precipitation preferentially comes in the form of shallow, less intense but persistent systems with more ocean-like characteristics. A dominant feature of the rainfall variability is a diurnal cycle with seasonal contrasts less pronounced than over the African region. Most of the rainfall occurs between November and May. Mean annual accumulation over the majority of the area considered in this study ranges between 1000 and 3000 mm. Detailed analysis of Amazon rainfall systems, including occasional deeper, continental-like systems, is given by Petersen et al. (2002) and sub-cited literature. A literature review of the most important precipitation properties in this region can be found in Dias et al. 2002.

3.3. Understanding the Origins of Systematic Difference in PMW Retrieval

Because the PMW algorithm [Eq. (3.1) and Eq. (3.2)] guarantees similar rain rates for similar Tb depressions at 85 GHz, an error is introduced any time the scattering in a cloud differs from the average assumed relation. Since the 85 GHz brightness temperature

decreases primarily due to ice-scattering (Vivekanandan et al. 1991), it is hypothesized that ice-scattering variability is responsible for the systematic differences in rain rates seen between the two sensors in Fig. 3.1. To test this, PR reflectivity above the freezing level and rain rate over the two regions of Fig. 3.1 are first compared and then linked to a proxy for PMW retrieval rain rate (i.e., 85 GHz Tb depression). Only for this purpose, in order to ensure that 85 GHz Tb depression is not caused by any surface-related sources, such as standing water, a Polarization-Corrected Temperature (PCT) is used. Before the result is discussed, PCT and PR's total reflectivity above the freezing level are defined.

The Polarization-Corrected Temperature (PCT) is a linear combination of the vertically and horizontally polarized Tbs that largely eliminates the contrast between land and water (or wet surfaces). Thus, PCT yields an atmospheric scattering signal whose strength does not depend on the surface background. While a single polarization 85 GHz yields very similar results over the Tropics, the PCT depression is used here as a proxy for ice-scattering to eliminate possible contamination from standing water or wet surfaces. The PCT definition follows that of Spencer et al. (1989):

$$PCT = 1.818\ TB_V - 0.818\ TB_H$$

where TB_V and TB_H are brightness temperatures at the vertically and horizontally polarized TMI 85.5 GHz channels, respectively. To limit variability within TMI's field of view (FOV) and ensure good beam filling, only pixels with PCT colder than 250 K are used (Spencer et al. 1989). This criterion focuses on systems with a robust ice-phase in the precipitating column and excludes scenes that the algorithm has very little sensitivity to.

The Total reflectivity above freezing level (TRFL) is simply the sum total of all reflectivity values in range gates above the freezing level observed by PR. Due to a wide range of hydrometeor properties (e.g. type, phase, density, and size distribution) it provides only a qualitative estimate of the cloud content in the freezing portion of atmospheric column which, due to PR's sensitivity threshold (17 dBZ), mainly relates to large frozen hydrometeors. To estimate this quantity, the freezing level is obtained from the 2A25 PR product and used to locate PR range bins with frozen hydrometeors.

These two diagnostic variables allow for easier verification of the hypothesis that the variability in ice scattering is the dominant error source. Figure 3.4 shows the relationship between the TRFL and rain given by PR. While noisy, the TRFL in the cloud is clearly depressed over the Amazon and enhanced over the African region for a given rainfall rate.
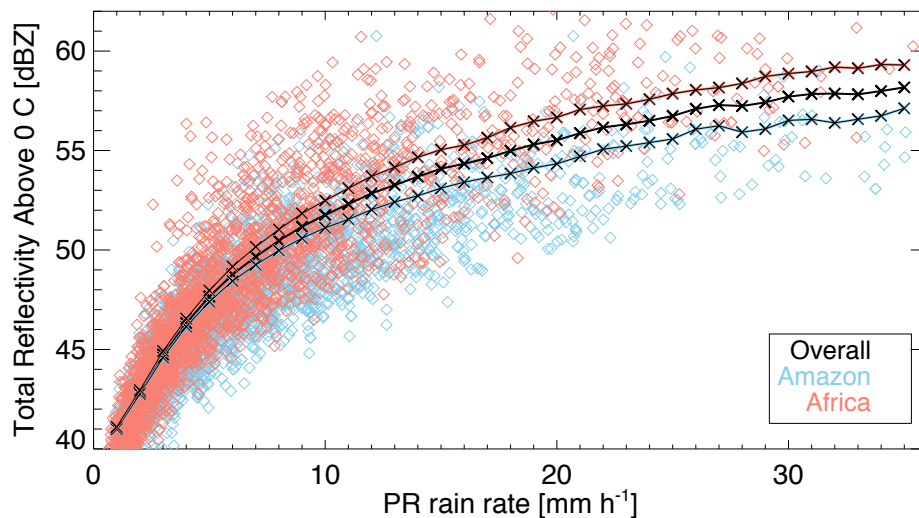
Figure 3.4 Total reflectivity above the freezing level as a function of rain rate. A comparison of the Amazon (blue), African (red) and the overall (black) region (as defined in Fig. 3.1) means. Pixel data are given by diamonds; mean values for each rain rate bin is given by crosses. Note: only 5% randomly chosen pixels are plotted (the means account for full data set) to avoid clutter in the figure.

Alternatively, one can also use the 250 K 85 GHz PCT depression from the PMW instrument as a proxy for ice scattering. Figure 3.5 depicts the relationship between this PCT depression and TRFL for collocated PMW and PR measurements. The comparison takes one year of observations over the two regions marked in Fig. 3.1. Although not perfectly aligned, the two quantities are seen to be related. An increase in PCT depression corresponds to an increase in total reflectivity above the freezing level. Stronger scatter at the bottom of the plot is a reflection of the variability in ice particle size (Bennartz and Petty 2001), as well as in Tb that is caused by liquid-phase particles seen by the radar above the freezing level but not contributing to the PCT depression. As the PCT depression increases, the scatter reduces.
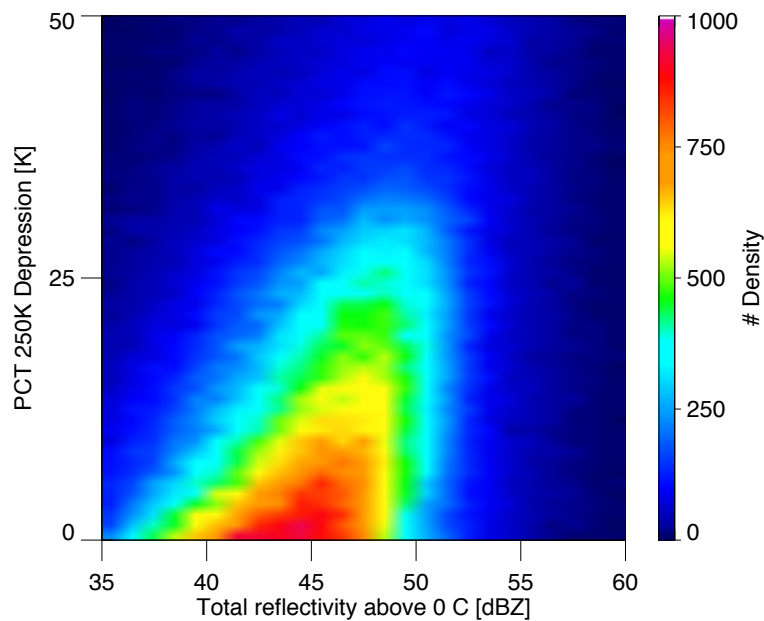
Figure 3.5 Relationship between the total reflectivity above the freezing level (PR) and 85 GHz Tb PCT 250 K depression (TMI).

Clearly, Eq. (3.1) and Eq. (3.2) show that PMW rainfall depends on the 85 GHz temperature depression, which in Fig. 3.5 is seen to be proportional to the reflectivity observed above the freezing level (i.e., to the reflectivity related to frozen hydrometeors). At the same time Fig. 3.3 suggests that the amplitude in the signal related to the presence of the

ice in clouds, typical for Amazon and African regions, differs. This is consistent with the hypothesis that the ice aloft is indeed related to the variability in the PR-to-PMW rainfall difference over these two regions.

3.4. Addressing the variability of the ice aloft to rain rate relation

The most striking property in Fig. 3.4 is a large pixel-to-pixel variability in the relationship between the total reflectivity above the freezing level and the surface rainfall. For moderate to high rain rates, the reflectivity can vary more than 15 dBZ (e.g., at 10 mm h^{-1} TRFL ranges from 45 dBZ to 58 dBZ). It is well known that clouds undergo substantial microphysical and thermo-dynamical changes through their lifecycle (e.g., chapter 14 in Stull 2015; Cotton et al 2011). The ice-phase responds to these changes (Imaoka and Nakamura 2012). Therefore, the pixel-level variability in Fig. 3.4 is expected, as different lifecycle stages are captured by TRMM's random sampling. The goal of this study, however, is not to interpret this pixel-level variability. Instead, the focus is on understanding the separation of the two mean relations in Fig. 3.4. Considering the sample size (over 50,000 pixels) the variability of the relationship between the mean total reflectivity above the freezing level and the surface rainfall over the two regions is significant.

3.4.1 Stratiform/Convective classification

The PR standard product 2A23 separates raining pixels into a number of categories, the majority of which (95%) fall into stratiform and convective classes. Categorization is made based on criteria such as: presence of a brightband, precipitation depth, reflectivity value, and type of neighboring pixels (Awaka et al. 2009). The outcome is shown to be in good agreement with similar schemes applied to ground-based classifications. Thus, this pixel

categorization is expected to efficiently recognize contrasts in vertical structures of stratiform and convective cloud types. Because of their different ice structures, systematic differences of these cloud types may be able to explain the observed regional differences in Fig. 3.4.

The PR reflectivity profiles of stratiform and convective pixels over the Central African and Amazon regions are compared in Fig. 3.6. As expected, the two classes separate well. However, using the freezing level height (4-5 km according to the brightband) as a reference, it is easy to notice that the reflectivity above 0 °C is significantly larger over the African than the Amazon region for both convective as well as stratiform cloud structures. This result thus adds little to our existing result from Fig. 3.4 that Africa has systematically higher reflectivities in the ice region than South America.
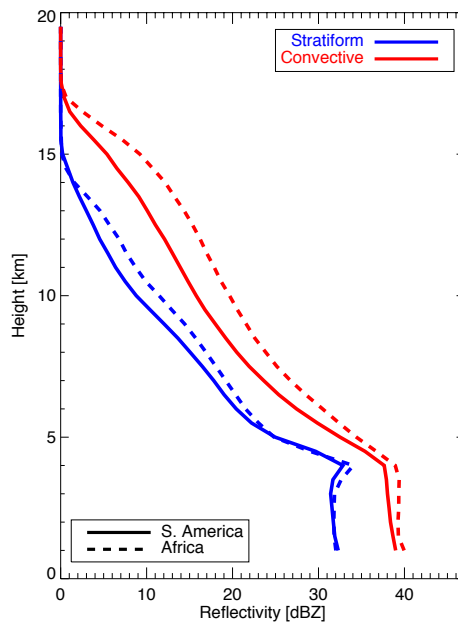
Figure 3.6 Mean PR reflectivity profiles over 4 mm h^{-1} 0.5° grid boxes within the two regions marked in Fig. 3.1. Both convective (red) and stratiform (blue) pixels tend to have stronger reflectivity over Africa compared to Amazon.

3.4.2 Cloud cluster type classification

An alternative classification of clouds consists of the clustering method developed in a study by Elsaesser et al. (2010, 2013). Elsaesser et al. (2010) classify precipitation regimes based on a cloud type probability density functions (PDFs), following the notion that regimes are characterized by distinct combinations of shallow, mid-level and deep convective cloud types (as discussed in Johnson et al. 1999). Using their approach, we tested self-similar PDFs of cloud characteristics allowing them to group into three clusters. In the original study, tropical oceanic clouds are clustered into classes defined by: 1) Shallow, 2) Deep-organized, and 3) Deep-unorganized convection. To mimic this, we first define a regular 1° x 1° grid along the TRMM track, and then seek cluster centroids, or "regimes", that minimize the Euclidean distance in an x-dimensional space of standardized variables. The variables, following Elsaesser et al. (2010), are chosen to be: 1) echo top heights (ETHs), 2) convective to stratiform rainfall ratio, and 3) raining to non-raining pixel ratios, all given by PR over the 1° grids. The first are given by the altitude of the highest non-isolated range bins with reflectivity of at least 17 dBZ (more details in Short and Nakamura 2000) with shallow systems being dominated by clouds with ETHs less than 5 km, deep-organized systems with ETHs from 5 to 9 km, and deep-organized ones with ETHs greater than 9 km. The other two variables are simply based on the total number of pixels within each category. While the echo top heights represent a proxy for the amount of ice in the cloud column, they also relate relatively well to the level of cloud system organization (e.g., deeper clouds yield more organization, as seen in Johnson et al. 1999). Application of the clustering algorithm results in the same cloud regimes described by Elsaesser et al. (2010, 2013). The corresponding

change of reflectivity with height and Tb values at 85 GHz of each regime are shown in Fig. 3.7.
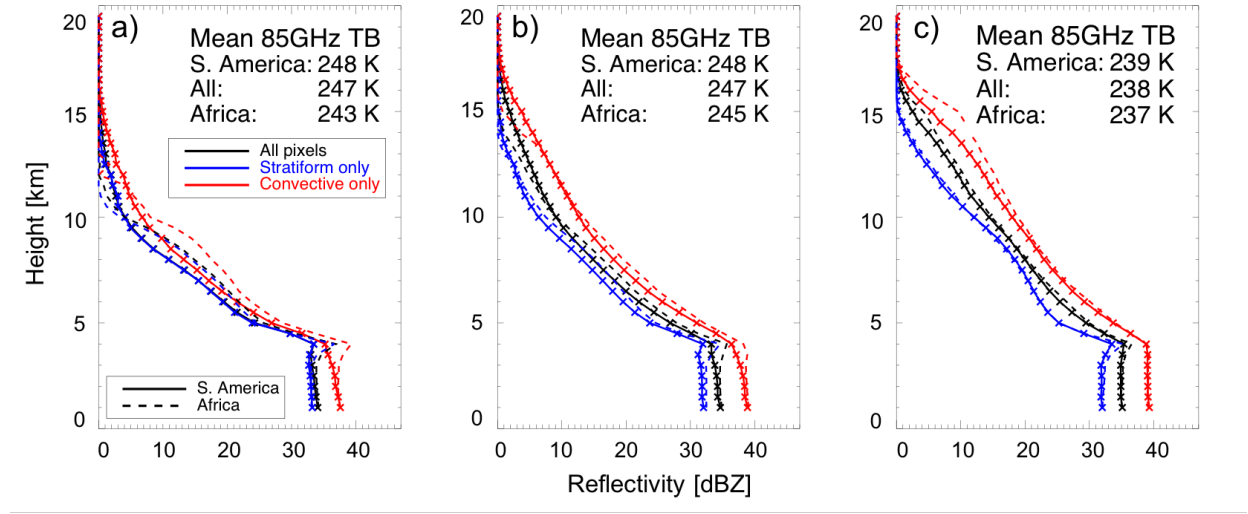
Figure 3.7 Vertical PR reflectivity profiles separated by 1) precipitation regime: shallow (a), deep-unorganized (b), and deep-organized (c); 2) precipitation type: convective (red) and stratiform (bleu) and; 3) region: Amazon (solid lines) and African (dashed lines).

Profile comparison suggests that unlike convective/stratiform profiles, regime vertical structures are extremely consistent between Africa and South America. For example, if one choses a vertical profile (convective or stratiform) in Fig. 3.7 to compare its extend and shape over the Amazon and African regions, it will find very little variability between the two regardless of chosen regime. Regional differences must therefore be related more to a change in regime frequency than in regime properties. High frequency (i.e., 85 GHz) Tbs further show significantly lower values in the case of deep-organized cloud systems, implying enhanced ice content of this regime. This is consistent with higher reflectivities detected throughout the column of dBZ profile above the freezing level (i.e. bright band) in deep-organized systems (panel c) compared to shallow ones (panel a). These results are

generally consistent with clouds and cloud system properties described in the existing literature (e.g. Steiner et al. 1995, Houze et al. 1990).

3.4.3 Explaining the variability of scattering-signal-to-rain-rate relationship using cloud clusters

Consistency of the regimes with respect to ice aloft and Tb depressions between the two regions suggests that using the clustering approach has more potential in addressing the systematic discrepancies over the two regions than the simple stratiform-convective classification. Figure 3.8 shows the probability of occurrence of each regime along with the total rain fraction of that regime. Additionally, Fig. 3.9 shows the relative difference in total rainfall contribution separated by regime as well as the corresponding scatterplots showing the differences within each regime. The results suggest a strong correlation between the three cloud system types and rainfall differences seen in Fig. 3.1. While no obvious correlation is noticeable between the systematic differences and deep-unorganized regime (middle panels), PMW negative deviations (purple areas in Fig. 3.1) coincide well with the Relative Frequency of Occurrence (RFO) of the shallow systems (top row in Fig. 3.8) and PMW positive deviations (warm colors in Fig. 3.1) coincide with RFOs of deep-organized systems (bottom row in Fig. 3.8). The results are in agreement with the findings that use similar approach to describe tropical convection [e.g., Mohr *et al.* (1999); Zipser et al. (2006); Wall et a. (2013); Houze et al. (2015)]. For example, Mohr *et al.* (1999) found that well-organized storms, MCSs, in the African region constituted 10%–20% of the regional populations of convective systems but contributed 70%–80% of the rainfall. Zipser et al. (2006) show the distribution of intense thunderstorms that coincide well with the relative frequency of occurrence of deep-organized systems in Fig. 3.8. The same study found that

rains over the Amazon have relatively few intense storms, which relates to properties of the

shallow systems seen here.
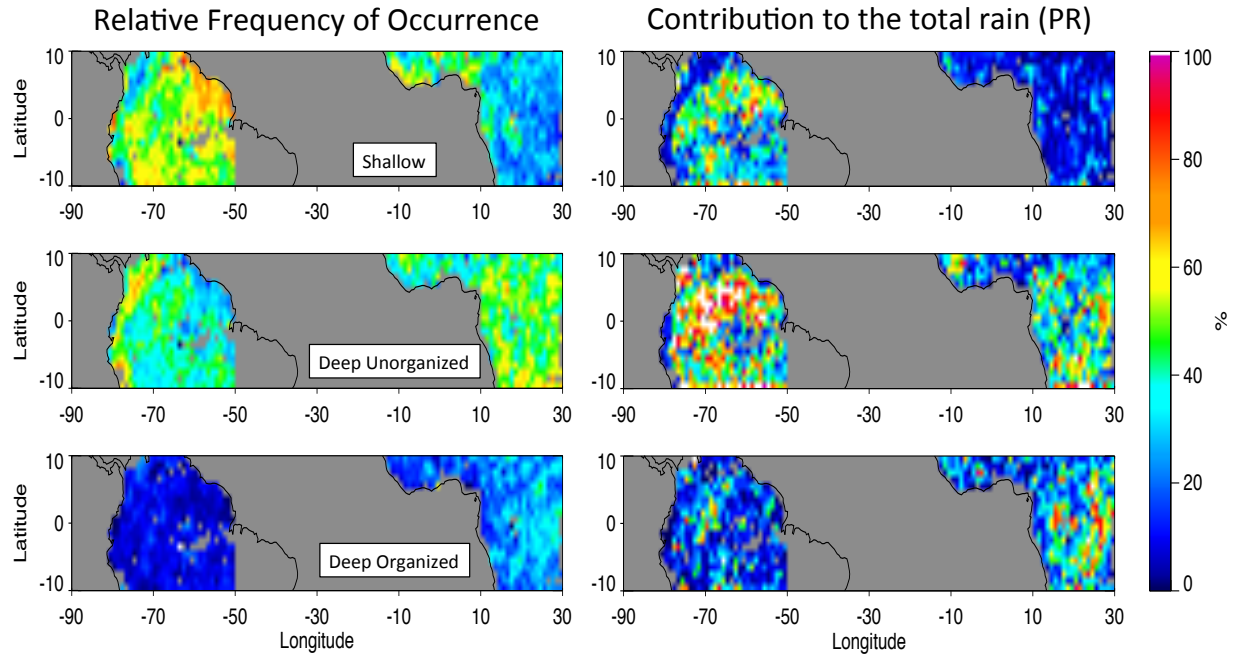
Figure 3.8 Relative frequency of occurrence (left) and contribution to the total PR rain (right) by: shallow (top), deep-unorganized (middle) and deep-organized (bottom) precipitation regimes over the Amazon and African regions in 2010.
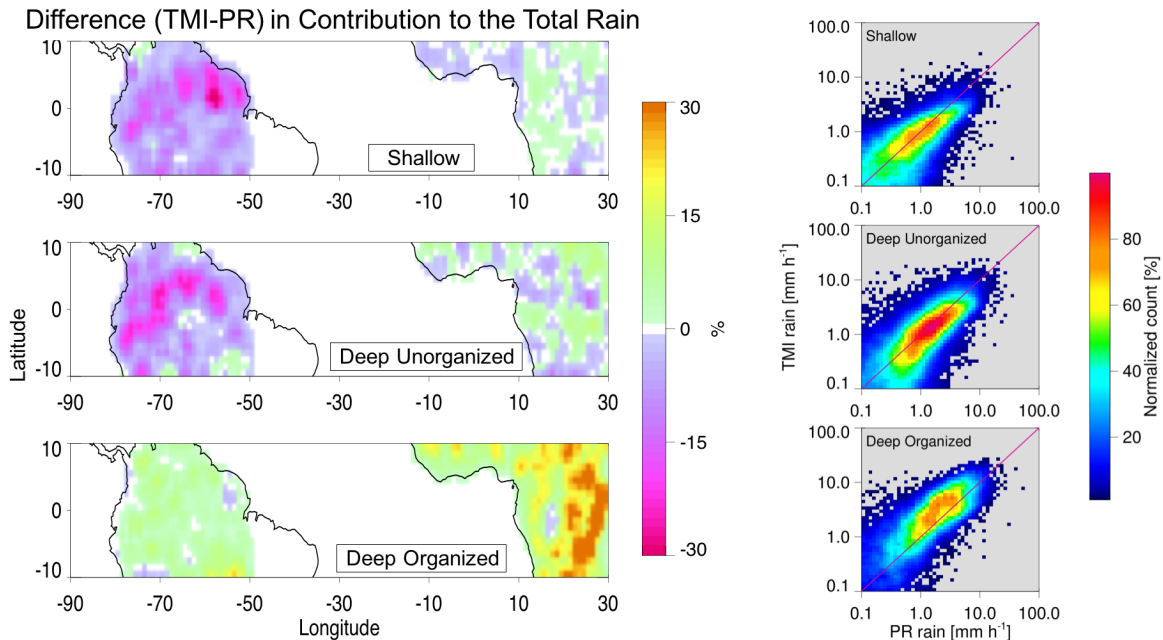
Figure 3.9 Left: The relative difference between PR and PMW total rainfall contribution separated by precipitation regime. Right: Density scatter plots of the PMW and PR rainfall estimates (log-axes) for each of the regimes. In shallow regime (top) PMW sensor underestimates PR by 33%; in deep-unorganized regime (middle) PMW underestimates PR by 10%; in deep-organized regime (bottom) PMW overestimates PR by 41%.

By showing the relative difference between PMW and PR total rainfall estimate with corresponding rain rate plots, Fig. 3.9 quantifies the contributions to the total systematic difference by each of the three regimes. Shallow and deep-unorganized regimes tend to be underestimated by the PMW sensor compared to the PR (by 33 % and 10 %, respectively), while the deep-organized regime rainfall is overestimated (by 41 %). Most of the areas with positive differences in the top two panels of Fig. 3.9 correspond to regions where shallow and deep-unorganized regimes contribute less than 50% to the total rain. Combined information from Figs. 3.8 and 3.9 suggests that cloud systems RFO explains up to 50% of the systematic differences over the Amazon and African regions. The overall conclusion is that PMW sensor indeed tends to overestimate ice-rich deep-organized convection and

underestimate the other two, relative to the PR. This, coupled the changes in the relative frequencies of occurrences of these systems, generally explains the systematic difference seen in Fig. 3.1.

The above conclusion is supported by Fig. 3.10, which uses the integrated reflectivity above the freezing level versus surface rainfall, as done for Fig. 3.4, to repeat the analysis. The figure clearly shows that deep-organized systems relate to positive, while shallow systems relate to negative deviations from the mean PR's ice-column-estimate-to-rain ratio of Fig. 3.4. This suggests that if one has knowledge on a type of a cloud system, then PMW-to-PR deviation of that system may be predicted, at least in the mean sense. Unfortunately, PR measurements are not always available to provide this information to PMW algorithms. Therefore, an alternative approach to link the observed storms to the systematic differences is desirable. Based on the current understanding of the interactions of storms with the environment, a potential solution exists if the environment can be used to predict cloud organization level (i.e., raining regime).
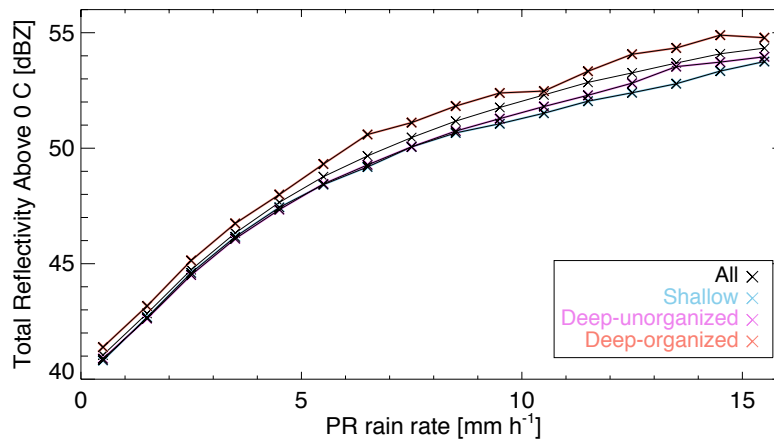
Figure 3.10 Same as Fig. 3.4 just separated by the system type (shallow, deep-unorganized, deep-organized).

3.5. Cloud System Types and the Large-scale Environment.

Clusters form a convenient basis for understanding the relationship between systematic differences and the synoptic state of the atmosphere (hereinafter also referred to as the "large-scale environment"). Shaped and governed by thermo-dynamical and microphysical processes, precipitation systems change and evolve during their lifecycle. By grouping the storms into structurally self-similar systems, clusters form subsets of data that potentially have less pixel-to-pixel variability induced by these lifecycle changes. Sampling the atmospheric conditions by criteria that are well known to play a key role in cloud development reveals links between the environment and the level of cloud system organization. Using findings from Mohr *et al.* (1996; 1999), Petersen et at. (2002), and other above-mentioned studies, a relationship between the regimes and large-scale parameters is tested.

Atmospheric parameters are taken from ERA-Interim and co-located with the existing 1° x 1° raining scenes. To ensure that environmental variables are not affected by

precipitation thermodynamics, the ERA-Interim data preceding the time of PR precipitation are used. Thus, the time-gap between the environment state and rainfall observations can be as large as 6 hours (temporal resolution of the 3D Era-Interim). A number of parameters and their combinations (e.g., convective available potential energy – CAPE, total column water vapor – TPW, skin temperature, vertical and horizontal winds at 700 mb, velocity of the mid-level jet, the magnitude of the low-level wind shear, the surface equivalent potential temperature) are tested as cloud regime predictors. Several parameters stand out: the mid-level vertical wind shear, vertical humidity deviation, CAPE, and the low-level dew point depression. Results are presented in Fig. 3.11 and Table 3.1.
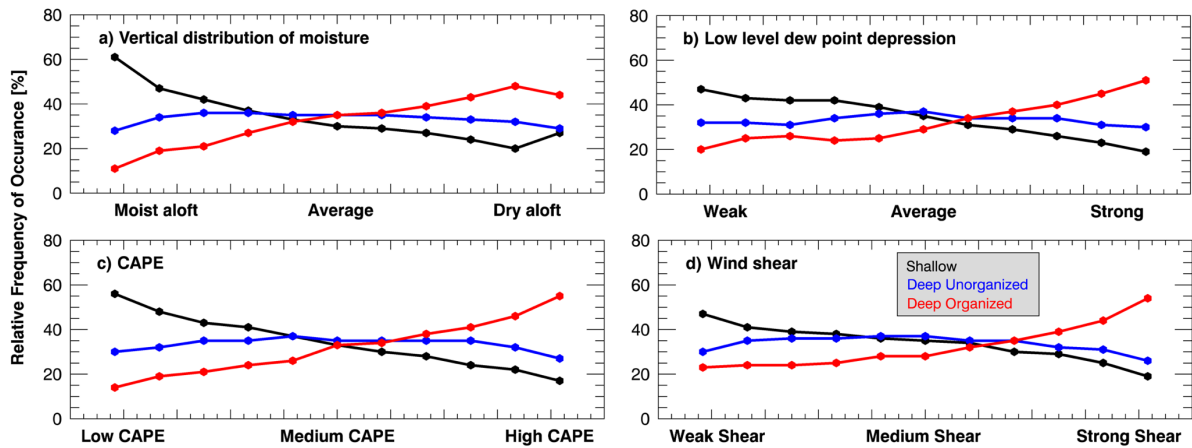
Figure 3.11 Relative frequency of occurrence (RFO) of deep intense organized (*red*), shallow (*black*), and deep-unorganized (*blue*) systems as a function of the environment. For the exact values of RFOs and the environments see Table 3.1.

Table 3.1 Environment bin limits with the corresponding PR to PMW (TMI) rainfall estimate ratios and Relative Frequency of Occurrence (RFO) of the three regimes, for the year 2010. Note: the bin limits for the vertical humidity deviation are given in the reversed order of what they appear in the panel a) of Fig. 3.11 (i.e. lower bin limit values correspond to the dry-aloft conditions).

CAPE

Bin limits [J kg⁻¹]	124	256	384	511	645	792	954	1137	1369	1729	+ ∞
PR/PMW ratio	1.50	1.25	1.18	1.16	1.13	1.01	1.03	0.95	0.89	0.88	0.78
RFO Shallow [%]	56	48	43	41	37	33	30	28	24	22	17
RFO Deep-	30	32	35	35	37	35	35	35	35	32	27
RFO Deep-Organized	14	19	21	24	26	33	34	38	41	46	55

VERTICAL HUMIDITY DEVIATION

Bin limits	0.11	0.14	0.16	0.18	0.20	0.21	0.23	0.24	0.26	0.29	+ ∞
PR/PMW ratio	0.77	0.83	0.87	0.95	0.98	1.02	1.04	1.12	1.18	1.23	1.28
RFO Shallow [%]	27	20	24	27	29	30	33	37	42	47	61
RFO Deep-	29	32	33	34	35	35	35	36	36	34	28
RFO Deep-Organized	44	48	43	39	36	35	32	27	21	19	11

LOW-LEVEL DEW POINT DEPRESSION

Bin limits [K]	0.48	0.88	1.26	1.69	2.24	2.99	4.11	5.63	8.24	12.64	+ ∞
PR/PMW ratio	1.27	1.20	1.16	1.18	1.14	1.07	0.99	0.91	0.85	0.73	0.65
RFO Shallow [%]	47	43	42	42	39	35	31	29	26	23	19
RFO Deep-	32	32	31	34	36	37	34	34	34	31	30
RFO Deep-Organized	20	25	26	24	25	29	34	37	40	45	51

WIND SHEAR

Bin limits [m s⁻¹]	-2.14	-1.02	-0.24	0.43	1.06	1.71	2.39	3.15	4.15	5.68	+ ∞
PR/PMW ratio	1.22	1.09	1.09	1.06	1.05	1.06	1.09	1.00	0.96	0.87	0.76
RFO Shallow [%]	47	41	39	38	36	35	34	30	29	25	19
RFO Deep-	30	35	36	36	37	37	35	35	32	31	26
RFO Deep-Organized	23	24	24	25	28	28	32	35	39	44	54

The analyses show that high CAPE values, strong shear and dry-aloft conditions are favorable precursors of deep-organized convection. In these environments intense well-organized systems are 2 to 3 times more common than any others. Conversely, low CAPE, week shear and moist-aloft setup are conditions that favor the shallow regime. While the two more-organized regimes (shallow and deep-organized) are highly predictable, it is interesting to note that deep-unorganized systems show no, or very little, sensitivity to any

of the tested variables. This may not be too detrimental since this is also the regime that showed the least disagreement in rain estimates between the two sensors. The role of the environment parameters favoring specific cloud regimes is examined next.

3.5.1 Wind shear and Convective Available Potential Energy

A role of CAPE and wind shear in cloud development is often coupled and as such broadly discussed in the literature. As a measure of atmospheric column potential energy, CAPE is widely used to predict convection intensity and longevity. Whether only a part or most of the column energy is exploited in the cloud development process depends on a number of factors where wind shear plays an important role (e.g., Xu 1992; Xu and Moncrieff 1994). Studies and theoretical models of cloud system organization describe a necessary balance between the strength of the updrafts and their vertical tilts to allow for deep-organized features such as MCSs. By defining a displacement of down-welling motions relative to the updrafts, wind shear controls the ability of precipitating system to utilize environment resources (e.g., CAPE). While downward motion of the hydrometeors straight through the updraft limits the storm's potential to propagate and feed on the unperturbed unstable environment, too much wind shear may force the rainwater into dryer layers away of the storm's core and cause evaporation that can stabilize the atmospheric column too fast (e.g., Rotunno et al. 1988; LeMone et al. 1998). Whether cold pool, updraft intensity, front and rear inflows, or in-cloud thermo-dynamical processes, are more favorable for one cloud regime over another, is a complex question that cannot be simply answered by CAPE and wind shear alone. However, these two variables have a strong influence on all of these factors and therefore serve as good predictors of a storm's organization level.

3.5.2 Low-level dew point depression

Using a low-level dew point depression as a cloud system type predictor is motivated by the facts that this quantity simultaneously provides information on the low-level relative humidity and state of the soil moisture, both of which have been shown (e.g., Ford et al. 2015) to relate to the cloud system initiation and development. Near the surface relative humidity is a relatively good proxy for the state of the boundary layer. Soil moisture and 2 m temperature are also related to the height of the boundary layer, which plays an important role in defining the cloud base height. This further influences the depth of the cloud determining thermo-dynamical properties over the course of the cloud lifecycle. At the same time the relative humidity and cloud base height strongly affect the amount of rainwater evaporated before reaching the ground. This does not only alter the rain rate but also may play an important role in further development and organization of the cloud system through the downdraft bursts and cold pools. Findings of Ek and Mahrt (1994) offer an example of the complex response of cloud properties to the top of a boundary layer. They found that drier soil leads not only to lower boundary-layer specific humidity but to cooler temperatures at the boundary-layer top due to greater-boundary layer growth. When the latter effect dominates, the relative humidity at the boundary-layer top is greater over drier soil. In contrast, they saw drier soil leading to lower relative humidity at the boundary-layer top when the air above is strongly stratified or very dry.

Clearly, large-scale environments can serve as predictors of a cloud system type. If relationships between the environment, system types, and PMW systematic differences are consistent and robust, then the environment itself must have a well-defined relationship to these differences as well.

3.6. Potentials of removing PMW climatological errors

The results, to this point, demonstrate that systematic deviations of PMW rainfall retrieval relative to PR rain estimates over land are caused by regionally dependent differences of the ratio between the ice scattering signature and surface rainfall, characterized by strong pixel-level variability. While this localized variability is hard to capture, grouping the pixels into classes (clusters) of distinct mean PMW-to-PR deviations allowed for their difference reduction at larger scales.

It was shown that clusters relate well with PMW to PR rainfall ratio and that the large-scale environment is a reasonably good predictor of the cluster types. Therefore, it is expected that both can perform well if used to predict their disagreement. To demonstrate these predictors' potential in reducing PMW-to-PR differences, a simple experiment is performed. A year of TRMM data is used to quantify the relationship between rain estimate of the two sensors (e.g., that seen in Fig. 3.1), with respect to: a) environment, and b) clusters. For each given environment or cluster, the PMW-to-PR rainfall ratio is recorded. Once available, this ratio is used to adjust the retrieved PMW rain rate estimates of an independent time interval when similar environmental or cluster conditions exist. The results are presented below.

3.6.1 Large-scale Environment as a variability-predictor

Before any PMW rainfall adjustments are made, Fig. 3.12 presents the mean PMW-to-PR ratios as a function of the environment categories used in Fig. 3.11. Clearly, a robust relationship exists, supporting the original hypothesis that the large-scale environment relates to differences between PMW and PR rainfall estimates. Table 3.2 lists correlations between the environments, suggesting that none of the four is overly linked to the others.
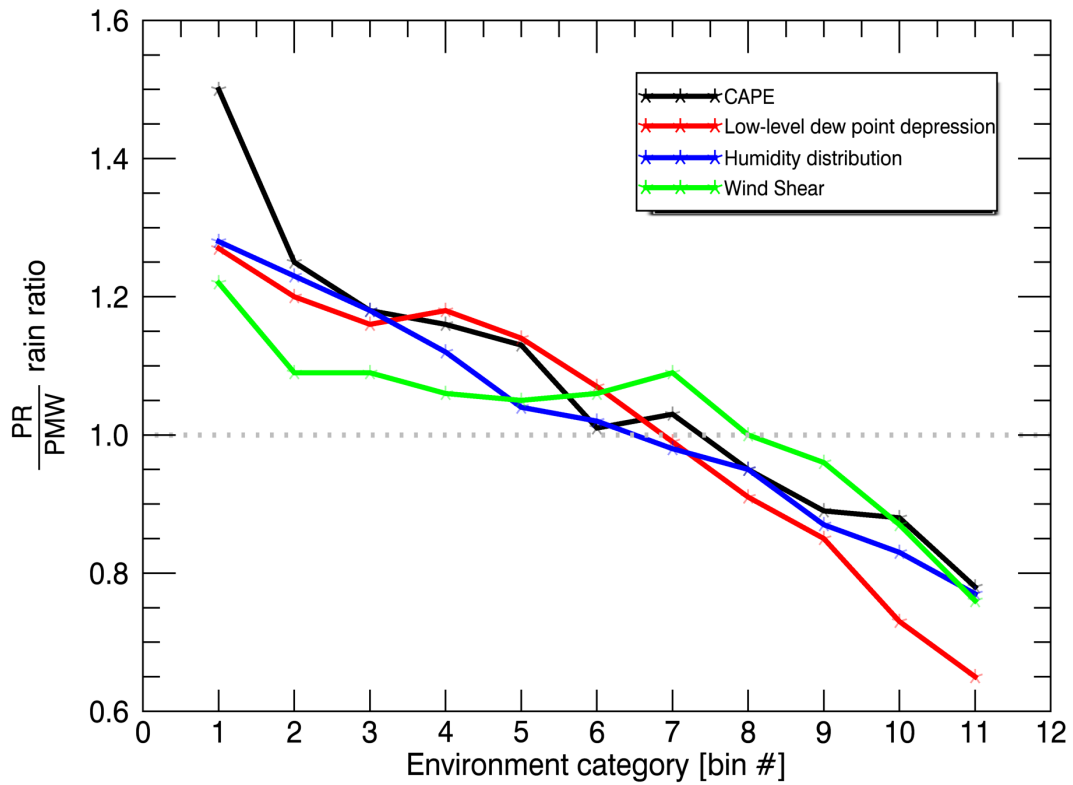
Figure 3.12 PR to PMW rainfall ratio as a function of large-scale environment during the year of 2010. The environmental bins are the same as in Fig. 3.11. The bin limits and exact values of PR to PMW rainfall ratios are listed in Table 3.1.

Table 3.2 Correlation between the large-scale environments of the four categories seen in Fig. 3.12. Data source: ERA-Interim reanalysis data for 2010.

	Humidity deviation	Dew point depression	CAPE	Wind Shear
Humidity deviation		-0.18	-0.15	-0.22
Dew point dep.	-0.18		-0.10	0.15
CAPE	-0.15	-0.10		0.10
Wind Shear	-0.22	0.15	0.10	

Multiple environment predictors of the PMW-to-PR rainfall ratio are also tested at once.

Figure 3.13 depicts an example where CAPE-defined environment is sampled by low-level

dew point depression. As the dew point depression decreases, an increase in the ratio of the

two instruments' rainfall is seen across each of the CAPE environment bins. Similar results

are seen for any combination of the environments (not shown here).
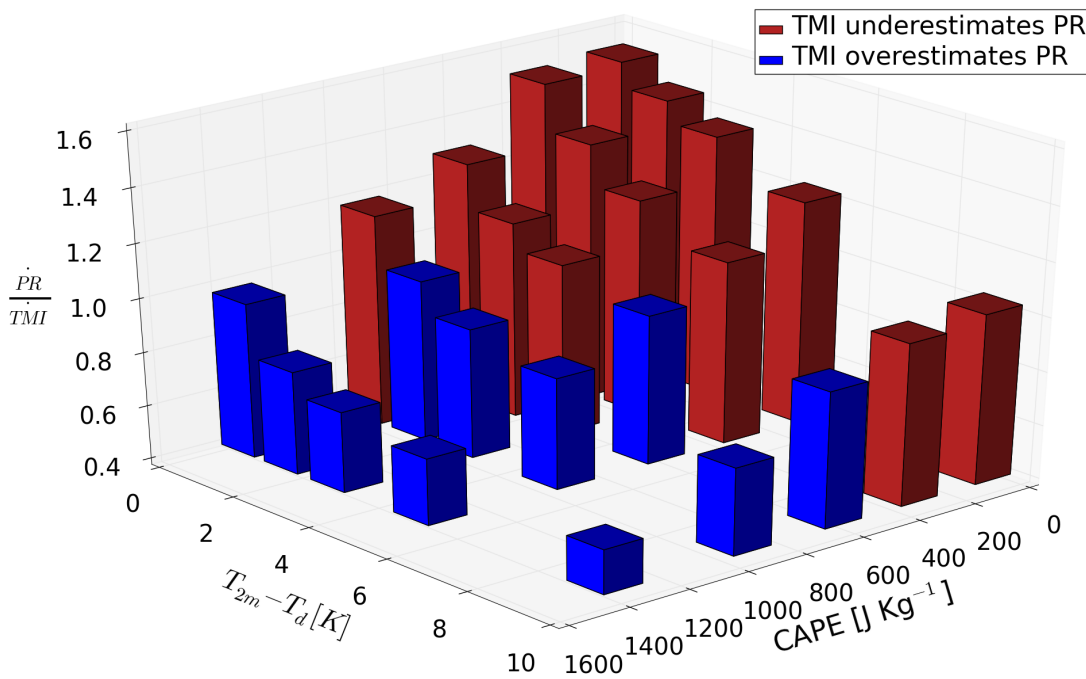
Figure 3.13 Ratio between PR and PMW rainfall as a function of the environment defined by CAPE and the difference between 2m temperature and dew point. Red bars denote bins where PR rainfall is underestimated by PMW retrieval, while blue bars denote the opposite.

Finally, to quantify the predictability of the two sensor's disagreements, Fig. 3.14 compares the original (black) and adjusted (red) PMW estimates of mean daily rain rates to those of PR, for year 2008, using level-3 products at 10° resolution. The adjustments of PMW rain estimate are based on the 2010 dataset constraining the PMW-to-PR ratio by two environments at a time. Using the observed CAPE and wind shear as criteria (left panel), improvements of approximately 30 % and 35 % are made in RMSE and systematic difference of daily rain rates, respectively, while regression coefficient is improved by 25%. Improvements are somewhat less appealing, but still significant when CAPE is used in combination with the humidity distribution, removing approximately 20% of the relative bias. When individual grids are compared, with no exceptions, improvement is found across the entire domain (not shown here).
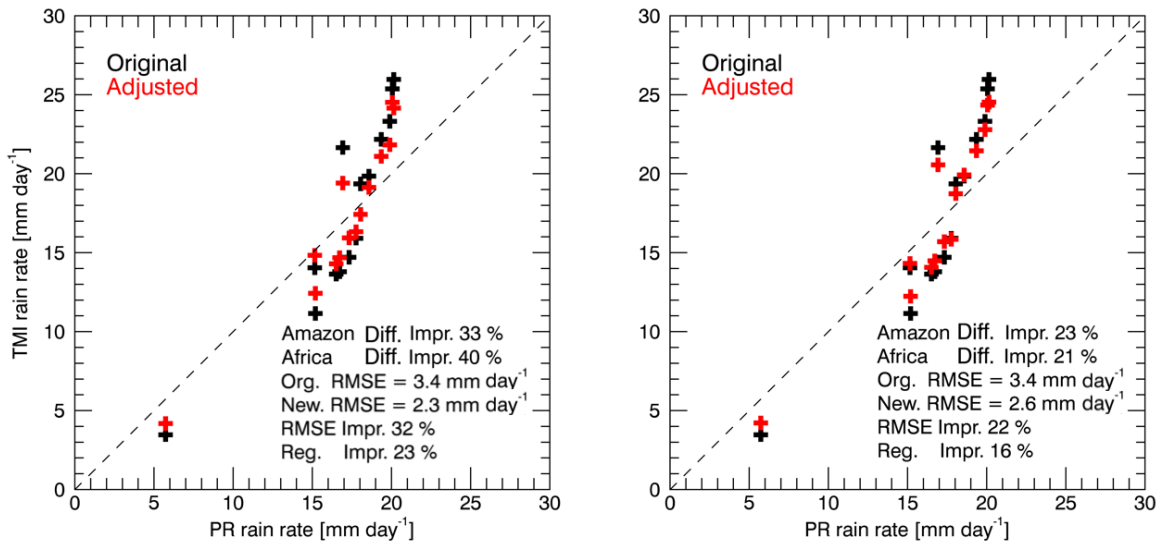
Figure 3.14 The PMW to PR conditional rainfall comparison before (black) and after (red) PMW rainfall estimate adjustment. Scenes observed by both sensors as non-raining are excluded. A combination of CAPE and shear values (left panel), CAPE and humidity distribution (right panel) is used to predict and then reduce the PR to PMW retrieval difference in GPROF algorithm at 10° x 10° grid for the regions marked in Fig. 3.1.

3.6.2 Cloud system type as a variability-predictor

Section 3.4c and Fig. 3.9 depict the PMW-to-PR rain ratio as a function of a cloud system type. The performance of the cloud system type in PMW systematic difference removal is evaluated in Fig. 3.15 by repeating the same test as above. The RMSE of adjusted rain rates yield value of 1.9 mm day^{-1} corresponding to proximately 40% of improvement relative to the original value of 3.4 mm day^{-1}. At same time systematic differences over the two regions are reduced by almost 50%. Clearly, a significant reduction of both RMSE and bias confirms a strong relation between the bias-to-cloud-structure to PMW systematic differences in rainfall estimates over land.
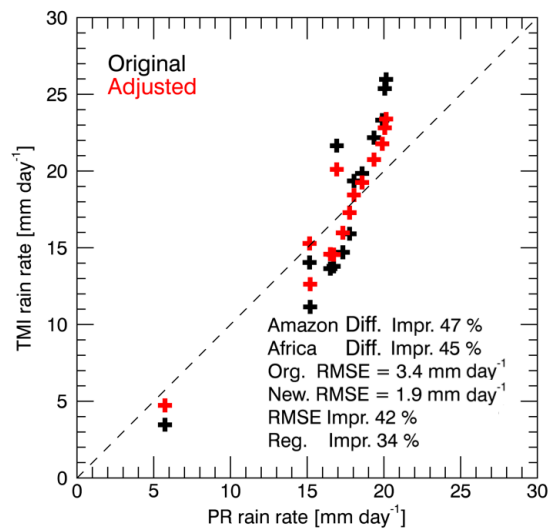
Figure 3.15 Same as Fig. 3.14 but now using the cloud system type as a predictor of the PMW to PR retrieval deviation.

When comparing the two predictors, cloud system types explain more variability between the two sensors. However, their definition was based on radar characteristics and thus may not be easily applied to radiometer-only retrievals.

3.7. Summary

This paper tries to provide a better understanding of systematic differences seen in PMW rainfall retrievals over land. The study explores the links between ice scattering PMW signature and estimate of surface rain intensity, cloud system structure, and large-scale environments. It is shown that observed cloud physics and relationship between Tb depression and surface rain intensity correlate well with regional PMW-to-PR rainfall discrepancies in tropical Africa and South America. Variability of ice-scattering-signal-to-rain-rate relationship across these two opposing regions is captured by grouping the pixel-level data into three self-similar cloud classes of distinct levels of organization. Although these groups showed great potential in removing systematic differences seen between PMW and PR rainfall estimates, their diagnosis is too complex for PMW retrieval applications. As a natural driver of atmospheric processes, the role of a large-scale environment in defining these distinct levels of cloud organization is evaluated. When constrained by CAPE, wind shear, dew point depression, and vertical humidity distribution, the environment is found to be in favor to a certain storm types. Thus, high CAPE values, as well as dry aloft conditions are most commonly seen prior to deep-organized systems. On the other side, low wind shear and weak dew point depression are both in favor of shallower unorganized events. The ability of large-scale environments to reduce climate-scale PMW to PR rainfall differences is found appealing, lowering the current PMW-to-PR regional rainfall ratios by up to 40%.

The possibility is left open that other predictors, or combination of predictors, could be used to further improve upon these results, overcoming the lack of information content that observed vector currently offers to PMW retrievals over land. It is concluded that addressing

the role of the cloud structure variability in PWM observations will be an inevitable step in future versions of the PMW algorithms.

CHAPTER 4

IMPROVING THE QUALITY OF EXTREME PRECIPITATION ESTIMATES FROM SATELLITE

PASSIVE MICROWAVE RAINFALL RETRIEVALS

4.1 Introduction

Rather than uniform and continuous, transitions of a physical system from one state to another state are often seen as a series of random perturbations characterized by a general trend. The capability to recognize this trend is a key for early detection but is often limited by access to accurate measurements. In an effort to adapt to an ever-changing climate, understanding fluctuations of atmospheric phenomena, especially their extremes, has a critical role. Emerging from complex thermo-dynamical processes, changes in precipitation could be thought of as a reflation of transitions of the changing physical system. Diagnosing the onset of a change in such a complex system is usually done by examining changes in its extremes. Therefore, direct observations of extreme precipitation at global scales are invaluable in understanding the ever-changing climate. Despite a long, albeit sparse, record [first known observations date back 2000 BCE (Wang and Zhang, 1988)], globally complete precipitation measurements did not become available until the modern era of satellite earth-observing systems that employ infra-red and microwave radiometric techniques (e.g., Atlas and Thiele, 1981). Achieving measurement standards of rainfall in atypical (i.e. extreme) environments on small spatio-temporal scales across the globe, however, has turned out to be more difficult than anticipated. Although satellite observations can have relatively large

random errors at small scales, their global nature makes them suitable for addressing potential changes in global precipitation extremes.

The first satellite-born passive microwave (PMW) instruments date back to mid 1960s. Rainfall detection from space began with the Scanning Multi-Channel Microwave Radiometer launched onboard the Nimbus-7 satellite in the mid 1970s making satellite PMW measurements an indispensable part of global rainfall records until the present day. Although far from ideal, the relatively low cost of microwave imagers made them affordable and a popular choice of instrument for many past and upcoming space missions (NIMBUS, DMSP, NOAA, METOP, TRMM, GPM, JPSS, to name a few). At the same time, passive microwave rainfall retrievals became, either directly or indirectly, one of the most important components of gridded products [e.g., IMERGE (Huffman et al. 2015), CMORPH (Joyce et al. 2004), TMPA (Huffman et al. 2007), PERSIANN-CCS (Hong et al. 2004), GSMaP (Kubota et al. 2007; Ushio et al. 2009)] that are commonly used in applications requiring precipitation at high spatial and temporal resolutions.

Continuous work on finding physical relations between the observed (i.e., brightness temperatures (Tb)) and state (i.e., rainfall) vectors, led to PMW retrievals improvements from fairly simple regression models (e.g., Grodi 1976, Wilheit et al. 1976) to sophisticated algorithms that employ radiative transfer and cloud resolving models, optimal estimation methods, and principal component analysis (e.g., Petty and Li 2013). Limitations, however, still exist (e.g., Petkovic and Kummerow, 2017), especially over land. Specifically, high and variable land surface emissivity obstructs the information content provided by PMW instruments, limiting rainfall signals to an indirect, non-unique, relationship between cloud ice-scattering signatures and surface rainfall. Based on the mean observed ratio between ice

aloft and the surface rainfall, these estimates can often be inaccurate, with more pronounced biases observed during the extreme events. In addition to the example given in Chapter 2, a difference in mean rain rate estimate bias between ground radar measurements and an operational satellite PMW retrieval is shown in Fig. 4.1. The top 10% of rain rates for the period between Sep 2014 to Aug 2015 (for detailed description of the data sources and domain see Section 4.4) are compared on a 0.25° grid over the Eastern US, ensuring high quality data and a good understanding of related system features. Clearly, satellite estimates show negative bias over the entire region. In addition, Fig. 4.2 compares satellite Field Of Views (FOVs) to corresponding ground reference (pixel-to-pixel comparison). It reveals a negative (underestimation) bias of 28% for the PMW retrieval for the top 10% of rain events as defined by the ground based radars. Characterized by relatively high correlation coefficient (0.66) the retrieval's performance is consistent in its negative bias at all rain rate values (black crosses mark mean retrieved rain rates for each of ground reference rain rate bins). This is the result of an assumed relationship between the cloud property (i.e., ice-content) and rain rate, used to retrieve the rain, that was derived from a broad range of observations but used only on a narrow portion of the rainfall spectrum (i.e. extreme precipitation regime).
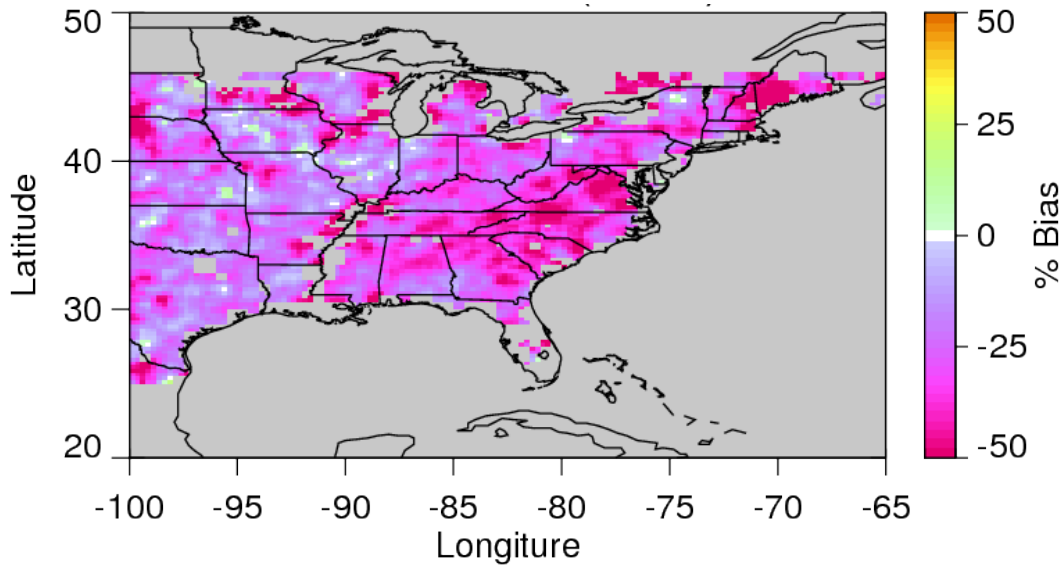
Figure 4.1 Mean rainfall bias between a ground reference (MRMS) and PMW retrieval (GPROF) for the top 10% of rainfall rates over eastern CONUS for period Sep 2014 – Aug 2015 on 0.25° grid. The mean MRMS observed rainfall rate for the period is 3.98 mm h⁻¹ while the mean PMW retrieved rainfall rate is 2.87 mm h⁻¹. The overall bias is -28% (Negative values in the map indicate satellite's retrieval underestimation of the ground reference.).
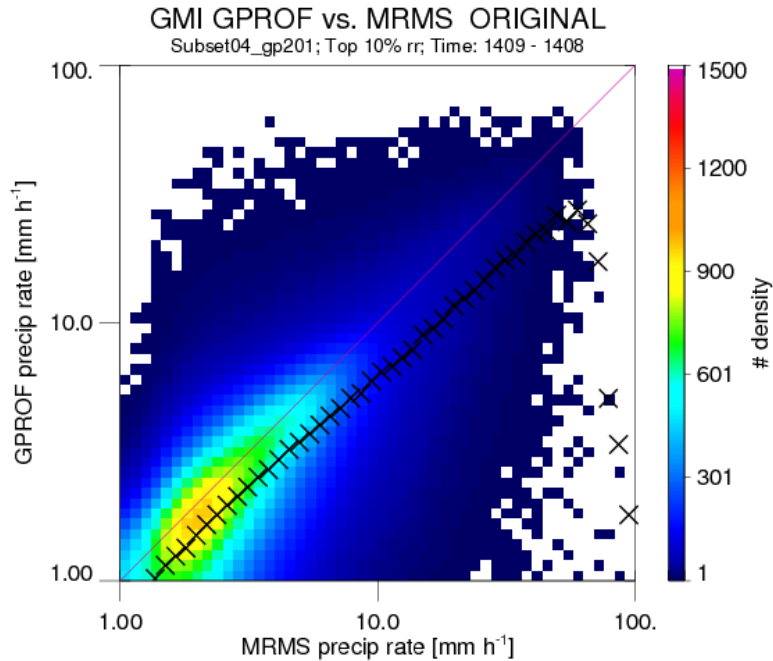
Figure 4.2 Pixel-level comparison of PMW rainfall retrieval (GPROF) and ground reference (MRMS) for the top 10% of rainfall rates over eastern CONUS for period Sep 2014 – Aug 2015. Black crosses represent mean PMW rainfall rate value for corresponding reference rainfall rate bin. The overall bias value for these maximum rain rates is -28%. The correlation coefficient is 0.66.

Fixing this problem requires a better understanding of the ice content in extreme precipitation events. Rather than trying to improve the retrieval itself, a solution is seen in complementing the observed brightness temperature vector with information that would help mitigate ambiguities in ice-to-rain relationship. In an attempt to do so, this study seeks to utilize more-complex links between observed cloud properties and common atmospheric parameters (e.g., large-scale environment). Based on findings presented in Petkovic and Kummerow (2017), it is hypothesized that such information is correlated with the synoptic state of the atmosphere. Additional variables can mitigate the information gap between the assumed and observed cloud property. To better understand challenges inherent in such a

scheme, a general review of the Bayesian approach, the approach used by the PMW retrieval validated in Figs. 4.1 and 4.2, is provided next.

4.2. Understanding the sources of rainfall bias - theoretical background

Developed by Bayes in 18th century, a fairly simple statistical method is used that utilizes the observed probability of an event (an *a priori* knowledge) to predict the probability of its reoccurrence if similar conditions exist. Using the definition presented in Rogers (2000) applied to PMW rainfall detection, rain rate probability is given by the following equation:

$$P (R \mid Tb) \sim P (R) \text{ x } P (Tb \mid R) / P (Tb) \tag{4.1}$$

where P(R | Tb) is the *a posteriori* conditional probability of rain rate (R) occurring with observed brightness temperature vector (Tb); P(R) and P(Tb) are *a priori* probabilities of rain rate and brightness temperature, respectively; and P(Tb | R) is the conditional probability of a brightness temperature vector observed with a given rain rate, R. Terms on the right hand side of Eq. (4.1) are given by *a priori* knowledge (stored in what is usually referred to as an *a priori* database), while the left hand side represents the most likely outcome (a prediction). In the PMW application (Figs. 4.1 and 4.2) the retrieved rain rate, r_r, is a weighted mean of the entire spectrum of rain rate values where each value is assigned a weight, w_i, proportional to its probability (i.e. P(R|Tb)):

$$r_r = \frac{\Sigma_i r_i w_i}{\Sigma_i w_i} , \quad \text{where} \quad w_i = \exp\{-0.5\,[T_b - F(r_i)]^T S^{-1} [T_b - F(r_i)]\} \tag{4.2}$$

In Eq. (4.2), i is an element of the a priori database, $\mathbf{S}$ is the T_b error covariance (accounting for both instrument and forward model errors), T_b is observed-, while $F(r_i)$ is r_i-associated brightness temperature.

While this approach, in general, provides excellent results, it has two caveats: 1) the solution is always pulled towards a mean of the *a priori* statistics (defined by most frequently observed rain rates), and 2) events that are underrepresented, or do not exist in the *a priori* database, will be assigned low, or even zero, probabilities. The cause of the first problem is low *a priori* probability of extreme rain rates observed in the *a priori* database, while the cause of the second is the low *a priori* probability of observed Tb vector for a given rain rate (i.e., P(Tb | R)).

The two above-mentioned problems constitute the bulk of rainfall retrieval biases discussed throughout this study. Unfortunately, since they result directly from Bayes' method definition, they can only be diminished, not eliminated. If the *a priori* and observed information are rich and allowed to relate well, however, the performance of the Bayes retrieval will likewise improve significantly. This suggests that the sources of the retrieval's bias could potentially be mitigated if the information content of both observed and *a priori* vectors is complemented by elements that can strengthen their links. Seeking such links requires a better understanding of the Tb (i.e. observed) vector and rainfall rate.

If the retrieval employs an observed relationship between two state vectors to retrieve one when the other is available, then its performance is driven by: a) robustness of the observed relationship, and b) an extent to which it is utilized. In the over-land PMW rainfall retrieval used in this study, the most robust relationship is the one between the radiometric signature of the ice scattering aloft and the rain rate itself. Therefore, using a proxy of ice

amount in a cloud to relate to a surface rain rate, will inherently introduce noise if the algorithm cannot distinguish between entries with similar brightness temperature vectors but different rainfall rates. For extreme rainfall rates, this noise translates to a bias for reasons stated above. Atmospheric states, described by CAPE, wind shear, humidity distribution, and aerosol concentrations are thus examined to assess if the extra information they provide allows the algorithm to better distinguish similar precipitation profiles.

4.3. GPROF rainfall retrieval – description and general properties

As an operational passive microwave rainfall retrieval for the Global Precipitation Measurement (GPM) mission (Hou, et al., 2014), the Goddard PROFiling (GPROF) algorithm has been well-documented and extensively analyzed over the past two decades (e.g., Kummerow et al. 2010, 1996, 2015, Meyers et al. 2015, etc.). Developed at NASA Goddard in the mid- '90s, from the work of Kummerow and Giglio (1994), primarily for the purpose of Tropical Rainfall Measurement Mission (TRMM) (Simpson et al., 1988), GPROF lived to the present day, undergoing a number of versions. At the time of this study, its most recent version, labeled by NASA's Precipitation Processing System (PPS) as GPROF.GPM.V4 developed for GPM's Microwave Imager (GMI) successfully serves a constellation of conical and cross-track scanning PMW instruments including GMI, SSMISs[4] (Kunkee et al., 2008), AMSR2[5] (Shimoda, 2005), ATMS[6] (Muth et al., 2005), MHS[7]s (Edwards and Pawlak, 2000)

---

[4] *Special Sensor Microwave Imager/Sounder* aboard Defense Meteorological Satellite Program satellites

[5] *Advanced Microwave Scanning Radiometer 2* onboard the GCOM-W satellite

[6] *Advanced Technology Microwave Sounder* onboard the S-NPP satellite

[7] *Microwave Humidity Sounder* onboard of MetOp and NOAA satellite series

and others. While more details on prior versions of GPROF algorithm can be found in aforementioned literature, a brief overview of the up-to-date algorithm is given below.

GPROF2014v2 is the first fully-parametric version of the algorithm that utilizes a Bayesian approach over both land and ocean surfaces. Over land (the focus of this study), it builds its *a priori* knowledge by employing hydrometeor profiles from the DPR combined algorithm (Grecu et al. 2016). Forward modeling of brightness temperatures is done through radiative transfer modeling (Kummerow et al. 2010) ensuring a good match with observed GMI Tbs. Once available, simulated Tbs and associated hydrometeor profiles are coupled with DPR Ku rain rate and ancillary data to include TPW, surface type and 2m temperature to constitute GPORF's *a priori* database. In the first step (often referred to as preprocessing), the algorithm uses the ancillary information (TPW, surface type and 2-meter temperature) to subset the *a priori* database and reduce the ambiguity of Tb-to-rain-rate relationship. This non-unique relationship between the set of Tbs and the rainfall rate is caused by similar radiometric properties of different combinations in rain DSDs, water vapor, cloud liquid water and ice content. McKague et al. (1998), Berg et al. (2006) and Bennartz and Petty (2001) describe strong correlation between these factors and the three criteria listed above. In this process, surface types are defined using SSM/I observed emissivity climatology (Aires *et al.*, 2011) updated daily by NOAA's AutoSnow product (Romanov *et al.*, 2000), while TPW and 2-meter temperature come from re-analysis data sets such as ECMWF (Dee et al., 2011) and GANAL (JMA, 2000). Upon sub-setting, the remaining database elements are exposed to Bayesian computation and rain rates are assigned a weight proportional to their respective probability given by Eq. (4.2). The same is done to all other parameters (e.g., hydrometeor profiles, convective fraction, precipitation phase) before outputting their weighted means as

87

the retrieval's solution. This methodology ensures the database is consistent with our best spaceborne radar observations to minimize errors, which are recognized by L'Ecuyer and Stephens (2002), and Kummerow et al. (2006) as one of the major error sources. The method is also readily adaptable to other sensors that take part in the GPM constellation: three SSMISs (F16, F17, and F18), AMSR2 (GCOMW1), GMI (GPM), four MHSs (MetOp-A, MetOp-B, NOAA-18, and NOAA-19), and ATMS (Suomi-NPP). The algorithm used in this study fully matches this description except that it replaces DPR Ku surface rainfall with a more accurate MRMS dataset to build its *a priori* database over the continental United States. This was done to ensure that any retrieval biases against MRMS are the result of the algorithm and not a function of the *a priori* database.

4.4. Data and the *a priori* database

This study employs 1 year (Sep 2014 through Aug 2015) of GPM-core satellite (both GMI and DPR), MRMS, GEOS-Chem aerosol and ECMWF reanalysis data to explore GPM PMW rainfall retrieval accuracies in extreme precipitation. The domain is limited to the mid-west and eastern United States (22N-55N, 105W-65W) to form a geographically well-understood test-bed and allow for high-quality data from the MRMS system. The GMI on the core-satellite provides cloud radiometric properties, the DPR provides cloud structure information, the ground-based measurements serve as the validation reference for satellite observations and the *a priori* surface rainfall, while aerosol and reanalysis sets provide necessary ancillary elements.

GMI data. With its 13 MW channels (10.65H/V, 18.7H/V, 23.8V, 36.5H/V, 89.0H/V, 166V/H, and 183.3 +/- 3V, 7V GHz) the GMI instrument (Draper et al. 2015) serves as a

calibration standard for PMW conical-scanning radiometers in GPM constellation. Brightness temperatures used here by GPROF (either as the observed vector or to form the *a priori* databases) are given by GPM level-1 1C-R GMI product (see file specification for GPM products).

DPR data. The DPR instrument, developed by Japan Aerospace Exploration Agency (JAXA) and Japan's National Institute of Information and Communications Technology (NICT), has Ku and Ka precipitation radars operating at 13.6 and 35.5 GHz frequency, respectively, with FOVs of approximately 5 km. The Ku band radar (the only one used in this study) has cross-track width of 245 km, vertical sampling of 250 m, and virtually complete sampling at the surface level (e.g., no gaps between individual FOVs). Its algorithm builds on that of TRMM PR (Iguchi et al. 2009) and, with a minimum detectable signal set to 18 dBZ, is suitable for detection of rain rates above 0.5 mm h^{-1}.

MRMS data. Multi Radar/Multi Sensor (MRMS; Zhang et al. 2016) dataset is used as a reference dataset. For this purpose, it is specifically adapted to the satellite needs, providing high-accuracy precipitation rate estimates at 0.01° spatial and 2-min temporal resolution over the entire CONUS at the time of the satellite overpass. Each estimate is assigned a radar quality index (i.e., a quality flag) and a precipitation type. Only the highest quality data are used to validate GPROF retrievals. In each satellite overpass, MRMS rainfall rate grids are collocated with individual satellite FOVs mimicking sensor-specific antenna geometry (i.e. antenna gain function).

GEOS-Chem data. To provide estimates of lower tropospheric CCN concentration, this study employs GEOS-Chem chemical transport model with the online aerosol microphysics

module TOMAS (Adams and Seinfeld, 2002; Pierce and Adams, 2009; D'Andrea et al., 2013; Pierce et al., 2013). GEOS-Chem was run globally for 2014-2015 at 2° by 2.5° resolution using GEOS-FP re-analysis meteorology fields (GMAO Data Products). GEOS-Chem-TOMAS simulates the particle size distribution from 3 nm to 10 μm in 15 size bins, tracking sulfate, sea salt, organics, black carbon, and dust aerosol species within these size ranges. Kodros et al. (2016) provides a complete description of emissions used in the simulations. Simulated CCN concentrations, given at 2° by 2.5° grids at 6-hour time resolution, are co-located with other ancillary data and joined to both observed fields and the *a priori* database. With the goal of optimizing ingestion of aerosol information to GPROF retrieval and supported by findings of Dusek et al. (2006) and Stolz et al. (2015), only number concentration of aerosols with diameters larger than 40nm (0.04μm) are used as a proxy for CCN.

ECMWF data. The European Centre for Medium-Range Weather Forecasts (ECMWF) interim reanalysis (ERA-Interim) model data (Dee et al. 2011) is used to provide environmental parameters — specifically, 2-meter temperature, total column water vapor, CAPE, wind profile, temperature, dewpoint, and specific humidity — at 0.75° horizontal and 6-h temporal resolution, at 4 pressure levels (850, 700, 500, and 200 mb) for the year of GMI data. While model-induced uncertainties exist, this dataset is still seen as a robust resource based on its consistency, coverage, and previous validation of the ECMWF analyses. Similar to Petkovic and Kummerow (2017), *vertical wind shear* is defined as the difference in wind magnitude at 500- and 850-mb levels. *Low-level dewpoint depression* is defined as the difference between 2m temperature and dewpoint. A *vertical humidity deviation* is defined as the ratio between specific humidity at low- and mid-tropospheric levels. To ensure that the height of the planetary boundary layer (PBL) does not affect these results, midlevel

humidity is taken as a mean value of 450 and 500 mb, while low-level humidity is required to be within the PBL (e.g., 850 mb). To minimize the effect of precipitation on the atmospheric column, the environmental parameters to be used as cloud morphology predictors in the *a priori* database are chosen to correspond to the time step preceding their coupled precipitation rate.

Database. The above datasets are grouped to build the *a priori* knowledge for GPROF retrieval. Each of 14 separate surface types are treated separately. Data count distributions of eight land surface classes occurring over the domain of this study are given in Fig. 4.3 as a function of TPW and 2-meter temperature.
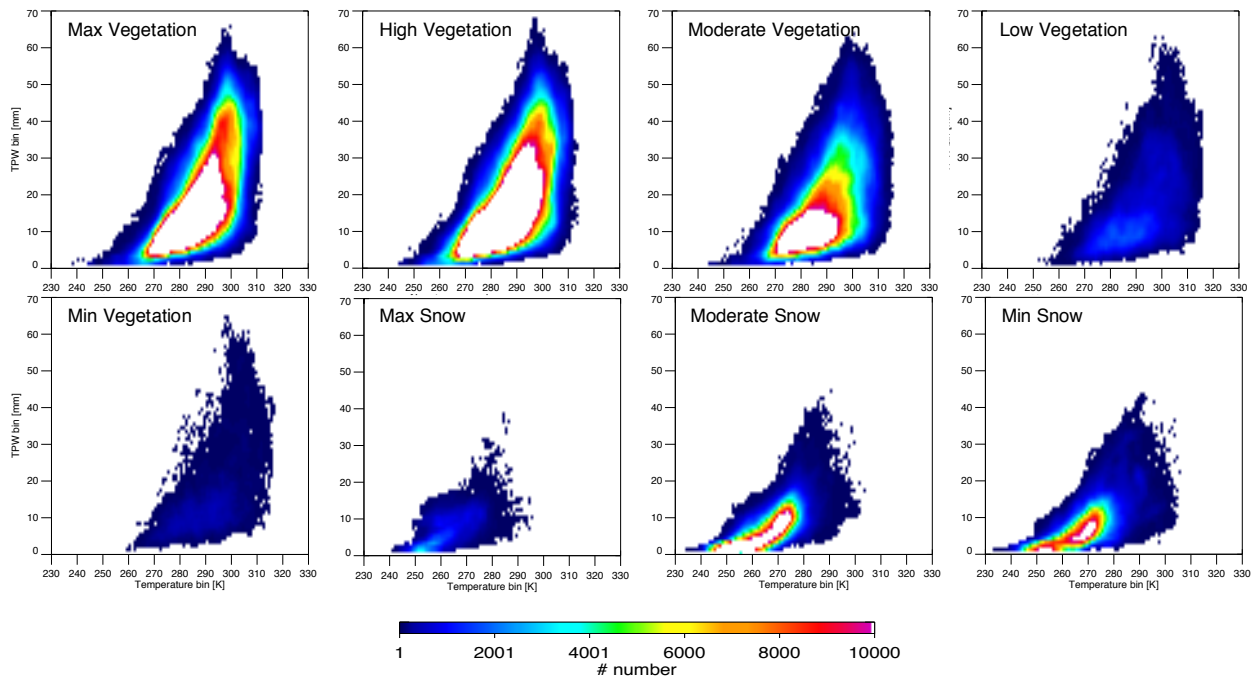
Figure 4.3 A priori databases sample size given by surface type as a function of Total Precipitable Water (TPW) and 2-meter temperature. Water, ice and coastal surface type not included. The overall number of elements exceeds 36 millions ranging from 1.4x10^6 for minimum snow to 1.4x10^9 for maximum vegetation.

4.5. Complementing the retrieval's *a priori* knowledge

Petkovic and Kummerow (2017), hereinafter PK2017, demonstrated a relation between large-scale environment and precipitation system regime that was related to PMW retrieval systematic errors. The authors found that a strong link between PMW bias and environment is related to variability in cloud microphysics and morphology. To support these findings, and demonstrate that this relationship is not specific only to the Amazon-African region (the test-bed used in PK2017), a link between the precipitation regime and high frequency Tb over the US region is examined. Using the same methodology (see Elseasser et al. 2010) and one year of GPM data over the US, all 1° x 1° raining scenes are separated into shallow, deep-unorganized, and deep-organized systems as define by Elsaesser et al, 2010. Employing k-means clustering technique, using the same 5-dimensional space as in PK2017 self-similar scenes are identified. Once again, convective to total rainfall ratio and DPR-Ku echo-top height (with height bins being 0-5, 5-9, and above 9 km) serve as the key properties in defining these structurally-distinct regimes. The result for non-isolated scenes (e.g. larger than 25 km) is shown in Fig. 4.4 together with the relationship between DPR-Ku echo-top height and GMI's 89 GHz Tb.
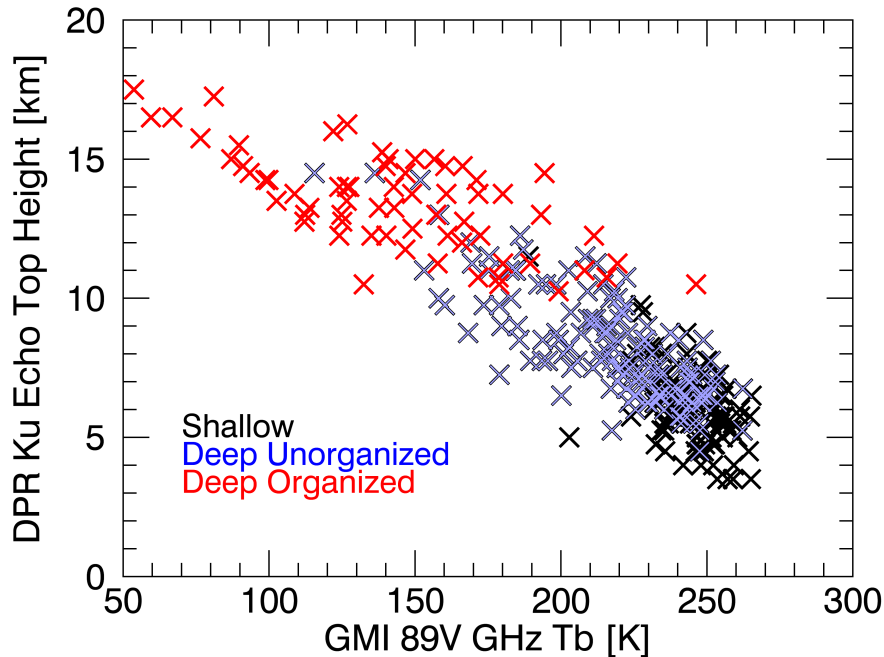
Figure 4.4 Mean cloud top height as a function of mean 89 GHz GMI brightness temperature over 1° x 1° scenes over the CONUS for period Sep 2014 through Aug 2015. The height is estimated using DPR Ku echo top heights. Three colors identify regime type.

As expected, based on sensitivity of 89 GHz channel frequency to the presence of ice in the atmospheric column and the fact that deeper clouds are likely to have greater ice content, echo-top height is strongly correlated with high frequency Tb depressions. However, the more important finding is the indication of a clear separation in the slope of echo top to brightness temperature relation shown in Fig. 4.4 for the three regimes. This suggests that brightness temperatures are strongly linked to variability in cloud organization (i.e. microphysics and dynamics), similar to what was found in PK2017.

4.5.1. Correlation of synoptic state and radiometric properties of precipitating scene

To better understand the relationship between the ice content (and thus Tb depression) and the large-scale environment, a closer look is necessary. While the synoptic environment is indubitably linked to the storms morphology, it is not guaranteed that this link is strong

enough to provide useful information to the retrieval. To estimate a potential of the synoptic state to predict storms morphology relevant to the retrieval, the analysis focused on variability of correlation coefficient between the ice-signal (i.e., 89 GHz Tb) and rainfall rate in the retrieval's *a priori* is performed.

Motivated by PK2017 study, predictors considered in this analysis include those found to relate with PMW systematic errors over Amazon-African region, plus the aerosol concentrations, which are widely recognized as a major factor in cloud formation. The environmental parameters are CAPE, low-level humidity, wind shear, vertical distribution of humidity and CCN concentration. Using one environment at a time to define a synoptic state, five distinct, equally frequent, atmospheric conditions are first recognized for each of the environmental variables. Then, a corresponding correlation coefficient between 89 GHz Tb and MRMS surface rainfall rate is found for each state. Defined to represent the strength of a relationship, correlation coefficient is used here to estimate the utility of each environmental parameter. The results are listed in Table 4.1.

Table 4.1 Correlation coefficient between ice aloft (as represented by the 89 GHz Tb) and rainfall rates for the subsets of a 12-month period (Sep 2014-Aug 2015) given by large-scale environment. Note: the correlation coefficient for the full dataset is -0.43.

CAPE					
Quintile limits [J kg^{-1}]	0 - 30	30 - 60	60 - 140	140 - 485	485 - ∞
Correlation	-0.19	-0.17	-0.37	-0.51	-0.55
CCN					
Quintile limits [cm^{-3}]	0 – 690	690 – 1000	1000 – 1300	1280 – 1680	1680 - ∞
Correlation	-0.44	-0.47	-0.44	-0.43	-0.35
LOW-LEVEL DEW POINT DEPRESSION					
Quintile limits [K]	0 – 1.9	1.9 – 2.2	2.2 – 3.9	3.9 – 6.7	6.7 - ∞
Correlation	-0.48	-0.46	-0.39	-0.38	-0.46
HUMIDITY DISTRIBUTION					
Quintile limits	0 – 0.2	0.2 – 0.4	0.4 – 0.7	0.7 – 1.5	1.5 - ∞
Correlation	-0.51	-0.50	-0.49	-0.38	-0.20
WIND SHEAR					
Quintile limits [m s^{-1}]	-∞ - -1.3	-1.3 – 1.3	1.3 – 4.0	4.0 – 7.9	7.9 - ∞
Correlation	-0.48	-0.48	-0.47	-0.43	-0.27

Upon inspection, it is clear that the correlation coefficient shows significant change across each of the five environmental states. Greater differences in coefficient value are evident between the environments expected to strongly relate to a specific storm morphology. For example, the correlation coefficient for the last quintile of CAPE values is -0.55, while the value in the first two quintiles of this environment is close to -0.18. This can be explained by the expectation that high CAPE values are more typical for strong, often well-developed, storms with well-defined ice-to-rain relationship. To better depict this effect, Fig. 4.5 compares ice-to-rain ratios of five CAPE subsets relative to the mean *a priori* relation. While general findings hold for each of the five synoptic variables, CAPE is chosen as the easiest one to interpret.
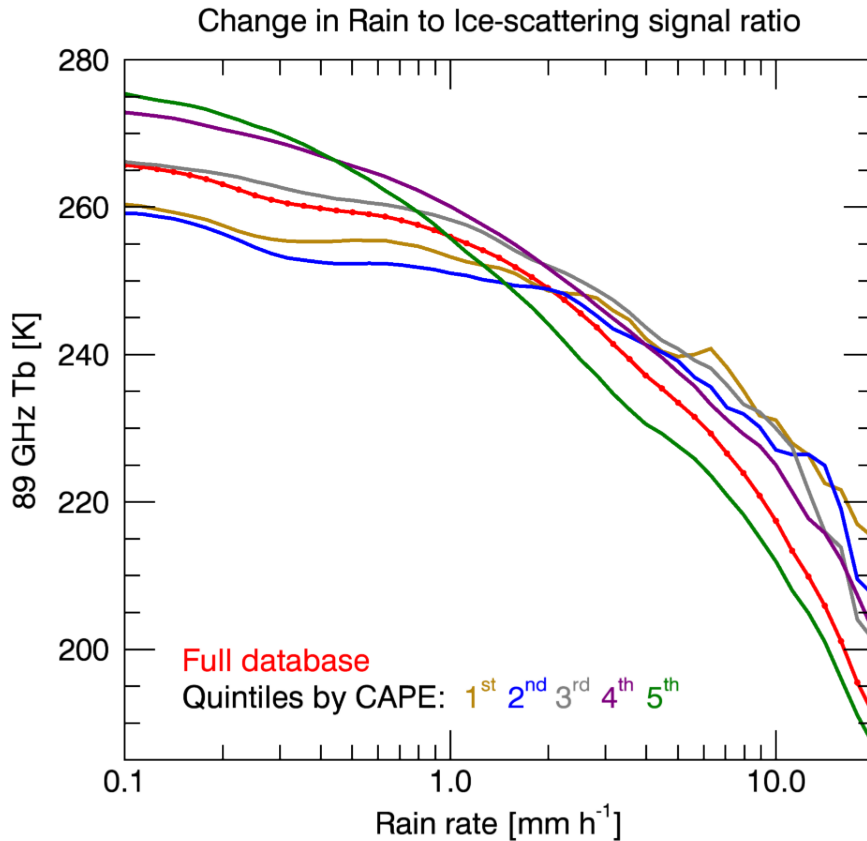
Figure 4.5 Mean relationship between the ice aloft and surface rainfall rate for the full dataset (red line) and five equally populated distinct CAPE environmental subsets (yellow, blue, gray, purple and green). Correlation coefficient for each line is given in Table 4.1.

The plot shows the relationship between ice content, as represented by the 89 GHz Tb, and rainfall for the full *a priori* dataset (red line) and its five subsets defined by CAPE environment. Characterized by different slopes, each environment line indicates a unique ice-to-rain relationship across both environmental and rainfall rate bins. Choosing the same example of the two lowest CAPE quintiles (yellow and blue line in Fig. 4.5) it is obvious that for a given 89 GHz Tb corresponding to low rain rate values (e.g. 250-260 K), both of the two CAPE environments indicate a lower rain rate than suggested by the mean (red line) relationship. While the opposite is true for the other three CAPE subsets (gray, purple and green line) these are, however, atypical (i.e. infrequent) for low rainfall rate conditions, and

as such would typically introduce a bias. This relation, although straightforward, requires

additional attention when extreme rain rates are considered.

4.5.2. Links between GPROF biases and precipitation regime

Concentrating on higher rain rates only (e.g. above 5 mm h^{-1}), which is the focus of this

study, the distribution of the five environment groups in Fig. 4.5 is such that while clearly

suggesting an increase in rain rates for the same brightness temperature depression for four

CAPE environments, the highest CAPE clearly underestimates the precipitation relative to

the ensemble mean (red) line. This is consistent with results from the PK2017 study. The

most vigorous CAPE environment is indeed recognized as the one where GPROF rainfall is

positively biased. To support this statement, analyses similar to those of PK2017 are

repeated over the [20-40N, 65-101W] US region over non-ocean surfaces (same as in Fig.

4.1) using a year of MRMS, DPR and GMI measurements. The relationship between five

environments, storm structures and GPROF biases is presented in Table 4.2.

Table 4.2. Mean values of environment parameters, brightness temperature, total reflectivity above the 0° level, mean rain rate, and GPROF-to-MRMS bias for the Shallow, Deep-unorganized and Deep-organized. Sample is based on approximately 1000 1° x 1° precipitating scenes occurred in period between Sep 2014 and Aug 2015, over non-ocean surfaces in [20N-40N, 65-101W] region.

	Shallow	Deep unorganized	Deep organized
GPROF/MRMS ratio	0.78	1.06	1.12
CAPE [J kg^{-1}]	277	574	952
CCN [cm^{-3}]	1200	1100	1002
Dew point depression [K]	3.64	4.72	6.83
Humidity distribution	0.47	0.38	0.31
Wind shear [m s^{-1}]	7.88	6.21	4.20
89 GHz Tb [K]	266	260	250
Total Reflectivity above 0°C [dBZ]	47	72	99
Rain rate [mm h^{-1}]	0.40	1.07	1.62

As expected, these results confirm the findings of the previous study (PK2017), with

shallow regimes on average being underestimated (22%) and deep-organized regimes being

97

overestimated (12%). These correspond to low and high CAPE values, respectively. Besides demonstrating the bias that is sensitive to the environmental conditions, Table 4.2 also confirms the relationships of the bias to the amount of ice typical for each of the three regimes.

4.5.3. Links between environments – independent information content.

The theoretical aspects of the relationship between CAPE, wind shear, humidity environments and precipitation regimes are discussed in PK2017. Here, the attention is briefly given to the CCN concentrations, which according to Table 4.2, when preceding shallow systems tend to be higher (by 20%) compared to those occurring prior to deep and more organized convection. At the same time, lower CCN concentrations clearly correspond to higher rainfall rates. One possible explanation for this result is that aerosol concentrations over land, while perhaps suppressing the warm rain processes, act to invigorate the ice phase processes as reported by various authors (e.g., Twomey 1977, Andreae et al. 2004, Storer et al. 2010, DeMott et al. 2011, Rosenfeld et al. 2013) with a recent study of Lin et al. 2016 listing relevant research on aerosol interaction with continental precipitation and modeled sensitivities based on field campaign measurements.

In order to effectively use environmental parameters, we focus here on the correlation between them (see Table 4.3). The highest correlation is found between wind shear and both CAPE and CCN concentration with values of only 0.3. This excludes the possibility that high CCN concentrations are exclusively related to very stable atmospheric stratification (e.g., inversions), which are typically characterized by low CAPE and shear values. Low correlations also imply that combinations of environmental parameters may be useful in defining cloud morphology and microphysics.

Table 4.3. Correlation between environments listed in Table 4.1.

	CAPE	CCN	Dew point depression	Humidity distribution	Wind shear
CAPE	-	-0.24	-0.08	-0.01	-0.30
CCN	-0.24	-	0.15	0.04	0.30
Dew point depression	-0.08	0.15	-	0.01	-0.03
Humidity distribution	-0.01	0.04	0.01	-	0.04
Wind shear	-0.30	0.30	-0.03	0.04	-

4.6. Implementation.

With the goal of improving the accuracy of extreme precipitation estimates, the top 10% of rain rates (at FOV scale) is used to test the proposed approach. In order to implement and utilize established links between the environment and the relative amount of ice in raining clouds, environmental parameters are joined to both the observed and *a priori* vectors. One year of ECMWF, GMI, MRMS and GEOS-Chem data is used to generate the *a priori* knowledge which included all observed FOV values and corresponding ancillary fields over the [20-50N, 65-101W] US region. To ensure independence between observed and *a priori* vectors, the true answer is withheld from the retrieval for each pixel. In the baseline run, rain rates are retrieved using the operational GPORF2014 version 4 algorithm as described in Section 4.3. To allow for analysis of the Bayesian weighting, the assigned weight and rain rate of each database element that took part in Eq. (4.2) calculations are added to the output. In this run, the database is constrained using only TPW, surface type and 2-meter temperature. Once available, the retrieved values are assessed using MRMS rain rates.

To test each of the five environments, using one environment at a time, the retrieval is run again but with the information on environment state included in the *a priori* knowledge. Prior to employing the Eq. (4.2), an atmospheric property is used to separate *a priori* knowledge into ten equally frequent environment state categories. Upon constraining the *a*

priori information by TPW, 2-meter temperature, and surface type, database elements characterized by environmental categories other than the category of an observed precipitation scene, are considered as non-matching and ignored. This causes redistribution of weights assigned to the database elements in Eq. (4.2) and, consequently, results in a new weighted mean value. Although alternatives exist, this simple approach is seen as a first choice due to its easy interpretation.

4.7. Assessment

One year of GMI observations over the US [20-55N, 65-101W] region is used to perform five separate runs of the GPORF algorithm using one environment at a time to complement retrieval's existing *a priori* information content. Focusing on extreme precipitation, retrieved values for the top 10% rain rates (at the pixel-level) are assessed using MRMS dataset as a reference. The results are presented in Fig. 4.6 and Table 4.4.
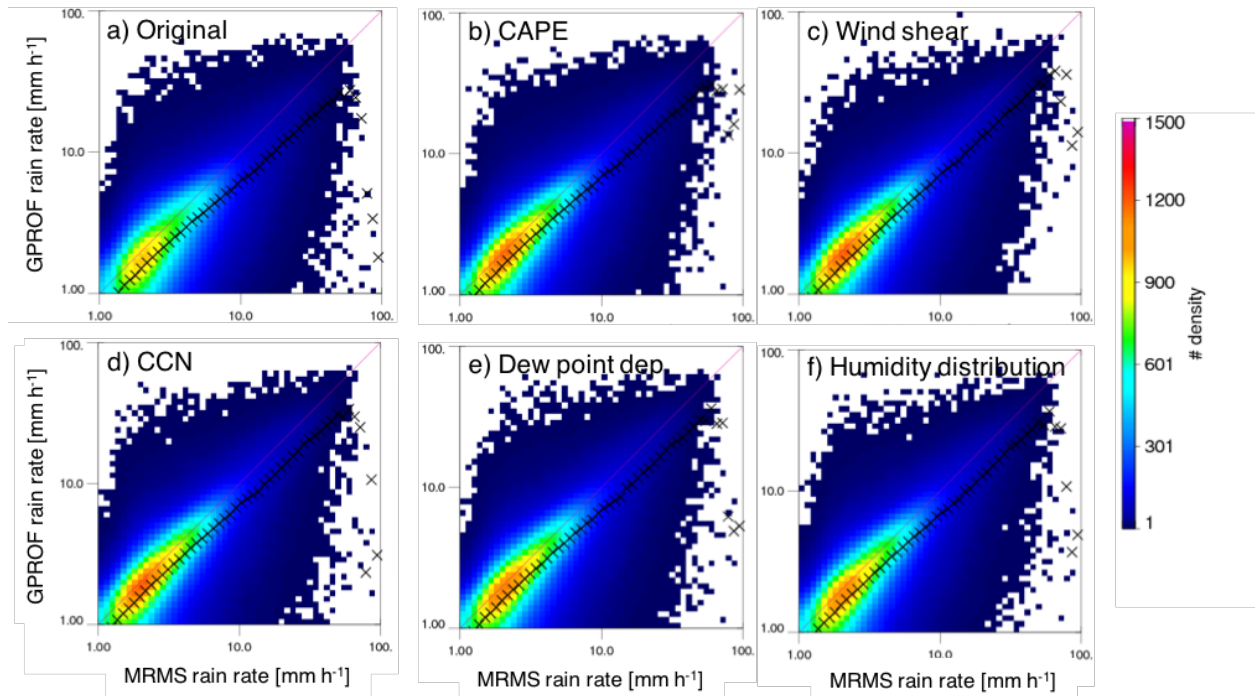
Figure 4.6 Assessment of GPROF retrieval for top 10% rain rates (by value) over the US region using MRMS as a ground reference. Top left (panel-a) represents the original GPROF retrieval without any adjustments to it's a priori information. Panels b) through f) show reference to retrieved rainfall rate relation for CAPE, wind shear, CCN, dew point depression, and humidity distribution, respectively. For specific bias and correlation coefficient values see Table 4.4.

Figure 4.6 offers side-by-side comparison of the original (top left panel; also given in Fig. 4.1) against five new GPROF to MRMS rain rates relations. Based on corresponding statistics, listed in Table 4.4, with no exception, the overall bias is decreased while correlation coefficients increase. Also, the dispersion in the scatter of each of the five experiments is reduced compared to the original. This suggests that the expansion of the retrieval's *a priori* information allowed for: 1) reduction of the randomness (i.e. improved precision) and 2) improved accuracy (the overall bias is lower). Additionally, comparison of mean retrieved rain rates at a number of rain rate intervals (black 'x' symbols in density plots) reveals consistency of these improvements – when compared to the original run, mean values of the other five are all closer to the one-to-one line (red lines in Fig. 4.6).

**Table 4.4. Quantitative assessment of GPROF retrieval for top 10% rain rates (by value) over the US region using MRMS as a ground reference. Values correspond to individual panels in Fig. 4.6. Mean rain rate value of the reference is 3.89 mm h⁻¹.**

Environment criterion	Correlation	Mean rain rate [mm h⁻¹]	Bias improvement [%]
None (original algorithm)	0.66	2.87	/
Humidity distribution	0.71	3.08	19
Dew point depression	0.71	3.09	20
CAPE	0.69	3.11	21
Wind shear	0.72	3.13	24
CCN	0.72	3.15	25
CCN + CAPE	0.77	3.47	54

To complement these results, biases between GPROF rainfall and MRMS reference are mapped for each environment criteria using a 0.25° grid. Simple subtraction of the original from the new map reveals regions where algorithm makes improvements in the top 10% of precipitation rates. An example depicting algorithm performance for CAPE (left) and CCN concentration (right panel) environments is given in Fig. 4.7.
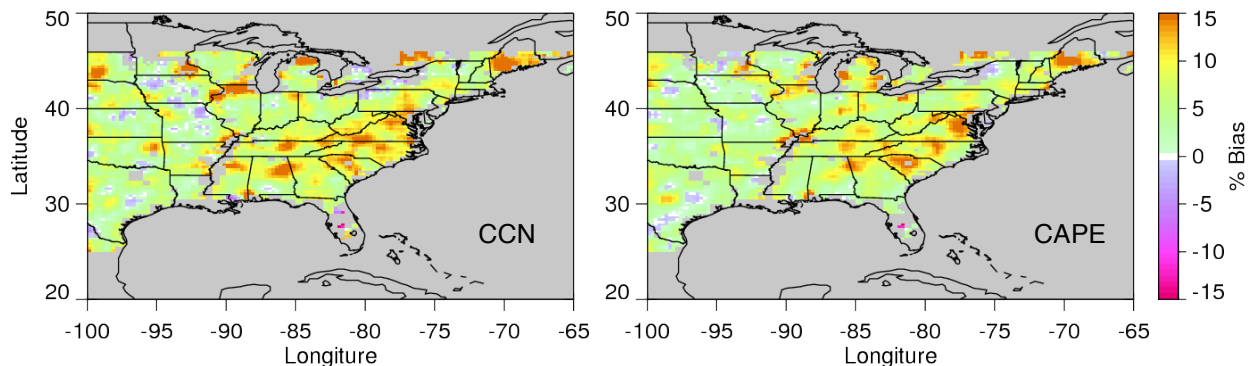
Figure 4.7 Map of improvements in high precipitation rate bias made by using CCN and CAPE environments to complement GPROF algorithm a priori information. Positive values indicate bias improvements.

Notably, areas of improved biases dominate the maps. Regions where the retrieval performs worse than originally are fairly small and generally correspond to the areas of lower initial biases (see Fig. 4.1). Maps for the other three environments have very similar

general properties (not shown here). A relatively strong variability in the magnitude of improvement maxima, and their locations, in the two panels of Fig. 4.7 suggests that the two environments address different portions of extreme rainfall bias. Examples can be seen over New Hampshire and Vermont, North Ohio, Central Georgia and Kentucky where improvement is present in one but absent in the other map. This is in support to the low correlation of the two environments (Table 4.3), suggesting a high potential for complementarity. To test this potential, another experiment is performed in which the algorithm is modified to use only those database elements that are close enough to the observed atmospheric state defined by two environment properties. Results for the example of CAPE and CCN concentration are given in Fig. 4.8.
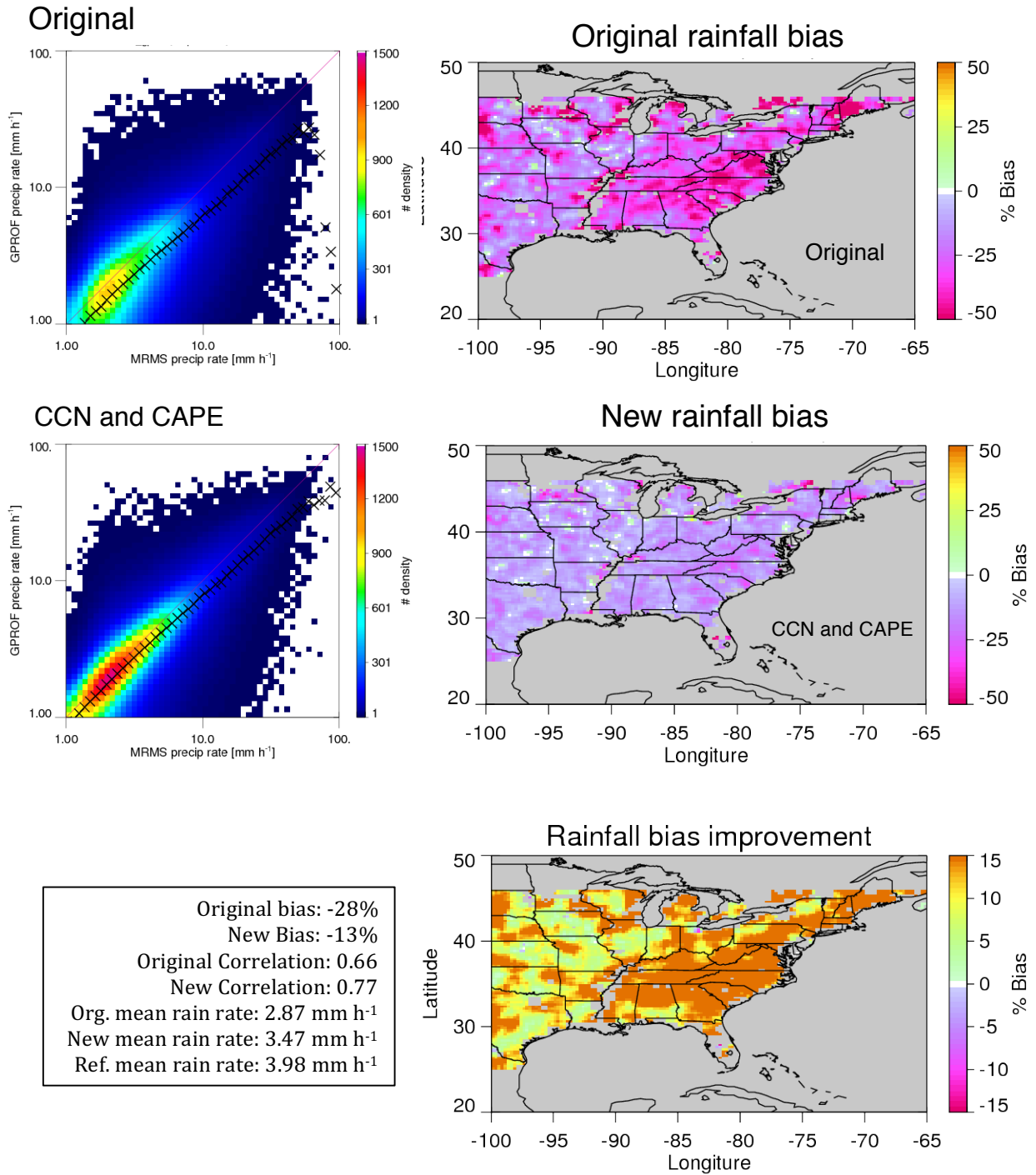
Figure 4.8 Improvement of the top 10% GPROF rainfall bias achieved using CAPE and CCN concentrations parameters. The top two maps in the right column indicate original and new rainfall bias distribution with negative values corresponding to retrieval's underestimating performance. The bottom map is the difference between the two (original – 'CCN and CAPE'), where positive values indicating reduction in the bias.

Compared to any of the individual environmental variables, the new criteria remove a significantly larger portion of the original bias, bringing it down from 28% to only 13%. This corresponds to a change in mean overall rainfall rate of 0.6 mm h^{-1}, which is more than a half of the original discrepancy. The correlation coefficient also improves, increasing from 0.66 to 0.77. Despite the fact that other combinations of environments do not perform as well as this scenario (not shown here), they all make improvements comparable or greater than any of the environments alone.

4.8. Discussion.

A positive assessment of the retrieval with the updated *a priori* information content supports the findings presented in previous sections. Here, we assess whether the improvement is due to an improved characterization of cloud ice processes or simply a statistical artifact (e.g. high CAPE values are associated with high rain rates). Also, while the extreme precipitation estimates are improved, it is unclear what effect this method has on the overall performance of the retrieval. Each of these questions is discussed separately.

4.8.1. Weight distribution

To offer a better insight on how the change in the *a priori* content improve the retrieval itself, a closer look is taken at the process of forming the weighted mean value in Eq. (4.2). If the retrieval is improved, the weights assigned to pixels closer to the true value should be higher. If instead, the retrieval result is simply better because the distribution of rainfall rates in the reduced *a priori* database more closely resembles the true answer, then no impact on the fit between observed and database Tbs should be evident. In the first step of this analysis, collocated ground reference (i.e. MRMS value) values are used to identify

rainfall bias associated with each of the database elements for all retrieved pixels. Then, for each pixel, using an arbitrarily determined bin width of 0.1 mm h^{-1}, all weights falling within the same bias bin are averaged. Zero-weighted database elements are not included. Finally, the overall mean weight values are calculated using all pixels retrieved by the original and modified *a priori* information. Their difference, given as a function of rain rate bias, identifies the origins of bias reductions seen in previous section. Once again, an example where CAPE is used to complement the *a priori* content is used to show the effect (Fig. 4.9). To assure valid comparison, before subtracting the original from the new weight mean, both sets are standardized and normalized. This ensured that the area above and below the zero line is equal.
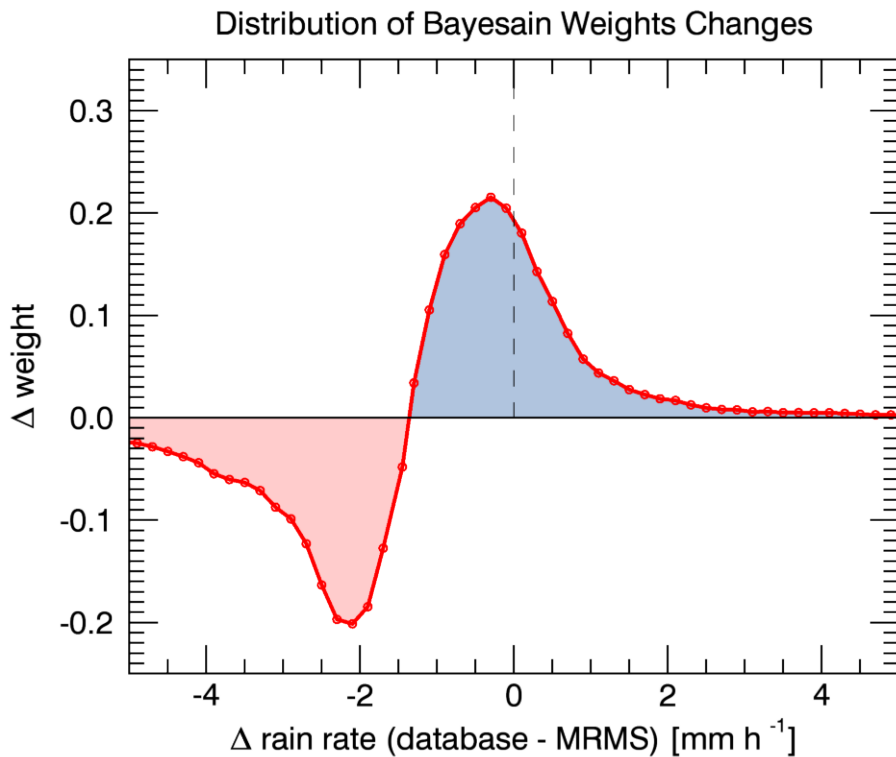
Figure 4.9 Difference in distribution of Bayes mean weights assigned using the original and new, CAPE complemented, a priori information content. The two distributions correspond to the results shown in the first two panels of Fig. 4.6. The differences seen here are associated with 21% reduction of overall rainfall bias (Table 4.4).

The redistribution of weights corresponds to the overall bias reduction of 21% (see Table 4.4 and the second panel in Fig. 4.6). The two areas (red and blue) in Fig. 4.9 indicate that after the *a priori* knowledge is complemented by information on the environment's CAPE, database elements with rainfall rates closer to the observed value received more weight. At the same time, this gain in the weight (blue shading) is compensated by the equivalent reduction (red shading) distributed across negatively biased elements. Being very close to the ideal (i.e. the gain maxima centered at zero biased elements), this distribution of weight adjustments clearly indicates that a goal of identifying elements that relate better to the observed rainfall scene properties is achieved.

4.8.2. The overall effect

The positive effect of introducing complementary information to the *a priori* knowledge on extreme precipitation is not guaranteed to hold when the full rainfall spectrum is considered. This is examined by testing the performance of GPROF with the *a priori* complemented by CAPE information. The result is given in Fig. 4.10.

Increased correlation coefficient, reduced dispersion, and positive bias reduction over the great majority of the domain, demonstrate that additional information content improves the performance of the retrieval in every aspect. While the overall retrieval has significantly lower bias than the opt 10% of rainfall rates (only 13%), making the overall bias reduction less impressive, the true value of the updated *a priori* information is found in its ability to improve both high and low rain rates. This is depicted in Fig. 4.10 by the reduced bias, and increased correlations of the density plots. Similarly, both positive and negative bias regions in the top right panel experience reduction in the bias upon using information on the environment to improve the *a priori* content.

Original

Original rainfall bias

CAPE

New rainfall bias

Original bias: -13%
New Bias: -10%
Original Correlation: 0.75
New Correlation: 0.80
Org. mean rain rate: 0.51 mm h⁻¹
New mean rain rate: 0.50 mm h⁻¹
Ref. Mean rain rate: 0.57 mm h⁻¹

Rainfall bias improvement
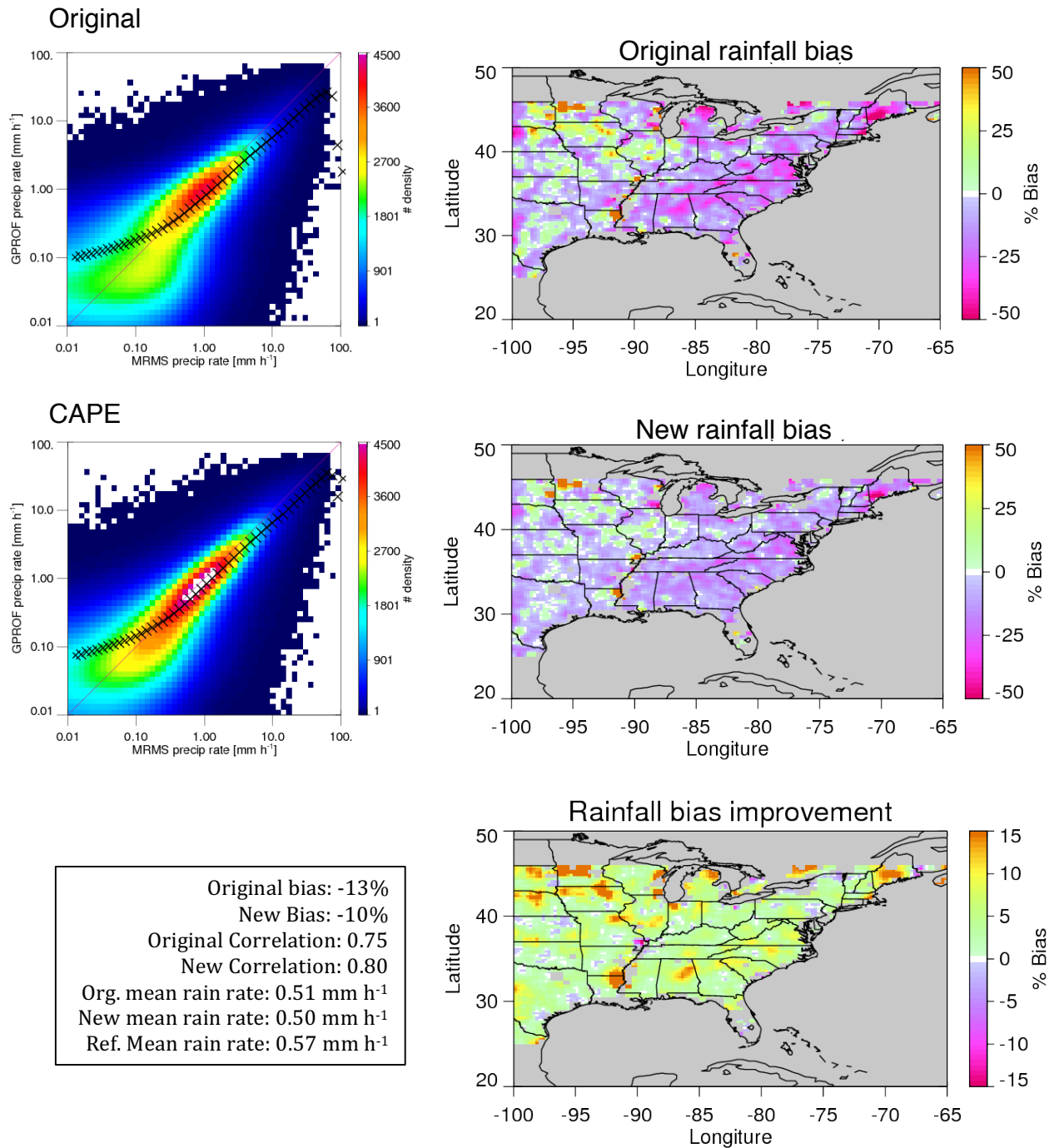
Figure 4.10 Comparison of GPROF performance when using the original and CAPE-enhanced a priori content to retrieve all rainfall over the eastern CONUS in period from Sep 2014 to Aug 2015.

4.9. Summary and conclusions

The goal of this study was to develop, understand, and test the potential for improving the quality of extreme precipitation estimates from satellite passive microwave rainfall retrievals over land. Focusing on Bayes approach and using GPROF, the operational PMW retrieval for GPM mission, this study builds on previous findings to hypothesize that the relationship between large-scale environment and satellite rainfall biases can be used to reduce rainfall estimate uncertainty in extreme atmospheric conditions. The idea of using large-scale environmental variables that are associated with the potential for the atmosphere to produce extreme precipitation is tested. This is accomplished by subsetting the *a priori* information in Bayesian scheme for distinct states of CAPE, CCN concentrations, wind shear, and humidity distribution, supporting the hypothesis. Robustness of the links between five predictors of precipitation system morphology is examined by evaluating the skill of each predictor to recognize a strong link between surface rainfall rate and Tb vector. Analysis suggested that system morphology and the retrieval's biases can indeed be linked through the use of their environmental predictors in atmospheric states favorable for convection.

Considering three structurally different precipitation regimes (shallow, deep-unorganized and organized) it is found that extreme states of the environments lead to distinct cloud morphology. Those characterized by the highest CAPE and wind shear values, as well as large low-level humidity depressions or greater than average decreases in specific humidity with the height, are found to typically precede storms with strong radar reflectivity above the freezing level. The opposite is true for their counterparts, while transitioning states had less defined preference confirming the complexity of cloud microphysics drivers.

Using MRMS rainfall data to assess its performance, it is found that by complementing *a priori* information by co-located environment properties, retrieval reduces the overall pixel-level bias for the most extreme precipitation by 20% to 30%. These improvements are accompanied by noticeable reduction in the random error as well. The analysis of Bayesian-averaging process revealed that added information content successfully shifts probability-based weight toward database elements of rain rate values similar to those given by the reference. This consequently reduces the overall bias in extreme rainfall. A use of more than one parameter to define an atmospheric state is also tested, yielding bias reductions of up to 50%. Finally, the effect of using this approach is tested on the entire rainfall spectrum, finding that the overall performance of the GPROF retrieval is preserved, with improvements in correlation coefficient and biases at both low and high end of rainfall rate range.

CHAPTER 5

CONCLUSIONS

5.1 Summary

With the research goal of improving the understanding of cloud characteristics related to the relative amount of ice aloft (as expressed through microwave Tb depressions) to surface rainfall in diverse meteorological regimes, this study facilitates improved PMW estimates of rainfall, allowing for a better understanding of precipitation trends across the globe.

In its first part (Chapter 2), the study tested the performance of the GPM passive microwave rainfall retrieval during an extreme precipitation event to offer deeper understanding of the algorithm's potentials and guidelines for future development. The retrieval is assessed under extreme precipitation conditions through qualitative and quantitative comparison of its products against two sets of independent ground measurements. The results showed that a constellation of as few as five PMW sensors is capable of providing sufficient sampling and coverage for the retrieval to closely reproduce rainfall rate and accumulation estimates given by ground reference. Discrepancies between satellite-, radar-, and gauge rain accumulation estimates, however, revealed that satellite algorithm underestimated accumulations of a record breaking event by as much as 60%. Upon additional comparisons against a more typical, non-extreme, precipitation event, which indicated satellite underestimate of only 20%, it was concluded that this ambiguous result is likely caused by differences in properties of precipitation systems structures. The

impact of regime dependent cloud microphysics is seen as the key for the accuracy of individual and combined satellite products. This is further confirmed by employing a ground radar network to demonstrate similar errors when Marshal-Palmer Z-R relationship ($Z=200R^{1.6}$) was used in observations of the two structurally different precipitation events. Similar to discrepancies caused when the Z-R relationship designed to represent mid-latitude stratiform systems DSD is used in "tropical-like" conditions, satellite retrievals must assume inadequate links between rain rates corresponding to two structurally very different events. By eliminating artifacts of the retrieval's Bayesian approach, it is estimated that those inadequate links contribute approximately 60% of the total bias. Recognized as critical for improving the accuracy of PMW rainfall estimates over land, variability of the links between rain rate and atmospheric radiometric signatures is investigated next. This is done by providing better understanding of systematic differences seen in PMW rainfall retrievals at larger and coarser scales.

In Chapter 3, the study explored links between ice scattering PMW signature and estimate of surface rain intensity, cloud system structure, and large-scale environments. By employing TRMM PMW and PR products, it is found that observed cloud physics and relationship between Tb depression and surface rain intensity correlate well with regional PMW-to-PR rainfall discrepancies. Variability of ice-scattering-signal-to-rain-rate relationship across regions of opposing systematic differences in rainfall is captured by grouping precipitating scenes into three self-similar cloud classes of distinct levels of organization, as defined by PR. The groups showed potential in removing up to 50% of these regional differences. This result is of specific value for future long-term satellite climate data records that typically do not suffer from overall global biases but are known to be skewed

over the regions of characteristic precipitation regimes. For this not to become a simple tuning exercise, however, it is necessary to find radar-independent properties that have strong relations to cloud morphology and can be utilized by any PMW sensor.

As a natural driver of atmospheric processes, the role of a large-scale environment in defining distinct levels of cloud organization is explored. When constrained by CAPE, wind shear, dew point depression, and vertical humidity distribution, the environment is found to favor certain storm types. Thus, high CAPE values, as well as dry aloft conditions are most commonly seen prior to deep-organized systems. On the other side, low wind shear and weak dew point depression favor shallower unorganized events. The ability of large-scale environments to reduce climate-scale PMW to PR rainfall differences is found appealing, lowering PMW regional biases by up to 40%. With the goal to offer a solid foundation for developing a new algorithm and to better understand how large-scale links translate to pixel-level applications, attention was focused on exploiting observed relationships between large scale environmental drivers and cloud properties.

In Chapter 4, the study focuses on Bayes approach and builds on previous findings to hypothesize that the relationship between large-scale environment and satellite rainfall biases can be effectively used to reduce rainfall estimate uncertainty in extreme atmospheric conditions. The idea of utilizing large-scale atmospheric attributes to complement the *a priori* information in Bayesian scheme is elaborated through modeled and observed data using CAPE, CCN concentrations, wind shear, and humidity distribution.

Using MRMS data to assess its performance, it is found that by complementing *a priori* information with collocated environment properties, retrieval biases of extreme

precipitation at the pixel-level can be reduced by 20% to 30%. A use of more than one parameter to define an atmospheric state yielded bias reductions of up to 50%.

These results lead to the conclusion that large-scale features carry robust information that can successfully explain and remove large portion of satellite precipitation biases in extreme conditions, while being simple to implement.

5.2 Future work and conclusions

Inspired by Chapter 4 of this study and with a goal of setting a direction for the future work, a potential in using the spatial variability of precipitating scene to describe ice-to-rain relation was briefly investigated but not fully understood. For example, a reduction of the overall bias in PMW extreme precipitation estimate for a factor of 2 is achieved by employing a high frequency Tb channel (e.g. 89 GHz) to form a histogram of Tbs corresponding to approximately 100 x 100 km area centered on a retrieving pixel. This histogram is used in a similar manner as the large-scale environments throughout the study to subset the *a priori* information and separate distinct ice-to-rain relationships. While the performance of the algorithm is clearly improved (Fig. 5.1), an explanation on what stands behind this remarkable result requires further parsing of the problem.

Original

Original bias: -30%
New Bias: -15%
Original Correlation: 0.64
New Correlation: 0.77
Observed mean rain rate: 3.75 mm h^{-1}
Original mean rain rate: 2.63 mm h^{-1}
New mean rain rate: 3.18 mm h^{-1}

PDF 89 GHz

Rainfall bias improvement
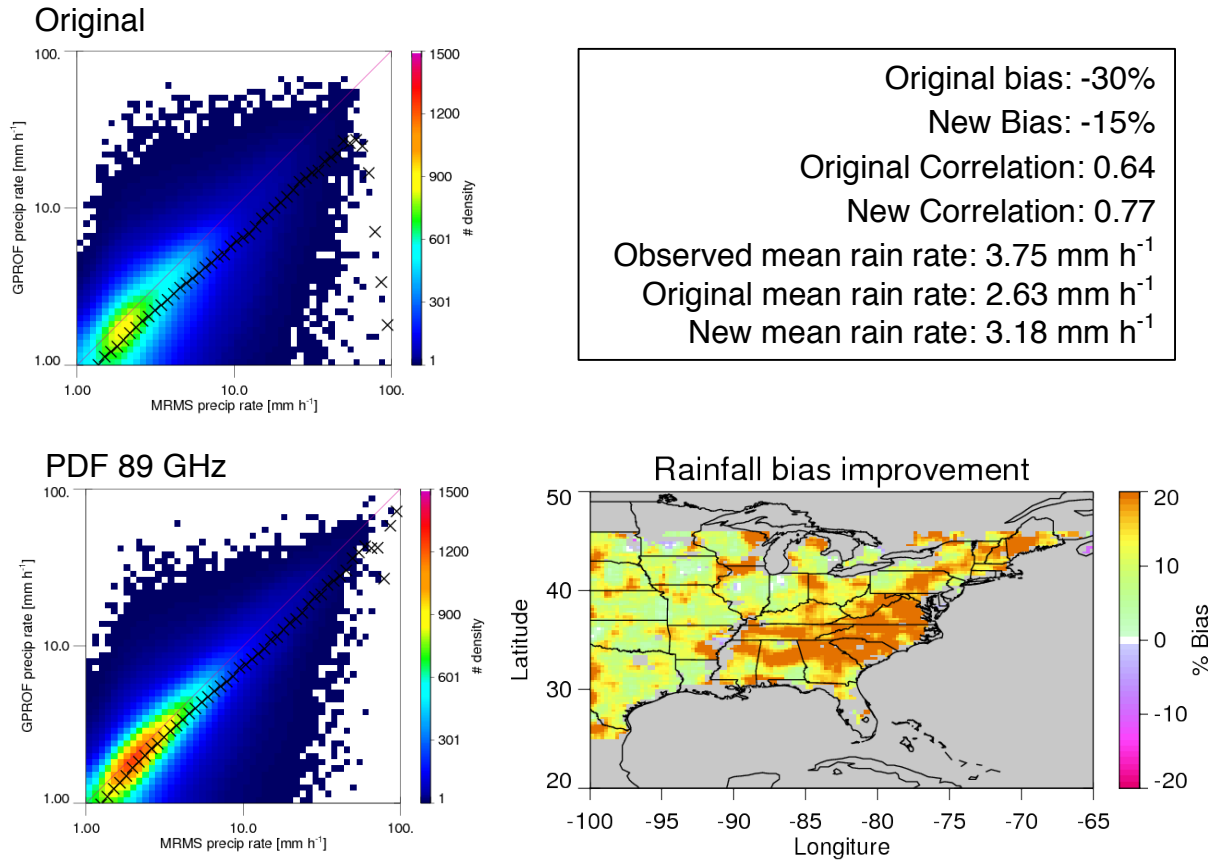
Figure 5.1 Performance of GPROF retrieval when 89 GHz Tb PDF is used to complement the *a priori* information content. Defined using eight 20-degree bins the PDF complements the *a priori* infromation via arbitrarily criterion where scenes of Tb PDFs differencing by more than 20% from that of the observed one are ignored.

Based on findings of Gopalan et al (2000), and McCollum and Ferraro (2003) it can be speculated that 89 GHz Tb PDF correlates well to the Convective vs Stratiform nature of convection and therefore resembles (to some extent) the information given by precipitation regimes shown in Section 3.6.2 as a good predictor of the ice-to-rainfall variability. It is expected that ground based measurements, such as MRMS, will offer a valuable insight to this link.

In addition to this, other findings shown in Chapters 3 and 4, also supported by recent literature, confirm the benefit of using satellite precipitation retrievals as a probing tool in

the effort of improving our understanding of cloud processes. For example, the result presented in Fig. 3.13, where PR to TMI rainfall ratio is given as a function of CAPE and low-level humidity, depicts a complex link between the bias and an atmospheric state. While the highest (lowest) CAPE values are characteristic for TMI's overestimates (underestimates) its absolute bias is governed by the low-level humidity. Dry low-level conditions tend to result in lower PR-to-TMI ratios than those observed in moist environment, regardless the CAPE. This confirms that CAPE is not the only factor to determine the depth of convection and ice amount in a cloud. Although usually sufficient, when combined with moist low-level conditions, large CAPE does not necessarily result in deep convection. The most likely reason is a moisture-induced lowering of the cloud base that deepens the warm cloud layer. This further allows for longer growth of cloud droplets through the warm layer, allowing for collision and coalescence processes (autoconversion). Consequently, the ice-to-surface rainfall ratio is changed, strongly influencing the TMI's bias. This explanation is in compliance with findings of Stoltz et al 2015, who considered additional effect of aerosol concentrations, suggesting even more complex relationships than the one presented here. Therefore, a continued investigation on extracting information from large-scale features to help explaining pixel-level variability should be performed. Special attention in future work should be placed on the stratiform and convective properties of the cloud system and investigation of their PMW signatures, since directly observed large-scale feature showed great potential in removing pixel-level biases. Also, rather than at regional-, future work shell focus on investigating the robustness of the ice-to-rain variability with large-scale environments at global-scales, where assessing of the retrieval shell be done against independent datasets. The first step in this process will be to apply regional relationships

found in this study globally, and investigate differences in retrieval's performance over the regions of opposite rainfall biases (like those shown in Fig. 3.1). Understanding the origins of potential discrepancies shell allow for better understanding of the nature of convection origins and for building stronger links between ice-scattering signal and surface rainfall. Stratiform-convective partitioning is expected to play important role in this process. Findings should be compared against independent precipitation data sets and ideally reproduced by independent observing systems (e.g., ground radar networks and modeled data). It is expected that implementation of those and the results presented in this study will result in ability of the retrieval to confidently diagnose individual extreme precipitation events while at same time its global bias distribution will lose regional signatures.

REFERENCES

Adams, P. J., and J. H. Seinfeld, 2002: Predicting global aerosol size distributions in general circulation models, J. Geophys. Res., **107**(D19), 4370, doi:10.1029/2001JD001010.

Adler, R. F., G. Gu, and G. J. Huffman, 2012: Estimating climatological bias errors for the Global Precipitation Climatology Project (GPCP). *J. Appl. Meteor. Climatol.*, **51**, 1, 84-99.

Adler, R. F., G. J. Huffman, and P. R. Keehn, 1994: Global tropical rain estimates from microwave-adjusted geosynchronous IR data, *RemoteSens. Rev.*, **11**(1-4), 125–152.

Aires, F., Prigent, C., Bernardo, F., Jiménez, C., Saunders, R. and Brunel, P., 2011: A tool to estimate land-surface emissivities at microwave frequencies (TELSEM) for use in numerical weather prediction. *Q. J. of the Roy. Meteorol. Soc.,* **137**: 690–699. doi: 10.1002/qj.803

Andreae, M. O., D. Rosenfeld, P. Artaxo, A. A. Costa, G. P. Frank, K. M. Longo, and M. A. F. Silva-Dias, 2004: Smoking rain clouds over the Amazon. *Science*, **303**, 1337–1342, doi:10.1126/science.1092779.

Atlas, P. A., and O. W. Thiele, 1981: Precipitation measurements from space. Workshop Report, NSA Goddard Space Flight Centre Greenbelt, MD.

Awaka, J., T. Iguchi, and K. Okamoto, 2009: TRMM PR standard algorithm 2A23 and its performance on bright-band detection. *J. Meteor. Soc. Japan*, **87A**, 31–52, doi:10.2151/jmsj.87A.31.

Ba, M. B., D. Rosenfeld, and A. Gruber, 1998: AVHRR multispectral derived cloud parameters: Relationships to microwave scattering signature and to cloud-to-ground lightning. Preprints, *Ninth Conf. on Satellite Meteorology and Oceanography,* Paris, France, *Amer. Meteor. Soc.*, 408–411.

Barrett, E. C., 1970: The estimation of monthly rainfall from satellite data. *Mon. Wea. Rev.*, **98**, 322–327. Doi: http://dx.doi.org/10.1175/1520-0493(1970)098<0322:teomrf>2.3.co;2

Barth, M. C., and Coauthors, 2015: The Deep Convective Clouds and Chemistry (DC3) Field Campaign. *Bull. Amer. Meteor. Soc.*, **96**, 1281–1309. doi: http://dx.doi.org/10.1175/BAMS-D-13-00290.1

Beniston, M., et al., 2007. Future extreme events in European climate: an exploration of regional climate model projections. *Climate Change*, **81**, 71–95. doi:10.1007/s10584-006-9226-z

Bennartz, R., and G. W. Petty, 2001: The sensitivity of microwave remote sensing observations of precipitation to ice particle size distributions. *J. Appl. Meteor.*, **40**, 345–364, doi:10.1175/1520-0450(2001)040<0345:TSOMRS>2.0.CO;2.

Berg, W., T. L'Ecuyer, and S. C. van den Heever, 2008: Evidence for the impact of aerosols on the onset and microphysical properties of rainfall from a combination of active and passive satellite sensors. *J. Geophy. Res.*, **113**, D14S23, doi:10.1029/2007/JD009649.

Berg, W., Tristan L'Ecuyer, and Christian Kummerow, 2006: Rainfall Climate Regimes: The Relationship of Regional TRMM Rainfall Biases to the Environment. *J. Appl. Meteor. Climatol.*, **45**, 434–454. doi: http://dx.doi.org/10.1175/JAM2331.1

Berne, G. Delrieu, and H. Andrieu, 2005: Estimating the Vertical Structure of Intense Mediterranean Precipitation Using Two X-Band Weather Radar Systems. *J. Atmos. Oceanic Technol.*, **22**, 1656–1675.

Bolton, D., 1984: Generation and propagation of African squall lines. *Quart. J. Roy. Meteor. Soc.*, **110**, 695–721.

Bretherton, C. S., M. E. Peters, and L. E. Back, 2004: Relationships between water vapor path and precipitation over the tropical oceans. *J. Climate*, **17**, 1517–1528.

Bringi, V. N., V. Chandrasekar, H. Hubbert, E. Gorgucci, W. L. Randeu, and M. Schoenhuber, 2003: Raindrop size distribution in different climate regimes from disdrometer and dual-polarized radar analysis, *J. Atmos. Sci.*, **60**, 354– 365.

Ciach, G. J., 2003: Local random errors in tipping-bucket rain gauge measurements. *J. Atmos. Oceanic Technol.*, **20**, 752–759.

Cifelli, R., V. Chandrasekar, S. Lim, P. C. Kennedy, Y. Wang, S. A. Rutledge, 2011: A New Dual-Polarization Radar Rainfall Algorithm: Application in Colorado Precipitation Events. *J. Atmos. Oceanic Technol.* **28**: 3, 352-364.

Conner, M. D., and G. W. Petty, 1998: Validation and intercomparison of SSM/I rain-rate retrieval methods over the continental United States, *J. Appl. Meteorol.*, **37**(7), 679–700.

Conway, D., Aurelie Persechino, Sandra Ardoin-Bardin, Hamisai Hamandawana, Claudine Dieulin, and Gil Mahé, 2009: Rainfall and Water Resources Variability in Sub-Saharan Africa during the Twentieth Century. *J. Hydrometeor*, **10**, 41–59. doi: http://dx.doi.org/10.1175/2008JHM1004.1

Cotton, W. R., George Bryan, Susan C. van den Heever 2011: Cumulus Clouds. *Storm and Cloud Dynamics*, International Geophysics, Second Edition 2nd Edition, 243-302.

D'Andrea, S. D., S. A. K. Häkkinen, D. M. Westervelt, C. Kuang, E. J. T. Levin, V. P. Kanawade, R. Leaitch, D. V. Spracklen, I. Riipinen, and J. R. Pierce, 2013: Understanding global secondary organic aerosol amount and size-resolved condensational behavior, Atmos. Chem. Phys., **13**, 11,519–11,534, doi:10.5194/acp-13-11519-2013.

Dee, D. P., and Coauthors, 2011: The ERA-Interim reanalysis: Configuration and performance of the data assimilation system. *Quart. J. Roy. Meteor. Soc.*, **137**, 553–597, doi:10.1002/ qj.828.

DeMott, P. J., and Coauthors, 2011: Resurgence in ice nuclei measurement research. *Bull. Amer. Meteor. Soc.*, **92**, 1623–1635, doi:10.1175/2011BAMS3119.1

Dias, S., M. A. F., and Coauthors, 2002: Cloud and rain processes in a biosphere-atmosphere interaction context in the Amazon Region, *J. Geophys. Res.,* **107**, 8072, doi:10.1029/2001JD000335

Draper, D., D. Newell, F. Wentz, S. Krimchansky, and G. Skofronick-Jackson, 2015: The Global Precipitation Measurement (GPM) Microwave Imager (GMI): Instrument overview and early on-orbit performance. IEEE J. Sel. Top. Appl. Earth Obs. Remote Sens., **8**, 3452–3462, doi:10.1109/ JSTARS.2015.2403303.

Dusek, U, Frank, GP, Hildebrandt, L, Curtius, J, Schneider, J, Walter, S, Chand, D, Drewnick, F, Hings, S, Jung, D, Borrmann, S and Andreae, MO, 2006: Size matters more than chemistry for cloud-nucleating ability of aerosol particles, Science, **312**, no. 5778, pp. 1375-1378. doi: 10.1126/science.1125261

Edwards, P. and Pawlak, D.: MetOp: The space segment for EU- METSAT's polar system, ESA Bulletin, 102, 6–18, 2000.

Ek, M. and L. Mahrt, 1994: Daytime Evolution of Relative Humidity at the Boundary Layer Top. *Mon. Wea. Rev.*, **122**, 2709–2721. doi: http://dx.doi.org/10.1175/1520-0493(1994)122<2709:DEORHA>2.0.CO;2

Elsaesser, G. S., and C. D. Kummerow, 2013: A multisensor observational depiction of the transition from light to heavy rainfall on subdaily time scales. *J. Atmos. Sci.*, **70**, 2309–2324, doi:10.1175/JAS-D-12-0210.1.

Elsaesser, G. S., Christian D. Kummerow, Tristan S. L'Ecuyer, Yukari N. Takayabu, and Shoichi Shige, 2010: Observed Self-Similarity of Precipitation Regimes over the Tropical Oceans. *J. Climate*, **23**, 2686–2698. doi: http://dx.doi.org/10.1175/2010JCLI3330.1

Ferraro, R. R., 1997: Special Sensor Microwave Imager-derived global rainfall estimates for climatological applications. *J. Geophys. Res.*, **102**, 16 715–16 735, doi:10.1029/97JD01210.

Ferraro, R. R., and Coauthors, 2013: An evaluation of microwave land surface emissivities over the continental United States to benefit GPM-era precipitation algorithms. *IEEE Trans. Geosci. Remote Sens.*, **51**, 378–398, doi:10.1109/TGRS.2012.2199121.

Ferraro, R. R., and Gerard F. Marks, 1995: The Development of SSM/I Rain-Rate Retrieval Algorithms Using Ground-Based Radar Measurements. *J. Atmos. Oceanic Technol.*, **12**, 755–770. doi: http://dx.doi.org/10.1175/1520-0426(1995)012<0755:TDOSRR>2.0.CO;2

Ferraro, R. R., Eric A. Smith, Wesley Berg, and George J. Huffman, 1998: A Screening Methodology for Passive Microwave Precipitation Retrieval Algorithms. *J. Atmos. Sci.*, **55**, 1583–1600. doi: http://dx.doi.org/10.1175/1520-0469(1998)055<1583:ASMFPM>2.0.CO;2

Ferraro, R. R., N. C. Grody, and G. F. Marks, 1994: Effects of surface conditions on rain identification using the DMSP-SSM/I, *Remote Sens. Rev.*, **11**(1-4), 195–209.

Ford, T. W., Anita D. Rapp, and Steven M. Quiring, 2015: Does Afternoon Precipitation Occur Preferentially over Dry or Wet Soils in Oklahoma?. *J. Hydrometeor*, **16**, 874–888. doi: http://dx.doi.org/10.1175/JHM-D-14-0005.1

Gilmore, M. S., and L. J. Wicker, 2002: Influences of the local environment on supercell cloud-to-ground lightning, radar characteristics, and severe weather on 2 June 1995. *Mon. Wea. Rev.*, **130**, 2349–2372, doi:10.1175/1520-0493(2002)130<2349:IOTLEO>2.0.CO;2.

GMAO Data Products: GEOS-5 FP, Analyses and forecasts produced in real time, using the most recent validated GEOS-5 system. Available online: https://gmao.gsfc.nasa.gov/products/

Gochis, D. and Coauthors, 2014: The Great Colorado Flood of September 2013. *Bull. Amer. Meteor. Soc.*

Gopalan, K., N.-Y. Wang, R. Ferraro, and C. Liu, 2010: Status of the TRMM 2A12 Land Precipitation Algorithm, *J. Atmos. Ocean. Tech.*, **27**, 1343 – 1354.

GPM Science Team (2016), GPM GMI_R Common Calibrated Brightness Temperatures Collocated L1C 1.5 hours 13 km V04, Greenbelt, MD, USA, Goddard Earth Sciences Data and Information Services Center (GES DISC), Accessed August 2016 https://disc.gsfc.nasa.gov/datacollection/GPM_1CGPMGMI_R_04.html

Grecu, M., W. Olson, S. Munchak, S. Ringerud, L. Liao, Z. Haddad, B. Kelley, and S. McLaughlin, 2016: The GPM Combined Algorithm. *J. Atmos. Oceanic Technol.,* **33**, 2225–2245, doi: 10.1175/JTECH-D-16-0019.1.

Grody, N. C., 1991: Classification of snow cover and precipitation using the special sensor microwave imager, *J. Geophys. Res.*, **96**(D4), 7423–7435.

Gumbel, E. J., 1958: *Statistics of extremes*. Published: New York: Columbia University Press.

Guy, N. and Rutledge, S. A., 2011: Regional comparison of West African convective characteristics: a TRMM-based climatology. *Q. J. R. Meteorol. Soc.* DOI:10.1002/qj.1865

Haddad, Z. S., D. A. Short, S. L. Durden, E. Im, S. Hensley, M. B. Grable and R.A. Black, 1997b: A New Parametrization of the Rain Drop Size Distribution, *IEEE Trans. Geosci. Rem. Sens.*, **35**, 532-539.

Haddad, Z. S., E. A. Smith, C. D. Kummerow, T. Iguchi, M. R. Farrar, S. L. Durden, M. Alves, and W. S. Olson, 1997a: The TRMM 'Day-1' Radar/Radiometer Combined Rain-Profiling Algorithm, *J. Meteor. Soc. Japan*, **75**, 799-809.

Haylock, M.R., N. Hofstra, A.M.G. Klein Tank, E.J. Klok, P.D. Jones and M. New, 2008: A European daily high-resolution gridded dataset of surface temperature and precipitation. *J. Geophys. Res (Atmospheres)*, **113**, D20119.

Herring, S. C., A. Hoell, M. P. Hoerling, J. P. Kossin, C. J. Schreck III, and P. A. Stott, Eds., 2016: Explaining Extreme Events of 2015 from a Climate Perspective. *Bull. Amer. Meteor. Soc.*, **97 (12)**, S1–S145, doi:10.1175/BAMS -ExplainingExtremeEvents2015.1.

Hollinger, J. P., J. L. Peirce, G. A. Poe., 1990: SSM/I instrument evaluation. *IEEE Transactions on Geoscience and Remote Sensing,* **28**(5) pp:781-790.

Hollinger, J.P. 1989: *DMSP Special Sensor Microwave/Imager Calibration/Validation. Final Report, Vol. I.,* Space Sensing Branch, Naval Research Laboratory, Washington D.C.

Holloway, C. E. and J. David Neelin, 2009: Moisture Vertical Structure, Column Water Vapor, and Tropical Deep Convection. *J. Atmos. Sci.*, **66**, 1665–1683. doi: http://dx.doi.org/10.1175/2008JAS2806.1

Hong, Y., K.-L. Hsu, S. Sorooshian, and X. Gao, 2004: Precipitation Estimation from Remotely Sensed Imagery Using an Artificial Neural Network Cloud Classification System. *J. Appl. Meteor.*, **43**, 1834–1853, doi:10.1175/JAM2173.1

Hou, A. Y., R. K. Kakar, S. Neeck, A. A. Azarbarzin, C. D. Kummerow, M. Kojima, R. Oki, K. Nakamura, and T. Iguchi, 2014: The Global Precipitation Measurement Mission. *Bull. Amer. Meteor. Soc.*, **95**, 701–722. doi: http://dx.doi.org/10.1175/BAMS-D-13-00164.1

Houze, R. A., Bradley F. Smull, and Peter Dodge, 1990: Mesoscale Organization of Springtime Rainstorms in Oklahoma. *Mon. Wea. Rev.*, **118**, 613–654. doi: http://dx.doi.org/10.1175/1520-0493(1990)118<0613:MOOSRI>2.0.CO;2

Houze, R. A., Jr., K. L. Rasmussen, M. D. Zuluaga, and S. R. Brodzik, 2015: The variable nature of convection in the tropics and subtropics: A legacy of 16 years of the Tropical Rainfall Measuring Mission satellite, *Rev. Geophys.*, **53**, 994–1021, *doi:*10.1002/2015RG000488.

Houze, R. A., Jr., S. Brodzik, C. Schumacher, S. E. Yuter, and C. R. Williams, 2004: Uncertainties in oceanic radar rain maps at Kwajalein and implications for satellite validation. *J. Appl. Meteor.*, **43**, 1114-1132

Huffman, G. J., and Coauthors, 2007: The TRMM Multisatellite Precipitation Analysis (TMPA): Quasi-global, multiyear, combined-sensor precipitation estimates at fine scales. *J. Hydrometeor.*, **8**, 38–55, doi:10.1175/JHM560.1

Huffman, G. J., D. T. Bolvin, and E. J. Nelkin, 2015: Integrated Multi-satellitE Retrievals for GPM (IMERG) Technical Documentation. NASA/GSFC Code 612, 47 pp. http://pmm.nasa.gov/sites/default/files/document_files/IMERG_doc.pdf

Huffman, G. J., D. T. Bolvin, D. Braithwaite, K. Hsu, R. Joyce, C. Kidd, E. J. Nelkin, and P. Xie, 2015: NASA Global Precipitation Measurement Integrated Multi-satellitE Retrievals for GPM (IMERG). Algorithm Theoretical Basis Doc., version 4.5, 30 pp.

Huuskonen, A., Elena Saltikoff, and Iwan Holleman, 2014: The Operational Weather Radar Network in Europe. *Bull. Amer. Meteor. Soc.*, **95**, 897–907.

Iguchi, T., T. Kozu, J. Kwiatkowski, R. Meneghini, J. Awaka, and K. Okamoto, 2009: Uncertainties in the rain profiling algorithm for the TRMM precipitation radar. *J. Meteor. Soc. Japan*, **87**A, 1-30.

Iguchi, T., T. Kozu, R. Meneghini, J. Awaka, and K. Okamoto, 2000: Rain-profiling algorithm from the TRMM precipitation radar. *J. Appl. Meteor. Climatol.,* **39,** 2038–2052.

Imaoka, K. and Nakamura, K., 2012: Statistical Analysis of the Life Cycle of Isolated Tropical Cold Cloud Systems Using MTSAT-1R and TRMM Data. *Mon. Wea. Rev.*, **140**, 3552–3572. doi: http://dx.doi.org/10.1175/MWR-D-11-00364.1

James, R. P. and Markowski P. M., 2010: A Numerical Investigation of the Effects of Dry Air Aloft on Deep Convection. *Mon. Wea. Rev.*, **138**, 140–161. doi: http://dx.doi.org/10.1175/2009MWR3018.1

JMA, 2000: New numerical analysis and forecast system (in Japanese). *Japan Meteorological Agency Annual Rep. 33,* 143 pp.

Johnson, R. H., T. M. Rickenbach, S. A. Rutledge, P. E. Ciesielski, and W. H. Schubert, 1999: Trimodal characteristics of tropical convection. *J. Climate*, **12**, 2397–2418, doi:10.1175/1520-0442(1999)012<2397:TCOTC>2.0.CO;2

Joyce, R., J. Janowiak, P. Arkin, and P. Xie, 2004: CMORPH: A Method that Produces Global Precipitation Estimates from Passive Microwave and Infrared Data at High Spatial and Temporal Resolution. *J. Hydrometeor.,* **5**, 487–503, doi: 10.1175/1525-7541(2004)005<0487:CAMTPG>2.0.CO;2.

Kim, M.-J., J. A. Weinman, and R. A. Houze, Jr., 2004: Validation of maritime rainfall retrievals from the TRMM-microwave radiometer. *J. Appl. Meteor.*, **43**, 847-859

Kirstetter, P., Guy Delrieu, Brice Boudevillain, Charles Obled 2010: Toward an error model for radar quantitative precipitation estimation in the Cévennes–Vivarais region, France. *Journal of Hydrology*, **394**, Issues 1–2, Pages 28-41, ISSN 0022-1694.

Kodros, J. K., Cucinotta, R., Ridley, D. A., Wiedinmyer, C., and Pierce, J. R., 2016: The aerosol radiative effects of uncontrolled combustion of domestic waste, Atmos. Chem. Phys., 16, 6771-6784, doi:10.5194/acp-16-6771-2016.

Krajewski, W. K., G. J. Ciach, and E. Habib, 2003: An analysis of small-scale rainfall variability in different climatic regimes. *Hydro. Sci. J.*, **48** (2), 151–162.

Kubota, T., and Coauthors, 2007: Global precipitation map using satelliteborne microwave radiometers by the GSMaP project: Production and validation. *IEEE Trans. Geosci. Remote Sens.,* **45,** 2259–2275.

Kubota, T., T. Ushio, S. Shige, S. Kida, M. Kachi, and K. Okamoto, 2009: Verification of high resolution satellite-based rainfall estimates around Japan using gauge-calibrated ground radar dataset. *J. Meteor. Soc. Japan*, **87**A, 203– 222.

Kummerow, C. , William Barnes, Toshiaki Kozu, James Shiue, and Joanne Simpson, 1998: The Tropical Rainfall Measuring Mission (TRMM) Sensor Package. *J. Atmos. Oceanic Technol.*, **15**, 809–817. doi: http://dx.doi.org/10.1175/1520-0426(1998)015<0809:TTRMMT>2.0.CO;2

Kummerow, C. and Coauthors, 2001: The Evolution of the Goddard Profiling Algorithm (GPROF) for Rainfall Estimation from Passive Microwave Sensors. *J. Appl. Meteor. Climatol.*, **40**, 1801–1820, doi:10.1175/ 1520-0450(2001)040,1801:TEOTGP.2.0.CO;2.

Kummerow, C. and J. A. Weinman, 1988: Determining microwave brightness temperatures from precipitating horizontally finite and vertically structured clouds. *J. Geophys. Res.*, **93 (D4)**, 3720–3728.

Kummerow, C. and L. Giglio, 1994: A Passive Microwave Technique for Estimating Rainfall and Vertical Structure Information from Space. Part I: Algorithm Description. *J. Appl. Meteor.,* **33**, 3–18, doi: 10.1175/1520-0450(1994)033<0003:APMTFE>2.0.CO;2.

Kummerow, C., and Coauthors, 2000: The Status of the Tropical Rainfall Measuring Mission (TRMM) after Two Years in Orbit. *J. Appl. Meteor.*, **39**, 1965–1982. doi: http://dx.doi.org/10.1175/1520-0450(2001)040<1965:TSOTTR>2.0.CO;2

Kummerow, C., David L. Randel, Mark Kulie, Nai-Yu Wang, Ralph Ferraro, S. Joseph Munchak, and Veljko Petkovic, 2015: The Evolution of the Goddard Profiling Algorithm to a Fully Parametric Scheme. *J. Atmos. Oceanic Technol.*, **32**, 2265–2280. doi: http://dx.doi.org/10.1175/JTECH-D-15-0039.1

Kummerow, C., Sarah Ringerud, Jody Crook, David Randel, and Wesley Berg, 2011: An Observationally Generated A Priori Database for Microwave Rainfall Retrievals. *J. Atmos. Oceanic Technol.*, **28**, 113–130. doi: http://dx.doi.org/10.1175/2010JTECHA1468.1

Kummerow, C., W. Berg, J. Thomas-Stahle, and H. Masunaga, 2006: Quantifying global uncertainties in a simple microwave rainfall algorithm. *J. Atmos. Oceanic Technol.*, **23**, 23–37, doi:10.1175/JTECH1827.1

Kummerow, C., W. Olson, and L. Giglio, 1996: A simplified scheme for obtaining precipitation and vertical hydrometeor profiles from passive microwave sensors. *IEEE Trans. Geosci. Remote Sens.*, **34 (5)**, 1213–1232, doi:10.1109/36.536538.

Kunkee, D. B., G. Poe, D. Boucher, S. Swadley, Y. Hong, J. Wessl, and E. Uliana, 2008: Design and evaluation of the first Special Sensor Microwave Imager/Sounder. *IEEE Trans. Geosci. Remote Sens.,* **46,** 863–883.

Kwon, E.-H., B.-J. Sohn, D.-E. Chang, M.-H. Ahn, and S. Yang, 2008: Use of numerical forecasts for improving TMI rain retrievals over the mountainous area in Korea. *J. Appl. Meteor. Climatol.*, **47**, 1995–2007.

L'Ecuyer, T. S. and G. L. Stephens, 2002: An uncertainty model for Bayesian Monte Carlo retrieval algorithms: Application to the TRMM observing system. *Quarterly Journal of the Royal Meteorological Society*, **128**, 1713–1737, doi:10.1002/qj.200212858316.

Laing, A. G. and J. M. Fritsch, 1993: Mesoscale convective complexes in Africa. *Mon. Wea. Rev.*, **121**, 2254-2263.

Laing, A.G., Carbone, R.E., Levizzani, V. 2011: Cycles and propagation of deep convection over Equatorial Africa. *Mon. Weather Rev.* **39**: 2832–2853.

Lee, G. W. and I. Zawadzki, 2005: Variability of Drop Size Distributions: Time-Scale Dependence of the Variability and Its Effects on Rain Estimation. *J. Appl. Meteor.*, **44**, 241–255.

LeMone, M. A., Edward J. Zipser, and Stanley B. Trier, 1998: The Role of Environmental Shear and Thermodynamic Conditions in Determining the Structure and Evolution of Mesoscale Convective Systems during TOGA COARE. *J. Atmos. Sci.*, **55**, 3493–3518. doi: http://dx.doi.org/10.1175/1520-0469(1998)055<3493:TROESA>2.0.CO;2

Lin, Y., Y. Wang, B. Pan, J. Hu, Y. Liu, and R. Zhang, 2016: Distinct Impacts of Aerosols on an Evolving Continental Cloud Complex during the RACORO Field Campaign. *J. Atmos. Sci.,* **73**, 3681–3700, doi: 10.1175/JAS-D-15-0361.1.

Liu, J., C.D. Kummerow, and G.S. Elsaesser, 2017: Identifying and analyzing uncertainty structures in the TRMM Microwave Imager precipitation product. *Int. J. Remote Sens.*, **38**, no. 1, 23-42, doi:10.1080/01431161.2016.1259676.

Lockhoff M., O. Zolina, C. Simmer, and J. Schulz, 2014: Evaluation of Satellite-Retrieved Extreme Precipitation over Europe using Gauge Observations. *J. Climate*, **27**, 607–623.

Lopez, P. 2013: Experimental 4D-Var Assimilation of SYNOP Rain Gauge Data at ECMWF. *Mon. Wea. Rev.*, **141**, 1527–1544.

Lopez, P. 2014: Comparison of ODYSSEY precipitation composites to SYNOP rain gauges and ECMWF model. *ECMWF Technical Memorandum*, **717**, Research Department

Machado, L. A. T., J.-Ph. Duvel, and M. Desbois, 1993: Diurnal variations and modulations by easterly waves of the size distribution of convective cloud clusters over West Africa and the Atlantic Ocean. *Mon. Wea. Rev.*, **121**, 37-49.

Maggioni, V., Sapiano, M. R. P., and Adler, R. F., 2016: Estimating Uncertainties in High-Resolution Satellite Precipitation Products: Systematic or Random Error? *J. Hydrometeor,* **17:4**, 1119-1129

Marshall, J.S. and Palmer, W.M., 1948: The distribution of raindrops with size. *J. Meteorol.*, **5**, 165-166.

McCollum, J. R., A. Gruber, and M. B. Ba, 2000: Discrepancy between gauges and satellite estimates of rainfall in equatorial Africa. *J. Appl. Meteor.*, **39**, 666–679, doi:10.1175/1520-0450-39.5.666.

McCollum, J. R., and Ferraro, R. R., 2003: Next generation of NOAA/NESDIS TMI, SSM/I, and AMSR-E microwave land rainfall algorithms, *J. Geophys. Res.*, **108**, 8382, doi:10.1029/2001JD001512.

McKague, D., K. F. Evans, and S. Avery, 1998: Assessment of the effects of drop size distribution variations retrieved from uhf radar on passive microwave remote sensing of precipitation. *J. Appl. Meteor.*, **37** (2), 155–165, doi:10.1175/1520-0450(1998)037<0155:AOTEOD>2.0.CO;2

Meyers, P. C., R. R. Ferraro, and N.-Y. Wang, 2015: Updated screening procedures for GPROF2010 over land: Utilization for AMSR-E. *J. Atmos. Oceanic Technol.*, **32**, 1015–1028, doi:10.1175/JTECH-D-14-00149.1.

Miriovsky, B. J., and Coauthors, 2004: An experimental study of small-scale variability of radar reflectivity using disdrometer observations. *J. Appl. Meteor.*, **43**, 106–118.

Mohr, K. I. and Edward J. Zipser, 1996: Mesoscale Convective Systems Defined by Their 85-GHz Ice Scattering Signature: Size and Intensity Comparison over Tropical Oceans and Continents. *Mon. Wea. Rev.*, **124**, 2417–2437. doi: http://dx.doi.org/10.1175/1520-0493(1996)124<2417:MCSDBT>2.0.CO;2

Mohr, K. I., J. S. Famiglietti, and E. J. Zipser. 1999: The contribution to tropical rainfall with respect to convective system type, size, and intensity estimated from the 85 GHz ice scattering signature. *Journal of Applied Meteorology*, **38:** 596-606.

Moszkowicz, S., G. J. Ciach, and W. F. Krajewski, 1994: Statistical detection of anomalous propagation in radar reflectivity patterns. *J. Atmos. Oceanic Technol.,* **11,** 1026–1034.

Muth, C., Webb, W. A., Atwood, W., and Lee, P.: Advanced technology microwave sounder on the National Polar- Orbiting Operational Environmental Satellite System, in: Geo- science and Remote Sensing Symposium, 25–29 July 2005. IGARSS '05. Proceedings. 2005 IEEE International, 1, 4 pp., doi:10.1109/IGARSS.2005.1526113, 2005.

Novella, N. S. and Thiaw, W. M., 2013: African Rainfall Climatology Version 2 for Famine Early Warning Systems. *J. Appl. Meteor. Climatol.*, **52**, 588–606. doi: http://dx.doi.org/10.1175/JAMC-D-11-0238.1

Olson, W. O., Christian D. Kummerow, Song Yang, Grant W. Petty, Wei-Kuo Tao, Thomas L. Bell, Scott A. Braun, Yansen Wang, Stephen E. Lang, Daniel E. Johnson, and Christine Chiu, 2006: Precipitation and Latent Heating Distributions from Satellite Passive Microwave Radiometry. Part I: Improved Method and Uncertainties. *J. Appl. Meteor. Climatol.*, **45**, 702–720.

Parsons, D. B., Redelsperger, J.-L. and Yoneyama, K., 2000: The evolution of the tropical western Pacific atmosphere-ocean system following the arrival of a dry intrusion. Q.J.R. Meteorol. Soc., **126**: 517–548. doi: 10.1002/qj.49712656307

Payne, S. W., and M. M. McGarry, 1977: The relationship of satellite inferred convective activity to easterly waves over West Africa and the adjacent ocean during Phase III of GATE. *Mon. Wea. Rev.*, **105**, 413–420, doi:10.1175/1520-0493(1977)105<0413:TROSIC>2.0.CO;2

Petersen, W. A. and Coauthors, 1999: Mesoscale and Radar Observations of the Fort Collins Flash Flood of 28 July 1997. *Bull. Amer. Meteor. Soc.*, **80**, 191–216.

Petersen, W. A., Stephen W. Nesbitt, Richard J. Blakeslee, Robert Cifelli, Paul Hein, and Stephen A. Rutledge, 2002: TRMM Observations of Intraseasonal Variability in Convective Regimes over the Amazon. *J. Climate*, **15**, 1278–1294. doi: http://dx.doi.org/10.1175/1520-0442(2002)015<1278:TOOIVI>2.0.CO;2

Petković, V. and C.D. Kummerow, 2015: Performance of the GPM Passive Microwave Retrieval in the Balkan Flood Event of 2014. *J. Hydrometeor.*, **16**, 2501–2518, doi: 10.1175/JHM-D-15-0018.1.

Petković, V. and C.D. Kummerow, 2017: Understanding the Sources of Satellite Passive Microwave Rainfall Retrieval Systematic Errors Over Land. *J. Appl. Meteor. Climatol.*, **56**, 597–614, doi: 10.1175/JAMC-D-16-0174.1.

Petty, G. and K. Li, 2013: Improved Passive Microwave Retrievals of Rain Rate over Land and Ocean. Part I: Algorithm Description. *J. Atmos. Oceanic Technol.,* **30**, 2493–2508, doi: 10.1175/JTECH-D-12-00144.1.

Pierce, J. R. and Adams, P. J. 2009: Uncertainty in global CCN concentrations from uncertain aerosol nucleation and primary emission rates. *Atmos. Chem. Phys.*, **9**, 1339–1356, doi:10.5194/acp-9-1339-2009.

Pierce, J. R., M. J. Evans, C. E. Scott, S. D. D'Andrea, D. K. Farmer, E. Sweitlicki, D. V. Spracklin 2013: Weak global sensitivity of cloud condensation nuclei and the aerosol indirect effect to Criegee+SO2 chemistry. *Atmos. Chem. Phys.*, **13**, 3163–3176, doi:10.5194/acp-13-3163-2013.

Qie, X., R. Toumi, and Y. Zhou, 2003: Lightning activity on the central Tibetan Plateau and its response to convective available potential energy. *Chin. Sci. Bull.*, **48**, 296–299.

Rasmussen, K. L., M. M. Chaplin, M. D. Zuluaga, and R. A. Houze Jr., 2016: Contribution of Extreme Convective Storms to Rainfall in South America. *J. Hydrometeor*, **17**, 353–367. doi: http://dx.doi.org/10.1175/JHM-D-15-0067.1

Rodgers, C.D., 2000: Inverse Methods for Atmospheric Sounding: Theory and Practice. *World Scientific*, 238 pp

Romanov, P., G. Gutman, and I. Csiszar, 2000: Automated Monitoring of Snow Cover over North America with Multispectral Satellite Data. *J. Appl. Meteor.*, **39**, 1866–1880.

Rosenfeld, D., and C. W. Ulbrich, 2003: Cloud microphysical properties, process, and rainfall estimation opportunities. Radar and Atmospheric Science: A Collection of Essays in Honor of David Atlas, *Meteor. Monogr.*, **52**, Amer. Meteor. Soc., 237–258.

Rosenfeld, D., R. Wood, L. J. Donner, and S. C. Sherwood, 2013: Aerosol cloud-mediated radiative forcing: Highly uncertain and opposite effects from shallow and deep clouds, in Climate Science for Serving Society, edited by G. R. Asrar and J. W. Hurrell, pp. 105–149, Springer, Netherlands.

Rotunno, R., J. B. Klemp, and M. L. Weisman, 1988: A theory for strong, long-lived squall lines. *J. Atmos. Sci.,* **45,** 463–485.

Rowell, D. P., and J. R. Milford, 1993: On the generation of African squall lines. *J. Climate*, **6**, 1181–1193.

Ryu, G.-H., B.-J. Sohn, C. D. Kummerow, E.-K. Seo, and G. J. Tripoli, 2012: Rain rate characteristics over the Korean peninsula and improvement of the Goddard Profiling (GPROF) database for TMI rainfall retrievals. *J. Appl. Meteor. Climatol.*, **51**, 786–798.

Sandford, C., and N. Gaussiat, 2011: Evaluation of an error-based quality index for compositing using UK radar data. OPERA Deliverable OPERA_2011_12, 13 pp. Available online at www.eumetnet.eu/sites/default/files/OPERA_2011_12_Quality_ index_evaluation.pdf.

Schumacher, C., and R. A. Houze, Jr., 2000: Comparison of radar data from the TRMM satellite and Kwajalein oceanic validation site. *J. Appl. Meteor.,* **39**, 2151-2164.

Seo, E.-K., B.-J. Sohn, and G. Liu, 2007: How TRMM Precipitation Radar and Microwave Imager Retrieved Rain Rates differ. *Geophys. Res. Lett.*, **34**, L03805, doi:10.1029/2006GL027857

Seto, S., N. Takahashi, and T. Iguchi, 2005: Rain/no-rain classification methods for microwave radiometer observations over land using statistical information for brightness temperatures under no-rain conditions. *J. Appl. Meteor.*, **44**, 1243–1259, doi:10.1175/JAM2263.1.

Seto, S., T. Iguchi, and T. Oki, 2013: The basic performance of a precipitation retrieval algorithm for the Global Precipitation Measurement mission's single/dual-frequency radar measurements. *IEEE Trans. Geosci. Remote Sens.*, **51**, 5239-5251.

Sharma, S., M. Konwar, D. K. Sarma, M. C. R. Kalapureddy, and A. R. Jain, 2009: Characteristics of rain integral parameters during tropical convective, transition, and stratiform rain at Gadanki and its application in rain retrieval, *J. Appl. Meteor. Climatol.*, **48**, 1245–1266.

Sherwood, S. C., P. Minnis, and M. McGill, 2004: Deep convective cloud-top heights and their thermodynamic control during CRYSTAL–FACE. J. *Geophys. Res.*, **109**, D20119, doi:10.1029/2004JD004811.

Shige, S., M. K. Yamamoto, and A. Taniguchi, 2015: Improvement of TMI Rain Retrieval over the Indian Subcontinent. Remote Sensing of the Terrestrial Water Cycle, *Geophysical Monograph* **206**, Edited by V. Lakshmi, American Geophysical Union, 27- 42.

Shige, S., S. Kida, H. Ashiwake, T. Kubota, and K. Aonashi, 2013: Improvement of TMI rain retrievals in mountainous areas. *J. Appl. Meteor. Climatol.*, **52**, 242–254.

Shige, S., Sasaki, H., Okamoto, K. and Iguchi, T., 2006: Validation of rainfall estimates from the TRMM precipitation radar and microwave imager using a radiative transfer model: 1. Comparison of the version-5 and -6 products. *Geophysical Research Letters, 33:* doi: 10.1029/2006GL026350. issn: 0094-8276.

Shimoda, H.: GCOM missions, Geoscience and Remote Sensing Symposium, 2005. IGARSS '05. Proceedings. 2005 IEEE International, 25–29 July, Seoul, South Korea, 6, 4201–4204, doi:10.1109/IGARSS.2005.1525844, 2005.

Short, D. A., and K. Nakamura, 2000: TRMM radar observations of shallow precipitation over the tropical oceans. *J. Climate*, **13**, 4107–4124.

Simpson, J., R. F. Adler, and G. R. North, 1988: A Proposed Tropical Rainfall Measuring Mission (TRMM) Satellite. *Bull. Amer. Meteor. Soc.*, **69**, 278–295.

Sohn, B.-J., G.-H. Ryu, H.-J. Song, and M.-L. Oh, 2013: Characteristic features of warm-type rain producing heavy rainfall over the Korean peninsula inferred from TRMM measurements. *Mon. Wea. Rev.*, **141**, 3873–3888.

Spencer, R.W., Goodman, H.M., Hood, R.E., 1989: Precipitation retrieval over land and ocean with the SSM/I: identification and characteristics of the scattering signal. *J. Atmos. Oceanic Technol.*, **6,** 254–273.

Steiner, M., Robert A. Houze Jr., and Sandra E. Yuter, 1995: Climatological Characterization of Three-Dimensional Storm Structure from Operational Radar and Rain Gauge Data. *J. Appl. Meteor.*, **34**, 1978–2007. doi: http://dx.doi.org/10.1175/1520-0450(1995)034<1978:CCOTDS>2.0.CO;2

Stolz, D. C., S. A. Rutledge, and J. R. Pierce, 2015: Simultaneous influences of thermodynamics and aerosols on deep convection and lightning in the tropics, *J. Geophys. Res. Atmos.*, **120**, doi:10.1002/2014JD023033.

Storer, R. L., S. C. van den Heever, and G. L. Stephens, 2010: Modeling aerosol impacts on convective storms in different environments. *J. Atmos. Sci.*, **67**, 3904–3915, doi:10.1175/2010JAS3363.1

Stull, R.B., 2015: *Practical Meteorology: An Algebra-based Survey of Atmospheric Science*. Free online for everyone worldwide, under a Creative Commons license. 938 pages.

Taniguchi, A., and Coauthors, 2013: Improvement of high-resolution satellite rainfall product for typhoon Morakot (2009) over Taiwan. *J. Hydrometeor.*, **14**, 1859–1871.

Tetzlaff, G. and M. Peters, 1988: A composite study of early summer squall lines and their environment over West Africa. *Meteorol. Atmos. Phys.*, **38**, 153- 163.

Toracinta, E. R., and Zipser, E. J., 2001: Lightning and SSM/I-Ice-Scattering Mesoscale Convective Systems in the Global Tropics. *J. Appl. Meteor.*, **40**, 983–1002. doi: http://dx.doi.org/10.1175/1520-0450(2001)040<0983:LASIIS>2.0.CO;2

Turk, F.J., Ebert, E.E., Hyun-Jong Oh, Byung-Ju Sohn, 2002: Validation and applications of a realtime global precipitation analysis, *Geoscience and Remote Sensing Symposium. IGARSS '02. 2002 IEEE International*, vol.2, no., pp.705-707 vol.2, 2002 doi: 10.1109/IGARSS.2002.1025625

Twomey, S., 1977: The influence of pollution on the shortwave albedo of clouds. *J. Atmos. Sci.*, **34**, 1149–1152, doi:10.1175/1520-0469(1977)034<1149:TIOPOT>2.0.CO;2

Ushio, T., and Coauthors, 2009: A Kalman filter approach to the Global Satellite Mapping of Precipitation (GSMaP) from combined passive microwave and infrared radiometric data. *J. Meteor. Soc. Japan,* **87A,** 137–151.

Vivekanandan, J., J. Turk, and V. N. Bringi, 1991: Ice water path estimation and characterization using passive microwave radiometry. *J. Appl. Meteor.*, **30**, 1407–1421, doi:10.1175/1520-0450(1991)030<1407:IWPEAC>2.0.CO;2.

Wall, C., C. Liu, and E. Zipser, 2013: A climatology of tropical congestus using CloudSat, *J. Geophys. Res. Atmos.*, **118**, 6478–6492, doi:10.1002/jgrd.50455.

Wang, J., and D. B. Wolff, 2012. Evaluation of TRMM rain estimates using ground measurements over central Florida. *J. Appl. Meteor. Climatol.*, **51**, 5, 926-940.

Wang, N. Y., C. Liu, R. Ferraro, D. Wolff, E. Zipser, and C. Kummerow, 2009: TRMM 2A12 land precipitation product-status and future plans, *J. Meteorol. Soc. Jpn.*, **87A**, 237–253.

Wang, P. K., and D. E. Zhang, 1988: An introduction to some historical governmental weather records of China. *Bull. Amer. Meteor. Soc.*, **69**, 753–758.

Westra, S., Lisa V. Alexander, and Francis W. Zwiers, 2013: Global Increasing Trends in Annual Maximum Daily Precipitation. *J. Climate*, **26**, 3904–3918.

Wilheit, T. T., J. S. Theon, W. E. Shenk, L. J. Allison, and E. B. Rodgers, 1976: Meteorological interpretations of the images from the Nimbus 5 electrically scanned microwave radiometer. *J. Appl. Meteor.*, **15**, 166–172, doi:10.1175/ 1520-0450(1976)015,0166:MIOTIF.2.0.CO;2.

Williams, E. R., S. G. Geotis, N. Renno, S. A. Rutledge, E. Rasmussen, and T. Rickenbach, 1992: A Radar and Electrical Study of Tropical "Hot Towers". *J. Atmos. Sci.*, **49**, 1386–1395. doi: http://dx.doi.org/10.1175/1520-0469(1992)049<1386:ARAESO>2.0.CO;2

Williams, E., V. Mushtak, D. Rosenfeld, S. Goodman, and D. Boccippio, 2005: Thermodynamic conditions favorable to superlative thunderstorm updraft, mixed phase microphysics and lightning flash rate. *Atmos. Res.,* **76**, 288–306, doi: 10.1016/j.atmosres.2004.11.009.

Wolf, P.O., 1966: Comparison of Methods of Flood Estimation. Paper 1, Session A, Proceedings of the Symposium organized by the Institution of Civil Engineers on River Flood Hydrology, London, pp. 1-23.

Wolff, D. B., and B. L. Fisher, 2009: Assessing the relative performance of microwave-based satellite rain-rate retrievals using TRMM ground validation data. *J. Appl. Meteor. Climatol.*, **48**, 1069–1099, doi:10.1175/2008JAMC2127.1

Wolff, D. B., D. A. Marks, E. Amitai, D. S. Silberstein, B. L. Fisher, A. Tokay, J. Wang, and J. L. Pippitt, 2005: Ground validation for the Tropical Rainfall Measuring Mission (TRMM). *J. Atmos. Oceanic Technol.*, **22**, 365–380, doi:10.1175/JTECH1700.1

Xu, Q. and Moncrieff, M. W., 1994: Density current circulations in shear flows. *J. Atmos. Sci.,* **51,** 434–446.

Xu, Q., 1992: Density currents in shear flows—A two fluid model. *J. Atmos. Sci.,* **49,** 511–524.

Yamamoto, M. K., F. A., Furuzawa, A. Higuchi, and K., Nakamura, 2008: Comparison of diurnal variations in precipitation systems observed by TRMM PR, TMI and VIRS. *J. Climate*, **21**, 16, 4011-4028.

Yang, S., William S. Olson, Jian-Jian Wang, Thomas L. Bell, Eric A. Smith, and Christian D. Kummerow, 2006: Precipitation and Latent Heating Distributions from Satellite Passive Microwave Radiometry. Part II: Evaluation of Estimates Using Independent Data. *J. Appl. Meteor. Climatol.*, **45**, 721–739.

Zhang, J. and Coauthors, 2011: National Mosaic and Multi-Sensor QPE (NMQ) System: Description, Results, and Future Plans. *Bull. Amer. Meteor. Soc.*, **92**, 1321–1338.

Zhang, J., K. Howard, C. Langston, B. Kaney, Y. Qi, L. Tang, H. Grams, Y. Wang, S. Cocks, S. Martinaitis, A. Arthur, K. Cooper, J. Brogden, and D. Kitzmiller, 2016: Multi-Radar Multi-Sensor (MRMS) Quantitative Precipitation Estimation: Initial Operating Capabilities. *Bull. Amer. Meteor. Soc.,* **97**, 621–638, doi: 10.1175/BAMS-D-14-00174.1.

Zipser, E. J., C. Liu, D. J. Cecil, S. W. Nesbitt, and D. P. Yorty, 2006: Where are the most intense thunderstorms on Earth? *Bull. Amer. Meteor. Soc.*, **87**, 1057–1071.

LIST OF ABBREVIATIONS

AMSR2	Advanced Microwave Scanning Radiometer 2
BiH	Bosnia and Herzegovina
CAPE	Convective Available Potential Energy
CCN	Cloud Condensation Nuclei
CMORPH	Climate Prediction Center Morphing Technique
CSU	Colorado State University
DMSP	Defense Meteorological Satellite Program
DPR	GPM Dual-frequency precipitation radar
DSD	Drop Size Distribution
E-OBS	High-resolution gridded data set of daily climate over Europe
ECA&D	The European Climate Assessment and Data
ECMWF	European Centre for Medium-Range Weather Forecasts
ERA - Interim	ECMWF Re-analysis Interim
ETH	Echo Top Height
EUMETNET	European Meteorological Network
FOV	Field Of View
GANAL	Global Analysis for near real-time operations
GMI	GPM Microwave Imager
GPCP	Global Precipitation Climatology Project
GPM	Global Precipitation Measurement
GPROF	Goddard Profiling Algorithm
GSMaP	Global Satellite Mapping of Precipitation
IMERG	Integrated Multi-satellitE Retrievals for GPM
IPCC	Intergovernmental Panel on Climate Change
IPCCAR5WG1	IPCC Fifth Assessment Report Working Group 1
LAN	Local Area Network

MJO	Madden-Julian Oscillation
MRMS	Multi-Radar Multi Sensor
MSC	Mesoscale Convective System
NASA	National Aeronautics and Space Administration
NMQ	National Mosaic and Multi-Sensor Quantitative Precipitation Estimation
OPERA	Operational Program for the Exchange of RADAR
PCT	Polarization-Corrected Temperature
PDF	Probability Density Function
PK2017	Petković and Kummerow 2017
PMM	Precipitation Measurement Mission
PMW	Passive Microwave
PPS	Precipitation Processing System
PR	TRMM Precipitation Radar
RFO	Relative Frequency of Occurrence
RHMSS	Republic Hydrometeorological Service of Serbia
RMSE	Root Mean Square Error
SEEVCCC	South East European Virtual Climate Change Center
SSMIS	Special Sensor Microwave Imager/Sounder
Tb	Brightness Temperature
TMI	TRMM Microwave Radiometer
TOA	Top Of the Atmosphere
TPW	Total Precipitable Water
TRFL	Total Reflectivity above the Freezing Level
TRMM	Tropical Rainfall Measuring Mission
US NEXRAD	United States Next-Generation Radar
UTC	Coordinated Universal Time
WMO	World Meteorological Organization